# Long Range Wakefields Due To High Gradient Cavity Designs And Beam Dynamics Studies At Future Linear Colliders.

Christopher J. Glasman

Accelerator Physics Group

School of Physics and Astronomy
University of Manchester

2012

A thesis submitted to the University of Manchester for the degree of Doctor of Philosophy in the faculty of Engineering and Physical Sciences

# Contents

Word Count: 22587

# List of Tables

# List of Figures

# Abstract

The international community is in agreement that a lepton collider in the TeV centre of mass energy range is required to leverage discoveries made at the Large Hadron Collider and expand the physics programme. Two future colliders are proposed. The International Linear Collider (ILC) will collide electron and positron bunches at a centre of mass energy of 500 GeV, upgradable to 1 TeV. The Compact Linear Collider (CLIC) is designed to reach 3 TeV.

This thesis investigates the wakefields, which degrade the beam quality, and beam dynamics in the main linacs of the ILC, presenting the first direct comparison of beam dynamics for linacs made up of the alternative high gradient superconducting cavity designs - the Reentrant and Ichiro cavities. Higher order modes of the electromagnetic field in the cavities, which will be excited by the passage of the bunches, are calculated using finite difference and finite element techniques. A trapped dipole mode in the Ichiro cavity at 2.4498 GHz is identified.

These modes are used as the basis for the beam dynamics studies. These simulations have demonstrated that ILC linacs made up of the new high gradient cavities, with targeted damping, would meet wakefield requirements for delivering high quality beams for particle physics studies. This result is important since any upgrade of the ILC from 500 GeV to 1 TeV centre of mass energy would make use of one of these high gradient cavity designs in the extension to the linacs.

Beam dynamics in the CLIC beam delivery system (BDS), are also detailed. Simulations included deflecting mode Crab Cavities required to maximise collision luminosity when there is a crossing angle, and verify analytic results for the required deflecting voltage and tolerances to phase differences. The tolerance to crab cavity roll angle is found to be extremely tight, at 5.9 millidegrees. Additionally, results in this thesis uncover a problem with the BDS magnet layout which must be addressed.

# Declaration

No portion of the work referred to in this thesis has been submitted in support of an application for another degree or qualification of this or any other university or institute of learning.

# Copyright Statement

# The Author

My education in Physics began at Balliol College, Oxford. I joined the Particle Physics group within the University of Manchester and completed a Masters in 2006. With the support of The Cockcroft Institute and STFC I continued my research into the PhD with Roger Jones.

Currently, I live and work in London but Manchester still feels like home.

# Acknowledgements

Firstly my thanks go to my supervisor, Roger Jones, who provided the direction for this research and the milestones along the way.
A huge thank you to Fred, who made me feel welcome from the first day I visited the group. His door has always been open, my calls and emails always answered - his support and enthusiasm have been invaluable.

Thank you to Ian Shinton for hundreds of helpful suggestions and discussions and for holding the group together. Thanks to Graeme Burt, Peter Williams and Hywel Owen for their advice. Many thanks to Vasim Khan, Nawin Juntong and Narong Chanlek for making Thursdays fun. Thanks to Lisa Alexander-Nunneley for unpicking some of Bane's equations and for making sure I didn't take myself too seriously.

Dankeschön to Warner Bruns, author of the code GdfidL, whose generosity made this project possible.

Thanks to Roger Barlow who led the group and supported me throughout my time at Manchester.

Many, many thanks to Sabah Salih who has kept the infrastructure underpinning this work running almost continuously and always when I needed it. I suspect that the only reason AFS ever went down was to encourage us away from our desks and towards Sand Bar. Thanks to Stuart and Alessandra for helping me to use 800 matlab licenses simultaneously.

Thank you to Rich and Rich for making The Lock Building a great place to live and for still making me smile. Thanks to Simon Head for making sure I knew how important it was to ask "what would Jack do?" Thanks to all my friends who knew when not to ask "how's the thesis going". Thank you to Will for reminding me I had "an academic itch to scratch". Thank you to Fanouria Antoniou, Mamad Eshraqi and Kevin Li for making sure I came back from Chicago with more than just lecture

notes and for welcoming me into your homes.

Thanks to Mum for always believing it would be finished, Dad for always believing I could finish right now and Pete for always believing it could have been finished last week. Thank you to Joy & Giles for their support and timely advice. Thanks to all my family who have always been supportive - I'm sorry you haven't seen much of me over that past few years, your patience is appreciated!

Thank you to Marta for getting me over the finish line, for your unending generosity, for laughing at my jokes (possibly I've already covered that) and for an uncountable number of other things, large and small, for which I can't thank you enough.

# Chapter 1

# Introduction

## 1.1 High Energy Colliders

The Twentieth Century saw the development and construction of a succession of particle accelerators which have increased the centre of mass energy available for collisions and expanded the Physics programmes possible, allowing for discovery and confirmation of Standard Model predicted leptons, quarks, neutrinos[1], bosons and gluons.

These accelerators have had necessarily limited life-spans with new generations replacing the older technology. The beginning of the 21$^{st}$ century saw the final years of data taking at LEP and at Tevatron and the construction and completion of the LHC . The LHC has delivered 5.61 fb$^{-1}$ integrated luminosity to the ATLAS experiment in 2011 and physics analyses continue around the world [3].

The expansion of the world's collider programme is necessary in order to further develop our understanding of fundamental Physics. In particular, for the LHC , to test the theorised existence of a *Higgs Boson*. Interaction with a Higgs Boson is one possible explanation for the origin of mass in the fundamental particles.

[1]Non-collider and cosmic ray fixed target experiments have played a significant role in this case also.

### 1.1.1 Why a Linear Collider?

In order to continue the expansion of the physics programme and make best use of discoveries made at LHC the international community is in agreement that a lepton collider in the TeV centre of mass energy range is required [4]. The LHC is a proton - proton machine in which the energy is divided between three quarks in each proton, as well as constituent gluons. In this case the identity of the particles involved in the central system of a particular event must be inferred from the resulting shower of particles in a detector. This introduces significant background effects and raises uncertainty in particle physics calculations.

In contrast the interaction between an electron and its anti-particle provides a clean environment, in which the central system is known. Further, the energy involved in the collision is much more precisely determined since it is not shared between more fundamental sub-particles. A lepton collider has the ability to make extremely precise measurements which will test theoretical models available and will have distinct discovery channels not available at LHC , particularly when polarised beams are employed [5].

To date the highest energy lepton collider was the LEP machine which operated at CERN until 2000. In its final months the maximum centre of mass energy reached was 205 GeV. The LHC now occupies the 27.1 km tunnel which was dug for LEP . While building another synchrotron machine like LEP is possible and would reduce the engineering and technical challenges it is not practical to build a TeV centre of mass electron storage ring since the losses due to synchrotron radiation are too high.

The synchrotron radiation generated in a complete turn, assuming uniform bending radius in the magnets, is given by [6]:

$$\Delta E = \frac{4\pi}{3} r_0 mc^2 \frac{\beta^3\gamma^4}{\rho} = \frac{e^2}{3\epsilon_0}\frac{\beta^3\gamma^4}{\rho}, \tag{1.1}$$

where $r_0$ is the classical radius of the electron. Taking $\beta$ as essential unity for high energy rings we have:

$$\Delta E \propto \frac{E^4}{m^4\rho}, \tag{1.2}$$

where $E$ is the particle energy, $\rho$ the radius of the ring and $m$ the rest mass of

the particle. Clearly the overhead involved at LHC is insignificant compared to an electron machine operating at the same energy in the same tunnel, since the proton is approximately 2000 times more massive than an electron. In order to avoid the very large civil engineering costs of producing a tunnel with a sufficiently large radius the choice of a linear collider has been made. In the case of a linear collider the losses due to synchrotron radiation are not significant, although the design does introduce a multitude of new technical challenges such as the single-pass problem and the necessity for high gradients in the main linac cavities.

### 1.1.2 Normal Conducting and Superconducting Linear Colliders

The design of a linear collider is dominated by the technology chosen for the main linac system. The linacs are the largest cost driver after the tunnel construction costs and great consideration was given to the two major options: superconducting cavities of the TESLA type and normal conducting copper cavities of SLAC / KEK design.

The most significant properties of a linac cavity are its accelerating gradient and shunt impedance, since these determine the length of the machine and the transfer efficiency of RF power to the beam. Normal conducting cavities have a significant advantage in the first area, having demonstrated gradients of the order of 100 MV/m, albeit without demonstrating the required wakefield suppression, in comparison to the $\sim$ 30 MV/m achievable with TESLA technology and the $\sim$ 50 MV/m which has already been achieved for superconducting cavities with newer designs, as will be described in Chapter 5. The RF power to beam efficiency, $\eta_{\mathrm{RF}\rightarrow\mathrm{beam}}$, can be calculated as follows:

$$\eta_{\mathrm{RF}\rightarrow\mathrm{beam}} = \frac{IE_{\mathrm{acc}}Lt_b}{P_{\mathrm{RF}}t_{\mathrm{RFpulse}}}. \tag{1.3}$$

Taking the ILC Reference Design Report (RDR) nominal parameters, accelerating gradient $E_{\mathrm{acc}} = 31.5$ MV/m, cavity length $L = 1.038$ m, beam train length $t_b = 2625 \times 369.2$ ns $= 969$ $\mu$s, RF pulse energy $P.E. = 293.7$ kW $\times$ 1.565 ms $= 459.6$ J and beam current $I = \frac{Nq}{t_{\mathrm{bs}}} \approx 9$ mA, gives a final efficiency $\eta_{\mathrm{RF}\rightarrow\mathrm{beam}} \approx 60\%$. A cor-

responding calculation for the normal conducting CLIC machine yields $\eta_{\mathrm{RF}\to\mathrm{beam}} \approx 28.5\%$ [7].

The full comparison is rather more involved and includes all systems of the collider, availability of klystron power supplies at the desired frequency, damping ring considerations and wakefield effects, for example. Indeed large documents are available detailing the specifications for full machines of each type operating at 500 GeV [8]. Colliders operating using either technology would have an efficiency of around the 10% mark once all systems have been taken into account, though the superconducting case remains slightly more efficient [9].

Following a global effort and full analysis by the International Linear Collider Technical Review Committee it was recommended in 2004 that superconducting cavities based on the TESLA design would be the technology choice for the Linear Collider [8, 10].

Beyond 1 TeV centre of mass energy there is CLIC - the Compact Linear Collider [11]. The CLIC project is being spearheaded by CERN and currently comprises a 3 TeV design achieved through very high gradient normal conducting cavities operating at 12 GHz. Details of ongoing efforts to mitigate transverse wakefield effects as well as breakdown issues through novel design and optimisation of cavity shapes are detailed in Khan [12]. Work continues in all areas, including the beam delivery system design which incorporates a crab cavity system (see Chapter 9).

## 1.2 Luminosity and Wakefields

In operation a linear collider will accelerate a train of many bunches, with each bunch containing of the order of $10^{10}$ electrons or positrons.

A collider's luminosity $L$ measures the rate and quality of collisions at the interaction point. A high luminosity is desirable since the event rate increases with luminosity and rare physics processes can only be properly investigated with large samples. For a train of Gaussian bunches the luminosity can be approximately determined by:

$$L = \frac{n_b N^2 f_{\mathrm{rep}}}{4\pi\sigma_x\sigma_y} \tag{1.4}$$

where $n_b$ is the number of bunches in a train, $N$ the particles per bunch, $f_{\text{rep}}$ the repetition frequency and $\sigma_x, \sigma_y$ are the horizontal and vertical bunch sizes at the interaction point [6].

The beam power can be written in terms of the repetition frequency $f_{\text{rep}}$ and the centre of mass energy $E_{\text{CM}}$:

$$P_{\text{beam}} = n_b N f_{\text{rep}} E_{\text{CM}}. \tag{1.5}$$

This is related to the beam energy used in Equation 1.3 through the repetition frequency and the number of cavities in the linac. Considering the numerators in Equations 1.4 and 1.5 we express the luminosity in terms of the beam power as:

$$L = \frac{(E_{\text{CM}} n_b N f_{\text{rep}})\, N}{4\pi\sigma_x\sigma_y E_{\text{CM}}} = \frac{\eta_{\text{RF}} P_{\text{RF}} N}{4\pi\sigma_x\sigma_y E_{\text{CM}}}. \tag{1.6}$$

Therefore, for a given $E_{\text{CM}}$ the luminosity is proportional to the RF power. For the LEP synchrotron machine the repetition frequency was 44 kHz compared with just 5 Hz for ILC i.e. a factor of 8800 in luminosity is lost immediately moving to the single pass system. In order to achieve the very high luminosity required it is necessary to reduce the beam cross section at the interaction point.

The vertical beam size is given by $\sigma_y = (\beta_y \epsilon_y/(1+\alpha^2))^{1/2}$, where $\beta$ is known as the beta function, determined by the focussing quadrupole magnets, $\alpha$ is the beam divergence and $\epsilon$ is the emittance. The emittance is a measure of the area occupied by the bunch ensemble in phase-space $(y, y')$ and can be calculated from a sum of the second order moments of each particle about the bunch centroid - the details will be further discussed in Chapter 8. As shown in Figure 1.1, for a Gaussian bunch, the ensemble describes an ellipse in phase space.

According to Liouville's Theorem under the action of conservative forces the phase space area will remain constant, this is the case when considering simple lattice elements like dipole and quadrupole magnets. However there are many elements in the lattice which act non-linearly and cause the emittance to increase. Clearly this has a direct impact on the luminosity and great care must be taken to eliminate sources of emittance dilution in order to preserve the low emittance beam produced by the injector system. In the main linacs the primary source of emittance dilution

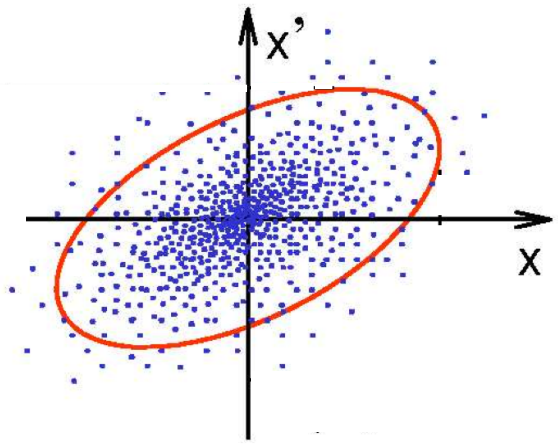


**Figure 1.1:** Bunch distribution in $x - x'$ phase space with inscribed ellipse. Adapted from [13].

is transverse wakefields in the accelerating cavities. The concept of a wakefield will be briefly described below and further expanded in Chapter 4.

### 1.2.1 Wakefields

The passage of a charged particle bunch through the linacs will excite a wakefield [14]. It is formed from the interaction and scattering of the bunch's electromagnetic field with the discontinuities in the environment around it, in particular with the walls of the accelerating cavities. Any analysis can be split into consideration of a short-range wake which acts to distort the shape of a bunch, thus increasing the emittance and a long-range wake which describes the effect of a leading bunch on the bunches trailing behind. The transverse long-range wakefield deflects bunches off the linac axis which increases the projected emittance for the whole bunch train and can lead to multi-bunch beam break up (BBU). This severe effect, first observed at the SLAC linac [15], results in a loss of useful beam at the interaction point. In extreme cases a bunch could impact the beamline and cause damage to the vacuum line, cavities or other components.

## 1.3 Summary

This thesis details simulation work undertaken to calculate the long range wakefields due to higher order modes in the superconducting accelerating cavities of the ILC main linacs, as well as a study of the CLIC crab cavity beam dynamics. Novel high gradient cavity designs from Cornell and KEK are modelled and then beam dynamics are simulated. This research is important in making the case that wakefields generated by the new designs can be sufficiently damped so that these cavities could be used for the future ILC upgrade to 1 TeV. The crab cavity system is crucial to maintaining high luminosity at CLIC.

Chapter 2 presents an overview of the ILC's main systems and operating parameters. In Chapter 3 CLIC is introduced and the main differences between the ILC and CLIC are outlined.

In Chapter 4 we will introduce the terms wakefield, wake potential, delta wake, loss factor and kick factor using their formal definitions.

Chapter 5 gives a brief description of the physics of superconductivity and details the designs for the various superconducting main linac cavities studied in this thesis. Their elliptical shape is governed by competing demands for high gradient operation with very low losses. Three main cavity types are considered, the baseline TESLA design developed at DESY , the Reentrant design from Cornell and the Ichiro cavity design from KEK .

The electromagnetic fields produced by the cavities were simulated using the parallel code GdfidL which employs the finite difference method. The foundations of this technique are discussed in Chapter 6 as well as the limitations and errors which are expected when making use of a numerical method to approximate the fields.

Chapter 7 presents the detailed eigenmode results obtained for the cavities. The cavity modes are also used to calculate long-range wakefields for each cavity type.

The beam dynamics codes LIAR ("Linear Accelerator Research code") and Lucretia have been employed to calculate the emittance growth resulting from constructing the ILC main linacs from Reentrant and Ichiro cavities. These results are

presented in Chapter 8.

Chapter 9 details interesting results from another regime - that of the CLIC beam delivery system. Here similar techniques and codes have been employed in order to investigate the tolerances and required performance of a crab cavity system at CLIC.

Chapter 10 discusses the results obtained and limitations in the simulation work. Further work to be carried out in the future to ensure that ILC operates at the required luminosity is suggested.

# Chapter 2

# ILC machine layout and operation

The collider consists of many independent systems which transport the beam from its creation to the interaction region and on to the beam dumps. In this chapter we will introduce each of the major systems and give an overview of the machine layout as described in the Reference Design Report for the ILC. Further, we will also describe the operating state of the machine systems in collider operation - i.e. give an indication of what level of performance is required, in particular from components in the damping ring and main linacs. As we will show, these systems have competing design requirements and the final machine is a compromise between what is desirable from an engineering perspective, performance or luminosity requirements and the final cost.

## 2.1 Overview

The ILC baseline design is aimed to obtain a maximum centre of mass energy of 500 GeV and a peak luminosity of $2 \times 10^{34}$ cm$^{-2}$s$^{-1}$. The major sub-systems and their location in the overall layout of the ILC are shown in Figure 2.1 and can be briefly summarised as follows [16]:

- A polarized electron source based on a photocathode DC gun.
- An undulator-based positron source, which is driven by the 150 GeV main electron beam.

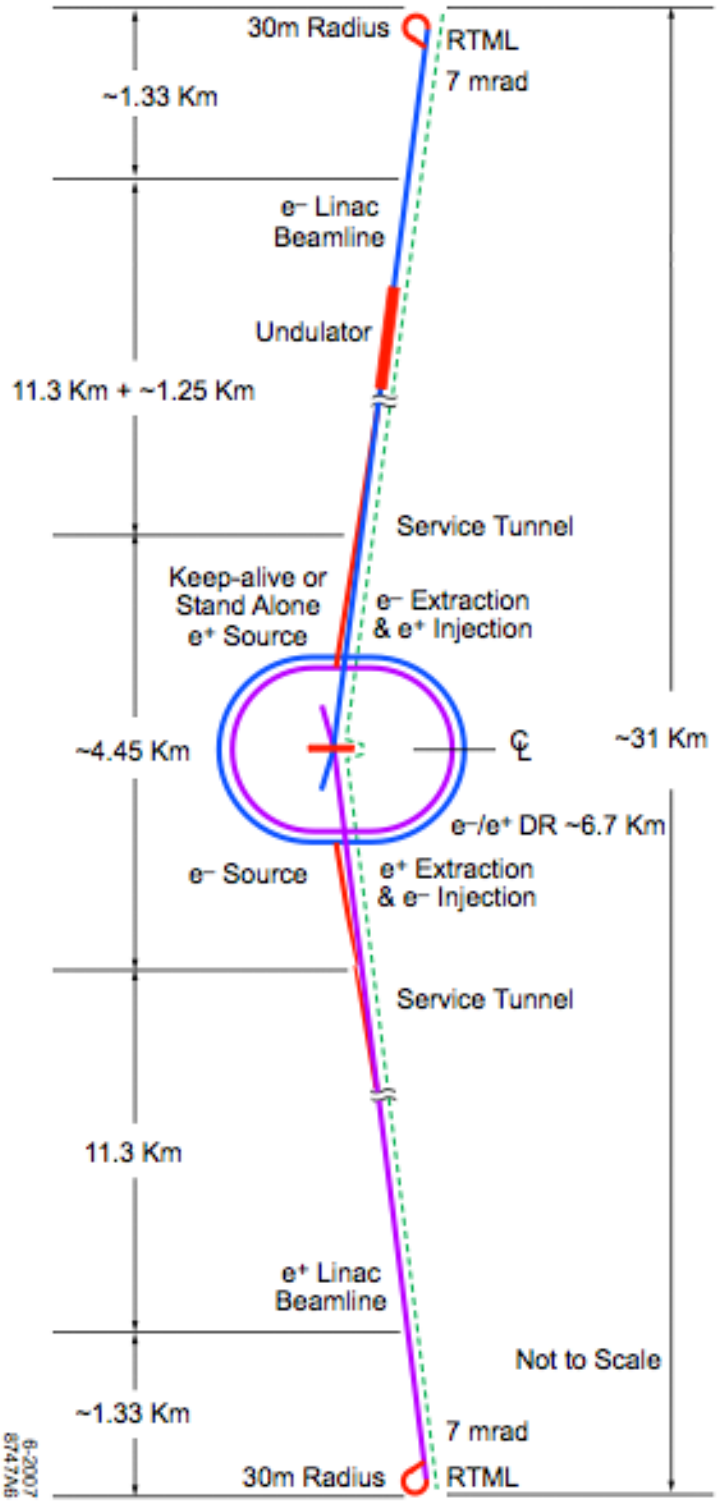


**Figure 2.1:** Schematic of ILC layout at the time of the RDR. The damping rings, ring to main linac, main linacs and IP regions are displayed, from [16]. The service tunnel has since been eliminated from designs.

- The 5 GeV electron and positron damping rings (DR), which are housed in a common tunnel at the ILC complex and have a circumference of 6.7 km.
- The beam transport from the damping rings to the main linacs, which are followed by the bunch compressor system.
- The two main linacs, each 11 km long, which contain superconducting radio frequency (SCRF) cavities.
- The beam delivery system, which brings the two beams into collision at the interaction point (IP). The beams have a 14 mrad crossing angle.

The total length of the ILC is 31 km. If an upgrade of the machine to a centre of mass of 1 TeV was desired the linacs and the beam transport lines would have to be extended by approximately another 11 km each. Some other components in the delivery system would also need to be replaced or augmented.

## 2.2 Pre-linac systems

### 2.2.1 Electron source

It is desirable from a particle physics perspective to have a high degree of polarization in the electron beam. The ILC electron source is, therefore, designed to give a stable train of 2625 bunches of $2 \times 10^{10}$ electrons at 5 Hz and with polarization greater than 80%. This is achieved by making use of a DC gun with a laser illuminated photocathode.

The electron source is placed on the positron linac side of the damping rings. Two independent laser systems providing 790 nm wavelength light, housed in a surface building, are available to provide redundancy. The laser system is based on Ti:sapphire technology. Their light is directed down evacuated light pipes to the two DC guns located in the underground tunnel. Photocathode material is the subject of ongoing research but it has been well established that GaAs/GaAsP superlattice structures can provide the necessary performance, yielding at least 85% polarization and a quantum efficiency greater than 0.5% [17, 18]. The optimum

preparation technique for the photocathode surface is yet to be determined, though a strong candidate can be found in Chanlek's work at the Cockcroft Institute [19].

The DC guns are based on the SLC gun designs, however, significant advances have been made in the intervening years and these will be incorporated into the ILC gun design. It has been optimized to operated at a peak current of 4.5 - 5 A (4.5 nC / 1 ns), limited by space charge effects. This peak current provides sufficient overhead to compensate losses that may occur in the later sections, for example in the bunching system.

Bunching is achieved by two subharmonic bunchers operating at 216.7 MHz and 433.3 MHz respectively, followed by an L-band 5 cell travelling wave buncher. This later system is based on the one in operation at the FLASH facility at DESY. Next, two 50 cell, normal conducting, travelling wave cavities accelerate the bunches to 76 MeV. Details of the bunching system can be found in reference [20].

Later sections provide energy collimation, diagnostics and then match to a booster section consisting of 21, main linac style, cryomodules which accelerate the beam to 5 GeV. The booster linac to damping ring (LTR) beam line provides spin rotation and energy compression functions by providing an arc and solenoid magnetic field. The first bend in the LTR can be switched off to direct the electron source beam to a dump, otherwise the beam is transported to the damping ring entrance.

### 2.2.2 Positron Source

The positron source is required to deliver $2 \times 10^{10}$ positrons per bunch at the IP. The ILC uses photoproduction to generate positrons which are produced with a polarization of about 30%. The electron beam is accelerated to 150 GeV and then diverted into a 150 m long superconducting helical undulator which produces a photon beam of 10 MeV. This photon beam is transported to the target hall where it hits a Ti-alloy target thus producing electromagnetic showers of electrons and positrons. The electrons and the remaining photons are separated from the positrons and dumped, while the positrons are accelerated to 400 MeV and transported 5 km

through the electron main linac tunnel to the central damping ring complex. Here they are boosted to 5 GeV using superconducting L-band RF and then injected into the positron damping ring.

The positron source also includes a low intensity auxiliary (called Keep Alive Source) source that can be injected into the superconducting L-band linac. This allows for commissioning and tuning of the positron systems while the high energy electron beam is not available. The Keep Alive Source is designed to produce 10% of the nominal positron beam by using a 500 MeV electron beam impinging on a tungsten-rhenium target. The positrons are captured and then accelerated using the same linac as the primary sources to accelerate the beam from 400 MeV to 5 GeV.

### 2.2.3 Damping Rings

The damping rings (DR) must accept electrons and positrons with large transverse and longitudinal emittances, compensate for beam incoming beam jitter and produce very low emittance beams for high luminosity collisions downstream.

A main constraint on the DR is the main linac bunch spacing. The DR must be capable of holding the whole bunch train at one time - up to 6000 bunches depending on the parameter set chosen (see Section 2.5.1). The collider operates with a repetition rate of 5 Hz, leaving just 200 ms for the damping ring to complete the damping process of those 6000 bunches from their large emittance entry to the ultra low vertical emittance required. This fast damping is achieved using superconducting wigglers, approximately 200 m long, in each 6.7 km damping ring.

Timing is a major consideration and it is expected that during ongoing design and feasibility studies the main linac bunch spacing and damping ring circumference will change slightly to find the optimum fill pattern.

The relatively large main linac bunch spacing imposes constraints on the DR extraction system also. If the damping rings contained the whole bunch train at the linac spacing they would require a circumference much larger than the 6.7 km in the current design. This can be seen from considering the main linac bunch spacing in distance, approximately 100 m, multiplied up by the $\sim$ 3000 bunches in

the train. The DR extraction kickers must, therefore, enable a fast extraction of a single bunch without disturbing the remaining bunches in the ring. The effective kicker field pulse width must be less than twice the bunch spacing, ensuring that both the immediately upstream and downstream bunches see negligible field.

### 2.2.4 Ring to Main Linac and Bunch Compressors

The Ring to Main Linac (RTML) transports the electron and positron beams from the damping rings to the upstream of their respective linacs. It also needs to collimate the beam halo generated at the damping rings and perform any rotation of the spin polarization that might be required at the IP for physics studies. Finally, compression of the long damping ring bunch by a factor in the range from 30 to 45 is required to provide the short bunches required by the main linac. In addition the RTML is also designed to provide diagnostics and feedback systems as well as sufficient instrumentation to preserve and tune the beam quality.

The RTML systems start with a long low emittance transport from the DP, followed by the collimation section, the spin rotator and the bunch compression system. A two-stage compression system has been chosen in order to provide not just the required compression factor but also some degree of flexibility in the final bunch length but also flexibility to balance the longitudinal and transverse tolerances. The linacs in both compressor stages use standard SCRF cryomodules and RF power similar to that used in the Main Linac. In the first stage stronger focussing is required to mitigate the higher wakefields and cavity-tilt effects resulting from the longer bunch length. The initial bunch length of 9 mm is reduced to 1 mm before entrance into the second bunch compressor which provides the momentum compaction required for compression. The bunch compressor delivers a final beam of bunch length 0.3 mm with an energy of 15 GeV.

The diagnostics, correction and operational requirements of the RTML are integrated into the design of the entire beamline. For example three emittance measurements are performed. The first before the collimation section, the second prior to entrance into the bunch compressor and the third between the compressor and

the linac.

## 2.3 Main Linac

The main linacs, one for each of the positron and electron lines, are the largest single system in the ILC. They consist of 14,560 superconducting cavities and 1680 focussing quadrupole magnets. The accelerating cavities are arranged into cryomodules, which contain 8 or 9 cavities, quadrupole magnets are included in place of the fifth cavity in some cryomodules, surrounded by a helium vessel which maintains the temperature required for superconducting operation. High power RF is fed from klystrons (see Section 2.3.1) through waveguides into the cryomodule and to the cavities via power couplers. The details of the cavity design will be discussed in Section 2.3.2 and Chapter 5. The cavities operate at 1.3 GHz and must be carefully synchronised with the RF systems in the earlier parts of the machine. Should the RF frequency or the phase begin to shift from the nominal then bunches entering the main linac will not receive the correct acceleration, an error in the energy is introduced. The main linac magnet lattice is designed for a particular progression in bunch energy, errors in the energy can lead to emittance dilution since the bunches are no longer correctly focussed.

The choice of frequency is the result of a trade off between the higher cost associated with lower frequency (larger cavity dimensions) and increased surface resistivity at higher frequencies which leads to a lower sustainable gradient. The two main linacs have a combined length of 23 km and accelerate the beams from their injected energy of 15 GeV to 250 GeV. They use superconducting technology, with 9 cell standing-wave niobium cavities of approximately 1 m in length, which operate at an average gradient of 31.5 MV/m. The cavities are immersed in a saturated Helium bath in order to keep the temperature at 2 K. The nominal parameters of the linacs are summarised in Table 2.1.

The power source for the accelerating cavities is a 10 MW klystron. The details of the power source arrangement are discussed in section 2.3.1.

| **Parameter** | Value | Units | **Parameter** | Value | Units |
|---|---|---|---|---|---|
| Initial beam energy | 15 | GeV | Initial $\gamma\epsilon_x$ | 8.4 | $\mu$m |
| Final beam energy | 250 | GeV | Final $\gamma\epsilon_x$ | 9.4 | $\mu$m |
| Particles per bunch | $2 \times 10^{10}$ | | Initial $\gamma\epsilon_y$ | 24 | nm |
| Beam current | 9.0 | mA | Final $\gamma\epsilon_y$ | 34 | nm |
| Bunch spacing | 369 | ns | $\sigma_z$ | 0.3 | mm |
| Bunch train length | 969 | $\mu$s | Initial $\sigma_E/E$ | 1.5 | % |
| Number of bunches | 2625 | | Final $\sigma_E/E$ | 0.14, 0.10 | % |
| Pulse repetition rate | 5 | Hz | Beam phase | 5 | ° |

**Table 2.1:** Nominal parameters of the Main Linacs of the ILC.

### 2.3.1 Power sources

The baseline design specifies 10 MW multi-beam klystrons (MBK) which have high efficiency (65%) by making use of multiple low space charge beams. They will operate at 1.3 GHz as required by the main linac cavities, further parameters are listed in Table 2.2.

560 klystrons are required for the two main linacs. Each will feed an "RF unit" consisting of three cryomodules, see Figure 2.2.

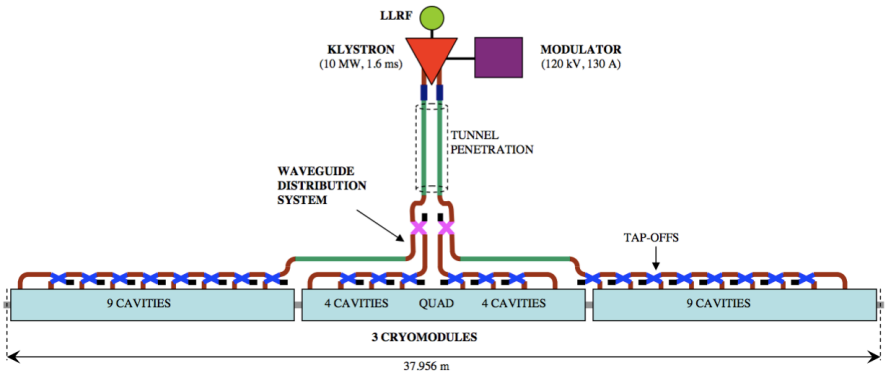


**Figure 2.2:** RF Unit layout, from [16].

The klystrons are partnered with low level RF systems and modulators in order to ensure stable operation and to regulate the cavity fields. At the time of the RDR the design incorporated the power supply systems housed in a parallel service

| Parameter | Specification |
|---|---|
| Frequency | 1.3 GHz |
| Peak Power Output | 10 MW |
| RF Pulse Width | 1.565 ms |
| Repetition Rate | 5 Hz |
| Average Power Output | 78 kW |
| Efficiency | 65 % |
| Saturated gain | $\geq$ 47 db |
| Instantaneous 1 db BW | 3 MHz |
| Cathode Voltage | $\leq$ 120 kV |
| Cathode Current | $\leq$ 140 A |
| Power Asymmetry | $\geq$ 1% |
| Lifetime | >40,000 hours |

**Table 2.2:** Klystron Parameters.

tunnel in order to reduce radiation exposure and facilitate maintenance, however, the separate service tunnel has since proven too costly an option [21].

### 2.3.2 Cavities

The main linacs cavities are superconducting niobium cavities made up of 9 cells. They are known as TESLA cavities, their design is an evolution of that used in the FLASH ("the Free-Electron Laser in Hamburg") light source at DESY. FLASH was previously named the TESLA Test Facility and, as the name suggests, it was the technology test bed for the proposed "TeV Energy Superconducting Linear Accelerator" from which the cavities get their name. The cavities are asymmetric due to the presence of an input coupler and two higher order mode (HOM) couplers, which serve to damp higher order modes excited by the passage of the beam. Further, to avoid HOM trapping, the end cells are of different designs, as shown in Figure 2.3. Chapter 5 contains a detailed discussion of the factors influencing the design of the TESLA cavities, as well as the alternative design candidates, the Reentrant and the

**Figure 2.3:** Photograph of a TESLA cavity. Adapted from [23].

Ichiro cavities.

Prior to installation each cavity is evaluated in a vertical test stand. Cavities must reach a stable gradient of 35 MV/m and a $Q$ value in excess of $0.8 \times 10^{10}$. Ensuring a high yield in industrial fabrication of these cavities is the subject of significant ongoing research around the world. A major part of the move to industrial processes is the construction of XFEL at DESY ("the European X-ray Free Electron Laser"). XFEL will be a high frequency light source based on a linac containing $\sim 800$ TESLA cavities [22].

### 2.3.3 Focussing

Each of the 1680 quadrupole magnets of the main linac has horizontal and vertical dipole correctors and a cavity beam position monitor, operating in the L-Band[1], in order to enable focussing of the beam. The main linac lattice uses weak focussing FODO optics with a quad spacing of about 38 m, which corresponds to one quad per RF unit. The lattice functions are not perfectly regular, due to the aperiodicity of the cryogenic system, and there is a mean phase advance per cell of 75° and 60° in the horizontal and vertical plane respectively. The tune split of 15° between the horizontal and vertical planes reduces the coupling of the horizontal polarization of the cavity dipole mode kicks into the vertical plane, thus preserving the very low emittance $\epsilon_y$ required [25].

The main linacs do not have equipment for intra-train trajectory control neither is the energy or energy spread measured in the main linacs. Both, the trajectory

[1]See details of an example design from the CEA Saclay group [24].

control implementation and the energy diagnostics are performed at the beginning and end of the linac and around the undulator. Dispersion, which is caused by misaligned quadrupole magnets and pitched RF cavities, produces increased emittance. This is corrected through local steering algorithms with additional correction achieved through local orbit distortions, which produce measured amounts of dispersion in a given phase. These are called "dispersion bumps" [26]. Dispersion matching and suppression at the beginning and end of the linac and around the undulator are achieved by supplying additional excitation to small umbers of correctors in "dispersion bumps" configurations.

## 2.4 Post-linac systems

### 2.4.1 Beam delivery system

The beam delivery system (BDS) must transport electrons with energies in the range 100 to 250 GeV from the end of the main linac through to the final focus. It must preserve the low emittance and orientate each bunch so that they collide with the maximum luminosity. Further, the beam delivery system must include some feedback mechanism to ensure collisions occur despite beam jitter, ground motion etc.

The main subsystems of the BDS are the diagnostics region, which links to the main linacs, the fast extraction and tune up beamline, the betatron and energy collimation, the final focus, the interaction region and the extraction line.

The diagnostics region starts at the end of the main linac and is responsible for measuring and correcting the properties of the beam before collimation. It contains a skew correction section, emittance diagnostic section and polarimeter with energy diagnostics. The tune up and extraction systems will detect errant beams and remove them, thus protecting the systems downstream.

The collimation system removes background produced by particles in the beam halo. It has a betatron collimator section as well as energy collimators. They can survive two hits by an errant bunch of 250 GeV or one hit by a 500 GeV beam.

The system also includes a muon shield to stop muons produced by electromagnetic showers created by primary particles.

### 2.4.2 Final focus, interaction region

The final focus system must reduce the beam to the required size at the interaction point, which is a horizontal length of approximately 639 nm and about 5.7 nm in the vertical direction. Figure 2.4 shows the final focus optics system. It creates a large and almost parallel beam at the entrance of the final duplet of strong quadrupoles. Particles of different energies will have a different focal point and therefore a small energy spread causes significant dilution of the beam size. Hence a series of corrections need to be applied. The final focus is designed to cancel chromaticity of the final doublet using sextupoles. Synchrotron radiation from the bending magnets results in emittance dilution so the bending radius must be minimized, particularly at higher energies. To do this the final focus has sufficient magnets for a centre of mass energy of 500 GeV. In order to perform all the diagnostics and corrections required the final focus system includes, besides the final doublet and chromaticity corrections, an energy spectrometer, additional absorbers for the particles which scape the collimator, tail folding octupoles, the crab cavities and additional collimators which protect the machine.

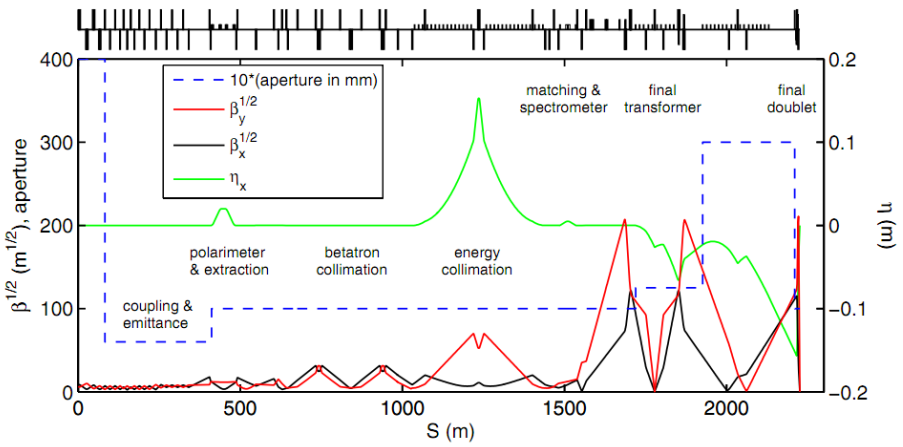


**Figure 2.4:** Final focus optics, from [16].

**Crab Cavities**

At the ILC the electron and positron beam lines meet at the IP with a 14 mrad crossing angle. This is necessary so that the disrupted post-collision beams can be extracted safely, without passing through each other's final focussing quadrupole doublets. In this configuration the collider luminosity is unacceptably reduced by more than 10% relative to the head-on collision case. This loss can be recovered by rotating the bunches, in flight, such that they are aligned at the IP [27].

The bunch rotation is achieved by using a deflecting mode RF cavity phased correctly to provide the rotation without the change in transverse position - a crab cavity. This is operated at the first dipole mode frequency rather than the monopole longitudinally accelerating mode. Further details can be found in Chapter 9, where results of beam dynamics studies including crab cavities at CLIC are presented.

## 2.5 Collider operating parameters

The ILC will operate with a centre of mass energy in the range $200 - 500$ GeV and with a peak luminosity of $2 \times 10^{34}\text{cm}^{-2}\text{s}^{-1}$. Operational experience from existing and decommissioned accelerators and colliders suggests that there will be problems in reaching this ambitious luminosity goal. The RDR, therefore, sets out a number of parameter sets which, taken together, form a parameter plane for the collider operation. Each subsystem has been designed such that the machine can be operated at any point on the plane. Should problems arise with one machine system which limits its performance another system can be "pushed" harder, tensioning the system, but enabling the collider as a whole to meet the luminosity goal. Table 2.3 lists the beam parameters for the nominal case alongside the three extreme cases, (Low N, Large Y and Low P).

### 2.5.1 "Low N"

Low N refers to the bunch population, $N = 2 \times 10^{10}$ in the nominal case. While a larger bunch population is attractive since it increases the luminosity, according to

| Parameter | Symbol/Units | Nominal | Low N | Large Y | Low P |
|---|---|---|---|---|---|
| Repetition rate | $f_{rep}$ (Hz) | 5 | 5 | 5 | 5 |
| Number of particles per bunch | $N$ ($10^{10}$) | 2 | 1 | 2 | 2 |
| Number of bunches per pulse | $n_b$ | 2625 | 5120 | 2625 | 1320 |
| Bunch interval in the Main Linac | $t_b$ (ns) | 369.2 | 189.2 | 369.2 | 480.0 |
| in units of RF buckets | | 480 | 246 | 480 | 624 |
| Average beam current in pulse | $I_{ave}$ (mA) | 9.0 | 9.0 | 9.0 | 6.8 |
| Normalized emittance at IP | $\gamma\epsilon_x^*$ (mm·mrad) | 10 | 10 | 10 | 10 |
| Normalized emittance at IP | $\gamma\epsilon_y^*$ (mm·mrad) | 0.04 | 0.03 | 0.08 | 0.036 |
| Beta function at IP | $\beta_x^*$ (mm) | 20 | 11 | 11 | 11 |
| Beta function at IP | $\beta_y^*$ (mm) | 0.4 | 0.2 | 0.6 | 0.2 |
| R.M.S beam size at IP | $\sigma_x^*$ (nm) | 639 | 474 | 474 | 474 |
| R.M.S beam size at IP | $\sigma_y^*$ (nm) | 5.7 | 3.5 | 9.9 | 3.8 |
| R.M.S bunch length | $\sigma_z^*$ (nm) | 300 | 200 | 500 | 200 |
| Disruption parameter | $D_x$ | 0.17 | 0.11 | 0.52 | 0.21 |
| Disruption parameter | $D_y$ | 19.4 | 14.6 | 24.9 | 26.1 |
| Beamstrahlung parameter | $\Upsilon_{ave}$ | 0.048 | 0.050 | 0.038 | 0.097 |
| Energy loss by beamstrahlung | $\delta_{BS}$ | 0.024 | 0.027 | 0.017 | 0.055 |
| Number of beamstrahlung photons | $n_\gamma$ | 1.32 | 1.48 | 2.18 | 1.64 |
| Luminosity enhancement factor | $H_D$ | 1.71 | 1.48 | 2.18 | 1.64 |
| Geometric luminosity | $L_{geo}$ $10^{34}$ cm$^{-2}$s$^{-1}$ | 1.20 | 1.35 | 0.94 | 1.21 |
| Luminosity | $L$ $10^{34}$ cm$^{-2}$s$^{-1}$ | 2 | 2 | 2 | 2 |

**Table 2.3:** Beam and IP parameters for 500 GeV centre of mass.

Equation 1.4, intense bunches pose problems in the machine. High bunch populations may cause microwave instabilities in the damping rings and raise the possibility of single bunch short range wakefield problems in the main linacs. Further, at the IP a large disruption parameter can cause a kink-instability or undesirable beam-beam effects - a problem for both IP feedback and for the extraction systems. In such cases operational conditions may require reducing the bunch population.

In the Low N set the $N$ is reduced to $1 \times 10^{10}$ with a corresponding shrink in the length of the bunches and is compensated by doubling the number of bunches in a train, with half the bunch spacing. The beam current is kept constant. Stronger

focussing at the IP maintains the nominal luminosity.

In this parameter set the reduced bunch spacing places higher demands on the damping ring extraction kicker as well as the bunch compressor section. Multi-bunch collective effects are also enhanced.

### 2.5.2 "Large Y"

Large Y refers to operating with the vertical emittance, $\epsilon_y$, at the IP greater than the $4 \times 10^{-8}\mathrm{m} \cdot \mathrm{rad}$ specified in the nominal case. Tuning problems in the damping ring or beam delivery system may result in an increased emittance. Main linac wakefields also have the potential to cause emittance dilution and will be discussed in detail in Chapter 4. The design luminosity is recovered with stronger focussing in the horizontal plane at the interaction region and by increasing the bunch length to offset increased beamstrahlung.

### 2.5.3 "Low P"

Problems achieving the required beam power can be overcome by compensating reduced beam current with increased IP focussing. Tight focussing is required in both horizontal and vertical planes, this removes the possibility of increasing the bunch length to offset beamstrahlung, as a result detector backgrounds will likely be increased in this scenario.

## 2.6 Summary

This chapter has detailed the various systems required to produce and maintain a high quality beam for the ILC, as described by the ILC Reference Design Report. Section 2.5 shows that the operational state of the collider will be the result of continual luminosity optimization by tensioning the various collider systems against each other. In this way the optimal luminosity will be delivered at all times.

In the next chapter the systems of the CLIC machine will be briefly introduced and major differences highlighted.

# Chapter 3

# CLIC Overview

The Compact LInear Collider (CLIC) is an international collaboration hosted at CERN and has been under R&D for over 20 years. The project proposes a Linear Collider that will operate at higher energies than the ILC, being designed to reach a centre of mass energy of 3 TeV.

The current design includes 42 km of main linacs equipped with normal conducting copper cavities operating at a frequency of 12 GHz which can achieve an accelerating gradient of 100 MV/m. Such high accelerating field gradients present technological challenges; the cavity structures are highly susceptible to electrical breakdown and long-range wakefield effects. Initial studies showed that a high operating frequency would allow for very high gradients [28, 29] and hence an operating frequency of 30 GHz was first proposed. However, the difficulties in sourcing power to achieve 3 TeV, which would require several thousand klystrons steered the project towards a novel scheme - Two Beam Acceleration (TBA) [30, 29]. In this scheme a low energy high current beam called the drive beam is decelerated in order to extract energy to accelerate the main beam. Studies performed at the CTF3 (CLIC Test Facility), located at CERN, and data collected from NLC/JCL on cavity and related beam parameters were used to determine the best RF frequency and gradient to be used at CLIC. This optimisation process established a gradient of 100 MV/m and a frequency in the vicinity of 14 GHz. In order to be able to use the testing facilities at CFT3 [31] and to benefit from the R&D already performed for the abandoned NLC and JLC it was decided to choose a frequency of 11.9942 GHz. All other subsystems and parameters were chosen to be consistent with this requirements. Table 3.1

| Parameter | Symbol | Value | Unit |
|---|---|---|---|
| Centre of mass energy | $E_{CMS}$ | 3000 | GeV |
| Main Linac RF frequency | $f_{rf}$ | 11.994 | GHz |
| Luminosity | L | $5.9 \times 10^{34}$ | $\mathrm{cm}^{-2}\mathrm{s}^{-1}$ |
| Luminosity (in 1% of energy) | $L_{99\%}$ | $2 \times 10^{34}$ | $\mathrm{cm}^{-2}\mathrm{s}^{-1}$ |
| Linac repetition rate | $f_{rep}$ | 50 | Hz |
| Number of particles per bunch | $N$ | $3.72 \times 10^{9}$ | |
| Number of bunches per pulse | $N_b$ | 312 | |
| Bunch separation | $\Delta t_b$ | 0.5 (6 periods) | ns |
| Bunch train length | $\tau_{train}$ | 156 | ns |
| Beam power / beam | $P_b$ | 14 | MW |
| Unloaded / loaded gradient | $G_{un/l}$ | 120/100 | MV/m |
| Overall two linac length | $l_{linac}$ | 42.16 | km |
| Total Beam delivery length | $l_{BD}$ | 48.4 | km |
| Total site AC | $P_{tot}$ | 582 | MW |

**Table 3.1:** Overall CLIC parameters [7].

summarises the main parameters for CLIC .

## 3.1 Comparison with ILC

Figure 3.1 shows a schematic of the overall CLIC machine layout for the 3 TeV case. While many systems are familiar from the ILC design, see Figure 2.1, there are a number of novel systems. The bulk of the new systems concern the Drive Beam creation and the power extraction and transfer structures (PETS). The low energy but high current drive beam is created by interleaving and combining sub-pulses, using the Delay Loop and Combiner Rings into single large, highly intense, bunches. The drive beam is generated at the centre of the complex and sent via long transfer lines to the end of the main linac. The beam consists of 24 short bunch trains of 243.7 ns length with a spacing of 60 cm. The total length of the drive beam for

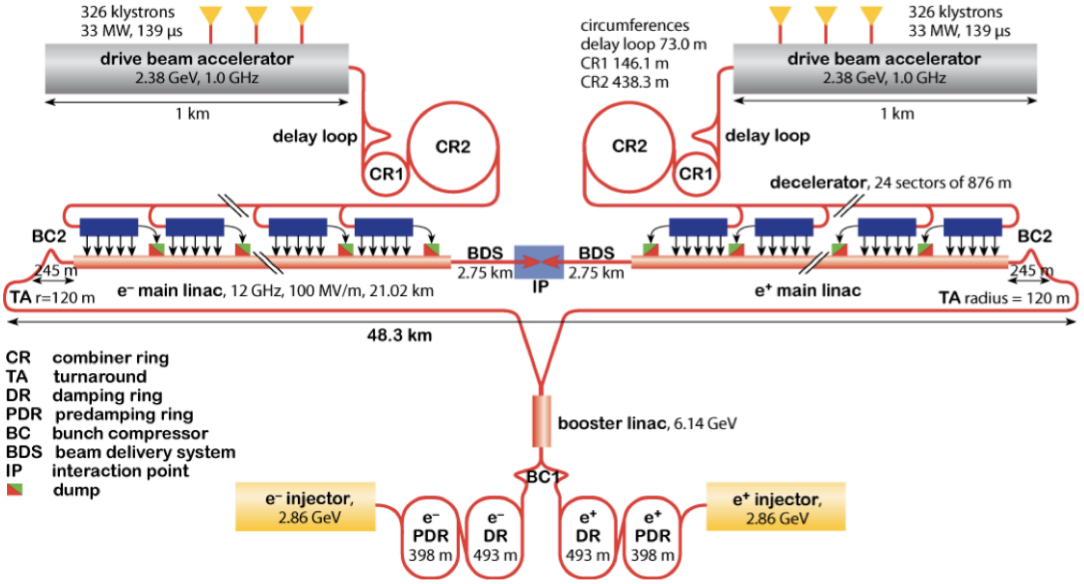


**Figure 3.1:** Schematic of the overall layout of CLIC for 3 TeV centre of mass [32].

one acceleration is 140 $\mu$s and the total current at this stage is 4.2 A. This pulse is input into the delay loop where even and odd buckets of the bunches are separated using an rf deflector. Each even bunch is delayed with respect to the following odd bunch by 240 ns. A second rf deflector recombines the bunches thus producing a final bunch whose intensity is increased by a factor of two. This process is shown in Figure 3.2. A similar process takes place on the combiner rings where interleaving the bunches finally leads to an increase by a factor of four. In this way a low energy high current (101 A) beam is available at the linac entrance to power the main accelerating structures.

RF power is extracted from the beam by Power Extraction and Transfer Structures (PETS). When the beam passes through an RF structure it will excite RF fields in this structure, thus losing some of its kinetic energy. The beam excited field in the PETS is sent via waveguides to the accelerating structures in the main beam. Each of the 35,784 PETS is designed such that it extracts 136 MW peak power, enough to feed two accelerating structures.

On the Main Beam side, the beam which is used for particle physics studies, the arrangement is closer to that of the ILC, although there is an extra Pre-damping

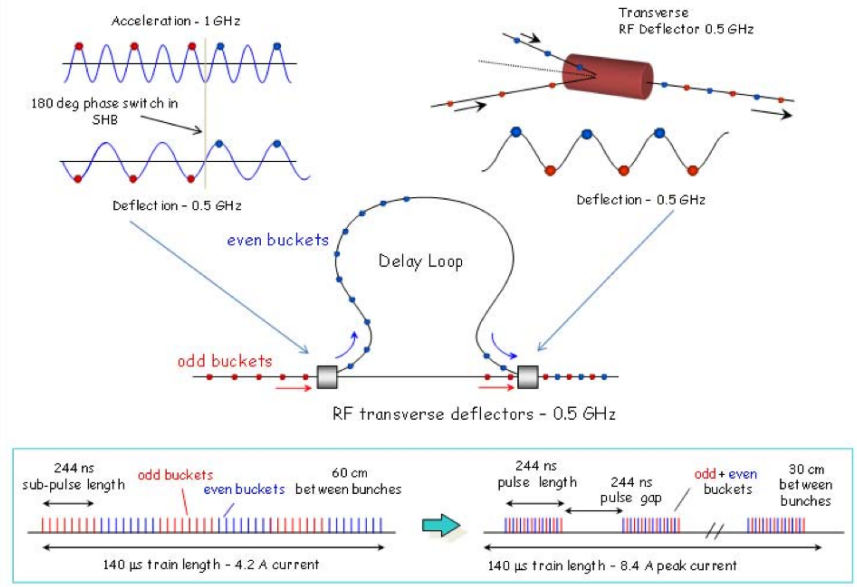


**Figure 3.2:** Full drive beam complex (not to scale)[7].

ring [33]. Electrons and positrons with energy of 2.4 GeV are injected into the two sets of damping rings, the pre-damping and the damping rings in order to reduce bunch emittance. Then the beams pass through the bunch compressor where bunch lengths are reduced in a two stage process. At the entrance to the main linac the bunches have a length of 44 $\mu$m and an energy of 9 GeV.

The operating regime is very different to that of the ILC. The CLIC cavities operate at 12 GHz and have iris sizes of just 4 mm, compared to 35 mm for TESLA cavities. The bunch train consists of 312 bunches separated by 0.5 ns. Compared to ILC's 2625 bunches and 369 ns spacing. In the CLIC regime the reduced iris dimension results in a much more intense wakefield (see Chapter 4). Equally the very short spacing between bunches necessitates very strong higher order mode damping in order to suppress the long range wakefields.

The beam delivery system is similar in design to that of the ILC, bringing the low emittance bunches to an interaction point with a crossing angle of 20 mrad. The presence of the crossing angle in the design leads to the inclusion of a crab cavity system to rotate the bunches prior to collision, just as in the ILC. Crab cavities are discussed in more detail in Chapter 9.

## 3.2 Summary

This chapter has presented a brief overview of the CLIC main systems, sufficient to point out the major differences with respect to the ILC. In the next chapter wakefields are described in detail. This is the theory which underpins the results presented in this thesis.

# Chapter 4

# Wakefields

Wakefields have the potential to seriously degrade the quality of a charged particle beam by deflecting particles off-axis. Adequate control of cavity wakefields during acceleration is essential to maintaining a low emittance, high luminosity beam for future linear colliders. Here we introduce the theory underpinning the research presented in this thesis. Calculations of the wakefields described here will be presented in Chapter 7.

## 4.1 Introduction to Wakefields

An observer situated at a distance $b$ perpendicular to the trajectory of a point charge $q$ moving in free space with velocity $\mathbf{v}$ near the speed of light will measure a Lorentz contracted electromagnetic field. The longitudinal and transverse components of the field carried by this relativistic point charge can be expressed as [34]:

$$\begin{aligned}
\mathbf{E}_{\parallel}(b,t) &= -\frac{q}{4\pi\epsilon_0}\,\frac{\gamma v t}{[b^2+(\gamma v t)^2]^{2/3}}\mathbf{e}_{\parallel},\\
\mathbf{E}_{\perp}(b,t) &= \frac{q}{4\pi\epsilon_0}\,\frac{\gamma b}{[b^2+(\gamma v t)^2]^{2/3}}\mathbf{e}_{\perp},\\
\mathbf{B}_{\perp}(b,t) &= \frac{1}{c^2}\,\mathbf{v}\times\mathbf{E}_{\perp}(b,t),
\end{aligned}$$

where the relativistic factor $\gamma$ is defined by $\gamma = \frac{1}{\sqrt{1-(v/c)^2}}$, $E$ is the electric field, $B$ the magnetic, $\mathbf{e}_{\perp}$ and $\mathbf{e}_{\parallel}$ are unit vectors perpendicular and parallel to the beam axis $z$.

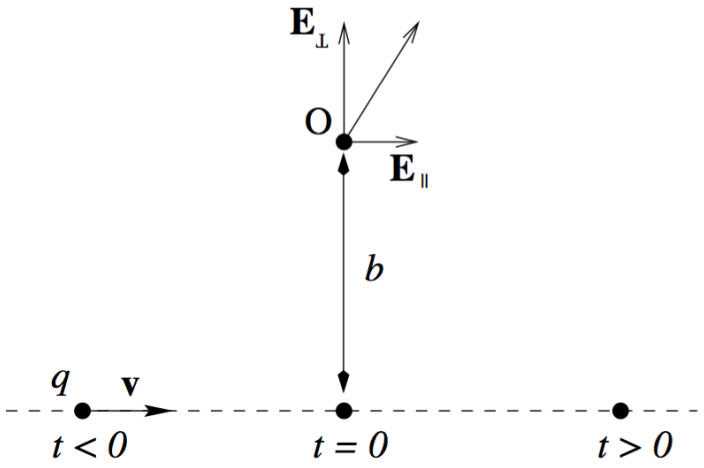


**Figure 4.1:** A charge $q$ moving with velocity $v$ crosses the observation point O at a distance $b$.

The amplitude of the transverse electric field, as seen by the observer, is an even function of time and it reaches its peak value when the particle crosses the point O, which is labelled $t = 0$ in Figure 4.1

$$\mathbf{E}_{\perp}(b, 0) = \frac{q}{4\pi\epsilon_0}\frac{\gamma}{b^2}\mathbf{e}_{\perp}, \tag{4.2}$$

which is dependent on the relativistic factor.

The longitudinal field is an odd function of time and it reaches its peak value for the time interval

$$\Delta t \approx \frac{\sqrt{2}}{2}\frac{b}{\gamma v}. \tag{4.3}$$

The value of the maximum amplitude is

$$\mathbf{E}_{\parallel}(b, \Delta t) = \frac{q}{4\pi\epsilon_0}\frac{2\sqrt{2}}{3^{3/2}b^2}\mathbf{e}_{\parallel}, \tag{4.4}$$

which is independent of the relativistic factor $\gamma$. Therefore the opening angle of the resultant electric field, $\theta$, is given by

$$\tan\theta = \frac{\mathbf{E}_{\parallel}}{\mathbf{E}_{\perp}} \tag{4.5}$$

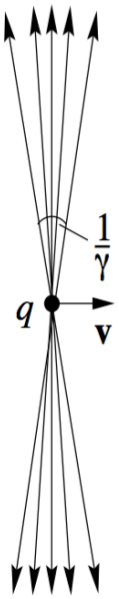


**Figure 4.2:** Electric field associated with a relativistic point charge moving in free space with velocity $v$.

and hence for relativistic particles, $\gamma \gg 1$, this angle is of the order of $1/\gamma$.

In the ultra-relativistic limit, when $v \to c$ and hence $\gamma \to \infty$ the field becomes a Dirac - delta distribution with a magnetic and an electric component in the transverse direction

$$\mathbf{E} = \frac{q}{2\pi\epsilon_0 r}\,\delta(z - ct)\mathbf{e}_\perp, \qquad \mathbf{B} = \frac{1}{c}\,\mathbf{E}. \tag{4.6}$$

The electromagnetic distribution described in Equation 4.6 is the distribution produced by a charged particle travelling in free space. The field is perpendicular to the trajectory with no field either in front or behind the charge. Therefore, a second particle, or a bunch, moving behind on the same or a parallel trajectory within an small distance will experience no forces from the fields produced by the leading charge.

When the charged particles are not moving in free space the situation changes. In the linacs of the ILC electron and positron beams travel through accelerating cavities. The field produced by the first charge, the driving charge, is scattered

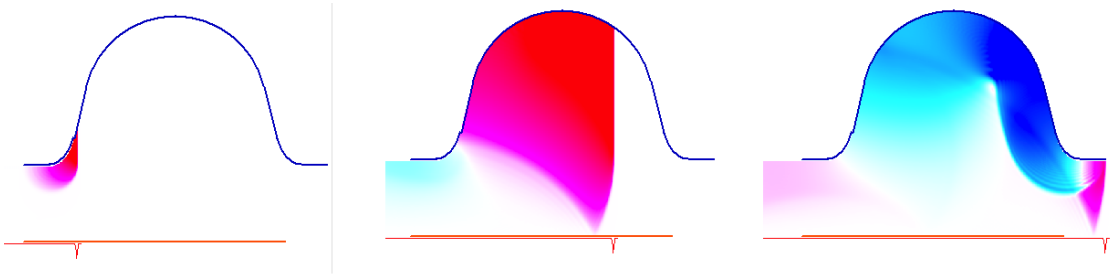

**Figure 4.3:** Wakefield generated when a Gaussian bunch passes a change in geometry. Shown at three different times. This figure was produced using the code ECHO-2D [36].

by geometrical discontinuities in the cavity. The particles travelling behind, the trailing particles, are then affected by the scattered radiation. These scattered fields, examples of which are shown in Figure 4.3, are defined as wakefields and have both longitudinal and transverse components [14].

There can be other sources of wakefields besides geometric discontinuities. The non-vanishing resistivity of the walls of the cavities gives rise to resistive wakefields [35]. In a perfect conductor the transverse electric field lines terminate on surface charges on the walls, and these charges move in synchronism with the driving charge. The resistivity of the metallic walls means that the surface charges will lag slightly behind. The magnetic field and the surface currents will diffuse into the cavity walls and hence affect the passage of the trailing both in the transverse and longitudinal direction. The integrated effects of these wakefields over a given path for the trailing charges give rise to longitudinal and transverse wake potentials.

## 4.2 Causality and The "Catch-up" Distance

The effects of the wakefield produced by scattering from discontinuities in the cavity walls on the trailing charges will depend on the distance separating the driving and test particles and their velocity.

The wakefield produced by an ultra-relativistic particle ($v \approx c$) by scattering from a small metallic obstacle is shown in Figure 4.4. For a test particle, moving a distance $s$ behind the driving charge, to experience the radiated wakefield it has to

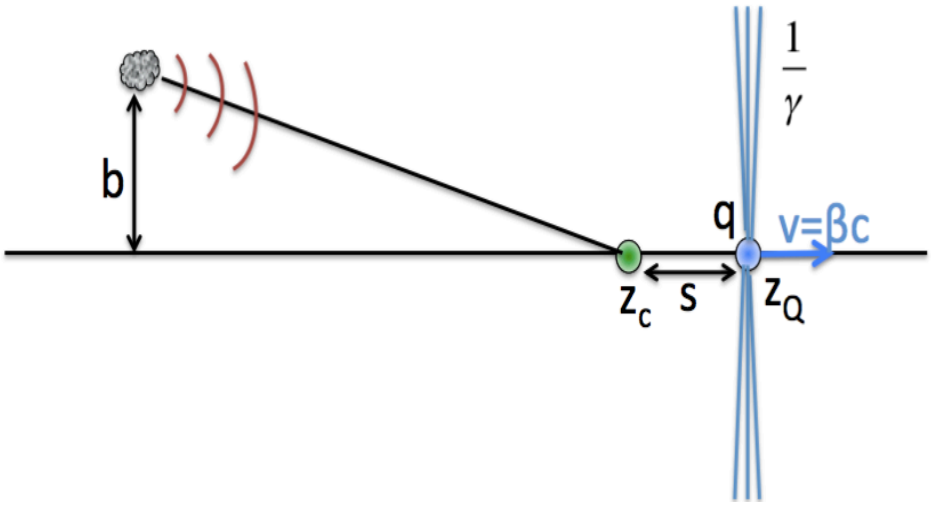


**Figure 4.4:** Field of a relativistic particle moving along the $z-$axis and field scattered by a perturbing metallic object.

reach position $z_c$. This "catch-up" distance is given by [14]

$$z_c \approx \frac{b^2 - s^2}{2s} \tag{4.7}$$

and for a small distance $s$ it can be significantly large. At the ILC, taking $s$ to be the RMS bunch length of 300 $\mu$m and $b = 35$ mm, the beam pipe radius at the entrance to an accelerating cavity, the catch-up distance $z_c = 2.04$ m. This implies that fields scattered due to the head of the bunch will not interact with the tail of the bunch until the bunch has exited the cavity itself.

Causality implies that there can be not disturbance ahead of a charged particle traveling at the speed of light [37]. However, for particles moving with a speed $v < c$ an electromagnetic field exits ahead of the driving charge. The wake potential derived for a particle moving at speed $v = c$ can be practical for ultra-relativistic particles with a relativistic factor $\gamma$ large enough so that over the times of interest the distance traveled the radiation ahead of the charge is small compared to the bunch lengths [35]. Thus, taking into account the finite nature of $\gamma$, one can calculate the distance for the scattered radiation to catch up to the exciting charge itself, which is given by:

$$b^2 + z_c^2 = z_c^2/\beta^2 \tag{4.8}$$

or,

$$z_c \approx \gamma b. \tag{4.9}$$

## 4.3 Wakefield effects and Wake potentials

In the study of beam dynamics one is normally more interested in the integrated effect of the wakefield produced by the driving charge on the trailing particles as they both pass through a structure, than in the details of the wakefields themselves. These integrated effects are defined as the wake potentials. The effects of the transverse and longitudinal wake potentials are usually studied separately since the motion of charged particle in the transverse and longitudinal planes is, to a very good approximation, decoupled [38, 39].

The longitudinal wake potential is the integrated effect of the electric field created by a driving charge on a unit trailing charge. The transverse potential is the transverse momentum kick experienced due to the deflecting fields. These potentials are sometimes referred in the literature as wake functions or delta wake potentials, defined as the wake potential per unit charge, which defines a Green's function for the potential (see Appendix A).

The effects of the wakefields on the trailing particles depends on the distance between the driving and the test particle, as illustrated in Section 4.2. In the linacs of the ILC particles are grouped in bunches, with bunches separated by $\sim$ 100 m. Hence, at small distances one is looking at the effect of the driving charge on the charges within the same bunch. This is what is called the short-range wakefield and it mainly affects the shape of the bunch producing an increase in the emittance. Long-range wakefields affect the bunches trailing behind the leading bunch and will be the main concern of the work presented in this thesis.

### 4.3.1 Longitudinal Wake potential

The integrated longitudinal field seen by a test charge at a distance $s$ behind a driving charge $q$ is given by:

$$\mathbf{W}_{\parallel}(\mathbf{r}, \mathbf{r}', s) = -\frac{1}{q} \int_{z_1}^{z_2} dz\, E_z(\mathbf{r}, z, t)_{t=(z+s)/c}\,, \tag{4.10}$$

where $\mathbf{r}, \mathbf{r}'$ represent the transverse offset of the test and driving charge respectively and both particles are moving parallel to the $z$ axis. The driving charge enters the cavity at $z = 0$ and exits at $z = L$ and the test particle enters at $z = z_1$ and exits at $z = z_2$.

This potential represents the response to a point a charge and can be used as the Green's function to calculate the potential within and behind a line density charge distribution with charge density $\lambda(s)$ (see Appendix A) [14]

$$V_{\parallel}(s) = \int_0^{\infty} ds'\, \lambda(s - s')\, W_z(s') \;=\; \int_{-\infty}^{s} ds'\, \lambda(s')\, W_{\parallel}(s - s') \tag{4.11}$$

This longitudinal bunch potential is used to calculate the total energy lost by the driving charge to the wakefield

$$\Delta U = \int_{-\infty}^{\infty} ds\, \lambda(s)\, V_{\parallel}(s) \;=\; \int_{-\infty}^{\infty} d\tau\, I(\tau)\, V_{\parallel}(\tau), \tag{4.12}$$

where $\tau = s/c = t - z/c$ and $I(\tau) = c\lambda(s)$ is the current flow within the charge distribution. It is usual to define the loss factor, which represents the energy lost per unit charge square:

$$k_{\lambda} = \frac{\Delta U}{q^2}. \tag{4.13}$$

The wake potential can be calculated by solving Maxwell's equations either in the time or in the frequency domain. Because the wakefield in the time domain far behind the bunch requires significantly increased computational efforts the frequency domain is usually chosen. A method for calculating the wakefields in a charge free cavity was introduced by Condon [40] and has been widely used. In the Condon method the vector and scalar potentials for the driving charge are expanded in terms

of the potentials for the normal modes of the cavity using the Coulomb gauge. The details of the Condon method are shown in Appendix B. Using this method one finds the following expression for the wake potential and the loss factor :

$$W_{\parallel}(s) = \mathrm{A}\sum_{\lambda} k_{\lambda}\cos(\frac{\omega_{\lambda}s}{c}) \begin{cases} \mathrm{A}=0 & s<0 \\ \mathrm{A}=1 & s=0 \\ \mathrm{A}=2 & s>0 \end{cases} \tag{4.14}$$

with

$$k_{\lambda} = \frac{|V_{\lambda}|^2}{4U_{\lambda}}. \tag{4.15}$$

### 4.3.2 Transverse wake potential

The transverse wake potential is defined as the transverse momentum kick experienced by a test charge moving a distance $s$ behind a driving charge $q$ following the same path.

$$\mathbf{W}_{\perp}(\mathbf{r},\mathbf{r}',s) = \frac{1}{q}\int_{z_1}^{z_2} dz\,(E_{\perp} + c(\mathbf{e}_z \times \mathbf{B})_{t=(z+s)/c} \tag{4.16}$$

As in the case of the longitudinal potential $\mathbf{W}_{\perp}$ can be used as a Green's function for transverse momentum kick per total charge within an ultrarelativistic bunch

$$V_{\perp}(s) = \int_0^{\infty} ds'\,\lambda(s-s')\,W_{\perp}(s') \;=\; \int_{-\infty}^{s} ds'\,\lambda(s')\,W_{\perp}(s-s') \tag{4.17}$$

The transverse quantity analogous to the loss factor is the transverse impulse factor defined by:

$$k_{\perp} = \frac{1}{q^2}\int_{-\infty}^{\infty} ds\,\lambda(s)\,V_{\perp}(s) \tag{4.18}$$

The total momentum kick experience by the charge distribution is $p_{\perp} = q^2 k_{\perp}/c$.

Similarly to the case of the longitudinal potential the Condon method can be used to obtain an expression of the transverse wake potential in terms of the sum of the eigenmodes of the cavity:

$$W_{\perp}(s) = \mathrm{A}\sum_{\lambda}\frac{k_{\lambda}}{\omega/c}\sin(\frac{\omega_{\lambda}s}{c})\begin{cases}\mathrm{A}=0 & s<0\\ \mathrm{A}=1 & s=0\\ \mathrm{A}=2 & s>0\end{cases} \tag{4.19}$$

Panofsky and Wenzel, in 1956, provided another method of calculating the transverse wakefield [41]. The result is outlined in Appendix C. With it we can derive the transverse fields directly from the longitudinal wake, this technique is employed in many simulation codes.

It is worth noting that the potential experienced by the driving charge due to the fields it induces is not equal to that experienced by the trailing charges or bunches. The two are related by the Fundamental Theorem of Beam Loading, derived in the following section.

### 4.3.3 Fundamental Theorem of Beam Loading

The fundamental theorem of beam loading relates the energy lost by a charge passing through a cavity to the electromagnetic properties of modes of the cavity. Superposition tells us that the beam induced voltage in a cavity is independent of the presence of a generator voltage component, and therefore this theorem can be used to calculate the effective voltage acting on a bunch when both a generator voltage and a beam induced voltage are present.

Consider two charges traveling through a cavity separated by a distance equal to half the wavelength of the cavity. The driving charge $q$ crosses an unexcited cavity and generates a voltage. After the charge has passed a beam induced voltage $V_b$ and a corresponding stored energy remain in each mode.

$$V_c = -V_b, \tag{4.20}$$

where $V_c$ is the cavity voltage. By energy conservation the energy lost by the particle must be equal to the work done ($W$) by the induced voltage on the charge.

$$W = qV_b \tag{4.21}$$

The induced stored energy is:

$$U = \alpha V_b^2 \tag{4.22}$$

where $\alpha$ is a proportionality constant. Assuming that the potential experienced by the driving charge itself, $V_e$, is some fraction, $f$, of the induced voltage $V_b$

$$V_e = fV_b \tag{4.23}$$

we obtain

$$U = \alpha V_b^2 = W = qfV_b \tag{4.24}$$

Half a period later when the second charge enters the cavity the voltage induced by the driving charge has changed it phase by $\pi$ so now $V_c = V_b$ and therefore no stored energy will remain in the cavity. The voltage induced by the trailing particle ( $V_{b2}$) adds to the first induced voltage to give a total voltage seen by the second charge. Assuming as before that the charge experiences a fraction $f$ of its induced voltage $V_b$

$$W_2 = -qfV_{b2} + qV_b \tag{4.25}$$

Applying conservation of energy and taking into account that $V_b = V_{b2}$ we get:

$$W_1 + W_2 = -qfV_b - qfV_b + qV_b = 0 \tag{4.26}$$

which gives $f = 1/2$ and thus

$$V_e = \frac{V_b}{2}. \tag{4.27}$$

The fundamental theorem of beam loading tells us that the potential, $V_e$, experienced by the driving charge, or bunch, is half of that the seen by the trailing charge, or bunch.

In the next section we will consider the details of the fields acting on trailing particles with a bunch.

### 4.3.4 Short-Range Wakefields

The wake potential induced by the driving charge of a bunch affects the trailing charges within the bunch, this is the effect of the short-range wakefield or intra-bunch wakefield. The bunch will experience both longitudinal and transverse fields. The longitudinal short-range wakefield changes the energy of the charges. An increase of the energy spread of the bunch results from the longitudinal wakefield's dependence on the charge positions. The transverse wakefield tends to deform the shape of the bunch and the combined effects of the fields lead to an increased emittance and hence to a decrease in the luminosity.

The main contributions to the transverse wakefield come from dipole modes and are inversely proportional to the square of the average aperture radius of the accelerating cavities [42, 43]. For quadrupole modes the field will depend on the fourth power [44].

At the short time and distance intra-bunch scales accurately calculating the wakefield according to Equation 4.19 requires knowledge of a very large number of modes, to very high frequency. In all but the simplest cases we must employ codes to calculate these modes numerically, so the computational demands are extreme. Further, as we will see in Chapter 6, the solution accuracy degrades as modes become higher in frequency, for a fixed mesh size. If we must work in the frequency domain then the lower part of the mode spectrum, calculated with e.g. a finite difference code can be supplemented with high-frequency dependence derived from the Optical Resonator Model due to Sessler and Vaynstein as described in [45, 46]. This is an application of theory used extensively in laser physics [47] to describe the diffraction of light trapped between two mirrors - the resonator. Here the analogous system is the array of cavity irises and the wake function has been calculated by Bane [48]. Its application is beyond the scope of this thesis and the reader is directed to the book by Zotter [49].

Intra-bunch effects are of particular concern where the catch-up distance is small, such as in collimator structures. Here the bunch passes extremely close to the metal surface and the frequency domain, modal summation, approach is not appropriate.

The solution here, as for the previously mentioned cavity case in the high frequency limit, is make use of a time domain code and calculate the wakefield response to the passage of a charged bunch directly. Many codes are available, notably GdfidL, ECHO [36] and ABCI [50].

In the next section we will consider the wakefield effect of one bunch on the following bunches.

### 4.3.5 Long-Range Wakefields

The power law described in the previous section marks the difference between physics in the ILC linacs and in CLIC for example. With an iris radius of 35 mm for TESLA cavities and the order of 4 mm for CLIC 12 GHz cavities the wakefields are much more intense in the case of CLIC [51]. However, there is another factor to consider. At CLIC bunch trains have approximately 100 bunches, compared to ILC's nominal of 2625 bunches in a single train. Bunches are separated by 369 ns (110.7 m) at ILC leading to a beam train which, unwrapped, would be 290 km long. This truly is the regime of the bunch-to-bunch long-range wakefield where a limited number of dominant modes contribute. The vast majority, adding with arbitrary phases, approximately cancel each other out [49].

To ease calculation and to provide a more natural measure we often work with dipole mode "kickfactors" $K$. This has units of V/C/m/m and is quoted per unit length of iris radius, per unit length of the cavity in V/C/mm/m. The kickfactor is defined thus:

$$K = \frac{|V|^2}{4U\frac{\omega}{c}Lr^2} \tag{4.28}$$

For $s > 0$ Equation 4.19 now becomes [52]:

$$W_\perp(s) = 2\sum_\lambda K_\lambda \sin\left(\frac{\omega_\lambda s}{c}\right)\exp\left(\frac{-\omega_\lambda s}{2Q_\lambda c}\right) \tag{4.29}$$

where we have also taken account of damping due to natural losses and external coupling. $Q_\lambda$ is the quality factor for the mode $\lambda$ given by the ratio of the energy stored in the mode to the energy lost in a single cycle (multiplied by $2\pi$).

For superconducting cavities these quality factors can be extremely large, of the order of $10^6$. This is beneficial for the efficiency of the collider in the case of

the fundamental operating mode ($Q$ is even higher here at $10^{10}$) but high $Q$s for deflecting modes can cause serious problems, including beam break up (BBU) [52].

The leading bunch dumps energy into the cavity, exciting the continuum of dipole modes, and then exits to continue down the linac. The modes excited continue to 'ring' in the cavity with their distinct frequency. Trailing bunches arrive some time later, in principle many cycles for the dipole modes, but energy remains in the transverse fields.

Another useful quantity often quoted for dipole modes is the $R/Q$. It is related to the loss factor and kick factor and quoted in units of Ohms per cm$^2$:

$$\frac{R}{Q} = \frac{1}{r^2}\frac{2k_{\text{loss}}(r)}{\omega} \tag{4.30}$$

The next chapter introduces the designs for the Reentrant and Ichiro accelerating cavities, as well as the nature of the superconducting Niobium material which leads to their particular geometry. The perturbations to the beam line which these cavities represent are responsible for generating the wakefields discussed above.

# Chapter 5

# Superconducting Cavity Design

Superconducting cavity technology offers significant advantages over the normal conducting room temperature copper cavities, however, the nature of the superconducting material Niobium requires careful work to produce an optimal cavity geometry and required surface morphology. Cavities which maximise the accelerating gradient despite the limitations which will be discussed in this chapter. Here we will discuss the properties of Niobium, fabrication techniques, emission of electrons from cavity walls due to high surface electric field, localized temperature rise and quenching. The cavity designs of particular interest in this thesis, namely the TESLA , Ichiro and Reentrant cavities, have arisen when focus on one or more of the above effects has driven the design process.

## 5.1 Superconductivity in Niobium

At room temperature Niobium metal is a poor electrical conductor but cooling the metal to below a critical temperature, $T_C = 9.2$ K, allows superconducting behaviour according to the BCS theory [53]. At this temperature electrons near the Fermi surface experience an attractive force due to the interaction with the lattice, which binds them in pairs, called Cooper pairs [54]. These pairs can be regarded as new particles with boson-like properties, rather than fermions which must obey the Pauli exclusion principle, and thus the pairing opens a gap in the energy spectrum of the electrons, $\Delta(0)$. This energy gap inhibits the interactions which cause electrical resistivity and therefore for sufficiently low temperatures,

i.e. temperatures such that the thermal energy is less than the band gap, the material exhibits zero resistivity. Since the number of unpaired electrons decreases exponentially with temperature according to the BCS theory the surface resistance in the proximity of the critical temperature can be expressed as [55]:

$$R_{\mathrm{BCS}}(T) = A_s\,\omega^2 \exp\left(-\frac{\Delta(0)}{k_B T}\right), \tag{5.1}$$

where $A_s$ is related to the properties of the specific material, $\omega$ is the operating frequency and $k_B$ is the Boltzmann constant.

In the superconducting state the DC (direct current) resistance is zero however there is still an AC (alternating current) resistance. The source of this resistance is an interaction between the superconducting Cooper electron pairs and their normal counterparts in the metal surface which dissipates energy and it is therefore dependent on the operating temperature. It can be expressed as the sum of the temperature dependent resistance, $R_{BCS}$, and a temperature independent residual surface resistance:

$$R_s(T) = R_{BCS} + R_0, \tag{5.2}$$

The residual surface resistance $R_s$ depends on the residual magnetic field and the purity of the material. Impurities in the material affect not only its resistivity but also its thermal conductivity. A parameter used to indicate the purity of a superconductor is the Residual Resistivity Ratio (RRR), which is defined as the ratio of the resistivities at room temperature to that at liquid helium temperature (4.2 K)

$$\mathrm{RRR} = \frac{\rho_{300K}}{\rho_{4.2K}}. \tag{5.3}$$

The higher the value of RRR the higher the purity of the material.

The thermal conductivity, $\lambda$ of niobium at cryogenic temperatures varies with RRR as:

$$\lambda(4.2K) \approx 0.25\,\mathrm{RRR}, \tag{5.4}$$

The thermal conductivity is strongly dependent on the temperature, decreasing by about an order of magnitude for a temperature change from 4 K to 2 K. A good thermal conductivity is important in the choice of material since the heat produced at the inner cavity surface has to be evacuated to the helium bath. A niobium purity of RRR = 300 was chosen for the ILC cavities [16].

Another important feature of the behaviour of superconducting materials successfully explained by the BCS theory is the Meissner effect [56, 57]. Magnetic field is expelled by material which is superconducting but only up to a critical field limit. Once the field limit is reached the superconductivity breaks down and the material becomes normal conducting once more. Large electric currents, induced by the RF field in the cavity, then cause Joule heating in this normal conducting region, which warms the surrounding material - again causing superconductivity to break down. In this way a critical loss of superconductivity rapidly occurs - this is known as a "quench". For a typically prepared Niobium sample this critical surface magnetic field ($H_{crit}$) is observed experimentally in the range 165 to 185 mT, though the theoretical limit is higher at 230 mT [58].

## 5.2 Figures of Merit

The primary aim for all physicists and engineers designing accelerating cavities for the ILC is to maximise the accelerating gradient $E_{acc}$. The length of the main linac tunnel and the number of cavities required to generate the 250 GeV beams is the main cost driver for ILC. Therefore, even a modest improvement in reproducible accelerating gradient could represent a significant cost saving.

The peak surface electric field ($E_{pk}$) and the peak magnetic field on the surface ($H_{pk}$) are the factors limiting the achievable gradient [55]. Both quantities increase proportional to the maximum $E_{acc}$. The geometry of the cavity determines the constant ratios $E_{pk}/E_{acc}$ and $H_{pk}/E_{acc}$ - these are the figures of merit used.

The TESLA cavity shape was optimized, in the first instance, to minimize $E_{pk}/E_{acc}$ to reduce field emission of electrons, which rises exponentially with $E_{pk}$. There is, however, no known critical limit to the surface electric field at which su-

perconductivity breaks down. Multiple cavities have been operated since 1992 with $E_{pk}$ in excess of 100 MV/m [59, 60, 61]. Practical, repeatable control of field emission has been achieved through improved cavity preparation "recipes". Processing includes high pressure water rinsing to remove surface particulate contamination [62] and electropolishing to achieve an ultra-smooth inner surface [63].

Designs which seek to reduce $H_{pk}$ have become common since 2002. Reports from Cornell proposed a Reentrant shape [64, 65] and separately a "Low Loss" shape was proposed by JLAB for the upgrade to the CEBAF linac [66]. Although operating at a different frequency the geometry has been scaled down to match 1.3 GHz dimensions and forms the basis for the Ichiro design.

$$E_{acc}^{max} = \frac{H_{crit}}{H_{pk}/E_{acc}} \tag{5.5}$$

Equation 5.5 relates the maximum achievable accelerating gradient to the critical surface magnetic field and the ratio $H_{pk}/E_{acc}$ determined by the cavity geometry. We can either increase the critical field sustainable, by switching a different material such as $Nb_3Sn$, or change the cavity geometry such that $H_{pk}/E_{acc}$ is reduced.

## 5.3 TESLA cavity

| Cavity shape parameter | Symbol | Midcup | Endcup1 | Endcup2 |
|---|---|---|---|---|
| Equator radius | $R_{equat}$ | 103.3 | 101.3 | 103.3 |
| Iris Radius | $R_{iris}$ | 35 | 39 | 39 |
| Radius of circular arc | $R_{arc}$ | 42.0 | 40.3 | 42 |
| Horizontal half axis | $a$ | 12 | 10 | 9 |
| Vertical half axis | $b$ | 19 | 13.5 | 12.8 |
| Length | $l$ | 57.7 | 56.0 | 57.0 |

**Table 5.1:** Half cell shape parameters for the TESLA cavity. Dimensions are in mm.

The TESLA cavity is made up of three types of elliptical cell. Of the 9 full cells, the inner 16 half-cells are identical. The dimensions are listed in Table 5.1 under the

title "Midcup". The outer half-cells at each end of the cavity are custom designs and leave the cavity longitudinally asymmetric in order to promote dipole mode damping.

The contour of each cell is made up of a circular arc at the equator (the widest part of the cell) and an elliptical section at the iris (the narrowest). The two curves are smoothly linked by a straight section which is tangent to both curves.

The contour is sketched in Figure 5.1. The TESLA cavities are the base-line for

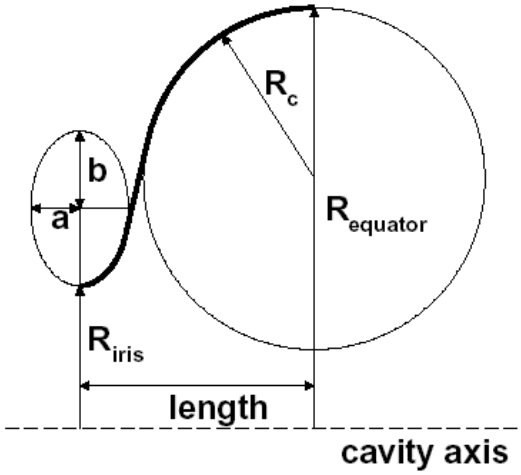


**Figure 5.1:** Sketch showing the contour of the TESLA cavity cells.

the ILC, operating with a peak gradient of 35 MV/m and sustained performance of 31.5 MV/m.

## 5.4 Reentrant cavity

There are multiple Reentrant cavity designs for 1.3 GHz operation. The design simulated in this thesis originates from a paper by Luk, Shemelin & Myakishev [67]. The cell parameters are listed in Table 5.2. This is a longitudinally symmetric design, with iris radius matching that of the TESLA cavity at 35 mm. The contour is shown in Figure 5.2.

The major feature of the Reentrant designs is that the tangent section present in the TESLA and Ichiro contours has been eliminated. The contour is made up of two conjugate ellipses, smoothly matched into each another.

| Cavity shape parameter | Symbol | Midcup | Endcup |
|---|---|---|---|
| Equator radius | $R_{equat}$ | 98.710 | 98.710 |
| Iris Radius | $R_{iris}$ | 35 | 35 |
| Horizontal half axis | $A$ | 51.56 | 53.53 |
| Vertical half axis | $B$ | 36.22 | 42.79 |
| Horizontal half axis | $a$ | 9.16 | 4.59 |
| Vertical half axis | $b$ | 11.92 | 7.743 |
| Length | $l$ | 57.652 | 56.238 |

**Table 5.2:** Half cell shape parameters for the Reentrant cavity. Dimensions are in mm.

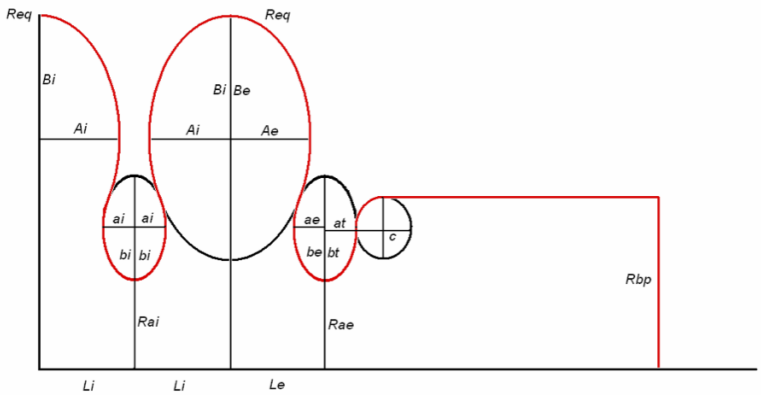


**Figure 5.2:** Sketch showing the contour of the Reentrant cavity cells. From [67].

In addition, the design simulated in this thesis contained modified end cells in which the beam pipes had been expanded to 50 mm to improve HOM extraction. This technique had also been used in the design of the two-cell cavity for the ERL injector at Cornell [67].

Single cell cavities fabricated at Cornell and KEK have demonstrated gradients in excess of 47 MV/m.

## 5.5 Ichiro cavity

The Ichiro cavity contour is displayed in Figure 5.3.

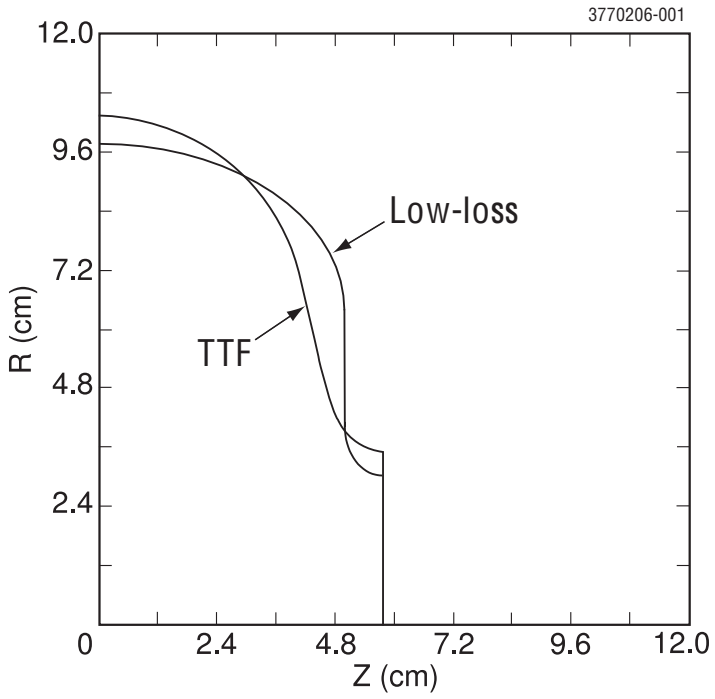


**Figure 5.3:** Sketch showing the contour of the Ichiro (Low Loss) cell compared to TESLA (TTF). From [68].

In this case both the equator region and the iris are defined by ellipses. The two curves are joined by a straight section perpendicular to the longitudinal axis of the cavity. The 8 inner cells of this design are identical while the matching end cells differ. The cell parameters are listed in Table 5.3.

| Cavity shape parameter | Symbol | Midcup | Outer End Cup | Inner End Cup |
|---|---|---|---|---|
| Equator radius | $R_{equat}$ | 98.151 | 98.835 | 98.835 |
| Iris Radius | $R_{iris}$ | 30 | 40 | 30 |
| Horizontal half axis | $A$ | 50.052 | 50.052 | 50.052 |
| Vertical half axis | $B$ | 34.222 | 34.906 | 34.906 |
| Horizontal half axis | $a$ | 7.60 | 7.60 | 7.60 |
| Vertical half axis | $b$ | 9.945 | 10.0 | 9.945 |
| Length | $l$ | 57.652 | 57.652 | 57.652 |

**Table 5.3:** Half cell shape parameters for the Ichiro cavity. Dimensions are in mm.

## 5.6 Future Designs

Optimization of the achievable gradients, higher order mode properties and surface fields continues at various research centres around the world, including the University of Manchester. N. Juntong has developed a "New Low Surface Field" cavity (NLSF), complete with HOM coupler design, which has improved accelerating mode bandwidth as well as the crucial low surface fields [69].

## 5.7 Summary

In this chapter the designs for the ILC baseline accelerating cavities as well as the alternative high-gradient designs have been described. Namely, the TESLA, Reentrant and Ichiro cavities. The properties of the superconducting Niobium material have been introduced, linking the required performance to the particular cavity contours through the figures of merit used for the optimization. These designs give the specifications required for electromagnetic field simulations.

In the next chapter the Finite Difference Method is introduced - this is the technique used to simulate the fields present within the cavities, since no analytic form is available for such geometries.

# Chapter 6

# The Finite Difference Method

The Finite Difference Method is one of many numerical techniques developed in order to solve problems cast in partial differential equations. In this chapter the basic techniques used to approximate field derivatives will be introduced and then applied to Maxwell's Equations in order to calculate frequencies of waveguide modes and eigenmodes of a Pillbox Cavity in an axis-symmetric coordinate system. A major part of the results described in this thesis (see Chapter 7) were calculated using the code GdfidL which makes use of the Finite Difference Method to calculate electromagnetic fields in both the frequency and time domains. This chapter serves as a primer to the method as well as highlighting important areas such as boundary conditions which must be handled carefully.

In the finite difference method an approximate solution is achieved by representing the solution domain with a structured *mesh* of discrete points. The discretization of the governing equations produces a linear system of simultaneous equations which may be solved in order to generate the solution value at each point in the mesh. In contrast with the Finite Element Method the field or solution value is only available at each mesh point.

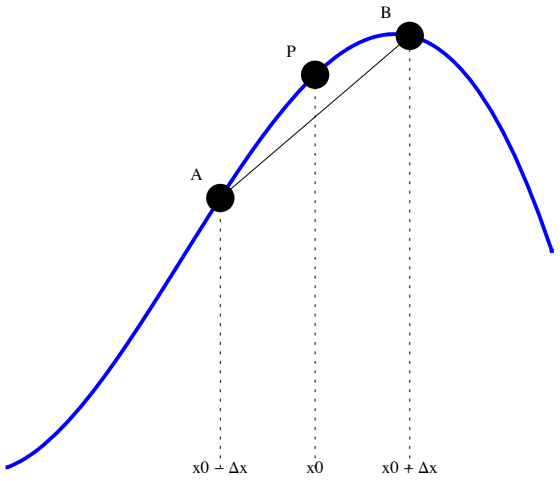


**Figure 6.1:** Estimated derivatives for the function $f(x)$ at point $P$.

## 6.1 Introduction to the Finite Difference Approximation

Originally developed in the 1920s by A. Thom [70] in order to solve nonlinear hydrodynamics problems the Finite Difference method has been enthusiastically embraced as a numerical technique since the arrival of programmable computing systems. The accuracy of a finite difference solution is related to the mesh spacing employed thus, as computing power has increased, scientists have become able to model finer detail to a greater degree of accuracy and in a shorter time. Over time new extensions have been proposed and newly developed codes have surpassed the performance of their predecessors but each example is generally based on the numerical approximation of first and second order derivatives as will be described in this section.

Consider a general, continuous, differentiable function $f(x)$, shown in Figure 6.1. Three points on the curve $A, B$ and $P$ are marked. We can simply approximate the derivative of $f$ at the point $P$ by calculating the gradient of the arc $AB$. This results in the central difference formula Equation 6.1:

$$f'(x_0) \simeq \frac{f(x_0 + \Delta x) - f(x_0 - \Delta x)}{2\Delta x}. \tag{6.1}$$

The second derivative of $f(x)$ can also be estimated at point $P$ as

$$\begin{aligned} f''(x) &\simeq \frac{f'(x_0 + \Delta x/2) - f'(x_0 - \Delta x/2)}{\Delta x} \\ &= \frac{1}{\Delta x}\left[\frac{f(x_0 + \Delta x) - f(x_0)}{\Delta x} - \frac{f(x_0) - f(x_0 - \Delta x)}{\Delta x}\right], \end{aligned} \tag{6.2}$$

or more compactly:

$$f''(x_0) \simeq \frac{f(x_0 + \Delta x) - 2f(x_0) + f(x_0 - \Delta x)}{(\Delta x)^2}. \tag{6.3}$$

The above are first order finite difference approximations to the derivatives of $f(x)$. Alternatively, a Taylor series expansion of $f$ can be used to obtain higher order approximations. Although a higher order approximation would improve accuracy for a given discretization this chapter will be restricted to first order for clarity. In contrast, the code GdfidL [71] makes use of a higher order scheme (see Chapter 6.5).

In computational problems the function $f$ can be determined in a given range if the boundary conditions are known. The computation proceeds from the boundary and calculates the solution at each neighbouring point according to the governing partial differential equation.

The method described above can be easily extended to two or more dimensions.

### 6.1.1 Solutions in two dimensions

Consider a new function $f(x,t)$ which has two independent variables. By decomposing the solution region of the $x-t$ plane into a series of equal sized square units, a mesh, the partial derivatives can be calculated a points separated by $\Delta x$ or $\Delta t$. Applying the central difference approximation, the derivatives at a point $P(x = x_0, t = t_0)$ are

$$f_x \simeq \frac{f(x_1,t) - f(x_{-1},t)}{2\Delta x} \tag{6.4a}$$

$$f_t \simeq \frac{f(x,t_1) - f(x,t_{-1})}{2\Delta t} \tag{6.4b}$$

$$f_{xx} \simeq \frac{f(x_1,t) - f(x_0,t_0) + f(x_{-1},t)}{(\Delta x)^2} \tag{6.4c}$$

$$f_{tt} \simeq \frac{f(x,t_1) - f(x_0,t_0) + f(x,t_{-1})}{(\Delta t)^2} \tag{6.4d}$$

From the above primitives the finite difference form of a differential equation, such as the wave equation, can be formed. From this "explicit form" the solution at a neighbouring point $Q$ can be derived from the value at point $P$ and the whole region can be solved beginning from the boundary conditions. Meshing involving square or rectangular cells will easily and accurately model simple geometries made themselves of rectangular sections. All finite difference meshing techniques will introduce errors when applied to complex geometries involving curved boundaries, the computational volume solved will either be too large or, more likely, too small with the boundary approximated as a "staircase". The simplest solution is to reduce the mesh spacing to more accurately map the curve of the boundary at the expense of a larger computational problem.

In the following sections the above method is illuminated by solving simple Electromagnetic problems closely related to major effort of this thesis. In Chapter 7 GdfidL has also solved Maxwell's equations to return fields and modal frequencies just in three dimensions rather than the simpler case of 2D.

## 6.2 Maxwell's Equations

The electromagnetic field in an evacuated cavity or waveguide bounded by perfectly conducting surfaces, on which there are no surface charges, is governed by Maxwell's Equations [34]:

$$\epsilon_0 \frac{\partial \mathbf{E}}{\partial t} = \boldsymbol{\nabla} \times \mathbf{H}, \tag{6.5a}$$

$$\boldsymbol{\nabla} \cdot \mathbf{E} = 0, \tag{6.5b}$$

$$\mu_o \frac{\partial \mathbf{H}}{\partial t} = -\boldsymbol{\nabla} \times \mathbf{E}, \tag{6.5c}$$

$$\boldsymbol{\nabla} \cdot \mathbf{H} = 0, \tag{6.5d}$$

where $\epsilon_0$ and $\mu_0$ are the permitivity and permeability of free space respectively. Taking the curl of Equation 6.5c gives

$$\mu_0 \frac{\partial}{\partial t} \boldsymbol{\nabla} \times \mathbf{H} = -\boldsymbol{\nabla} \times \boldsymbol{\nabla} \times \mathbf{E}, \tag{6.6}$$

and then using Equation 6.5a to replace the magnetic field gives

$$\mu_0\epsilon_0\frac{\partial^2\mathbf{E}}{\partial t^2} = -\boldsymbol{\nabla}\times\boldsymbol{\nabla}\times\mathbf{E}. \tag{6.7}$$

Imposing harmonic fields of the form $\mathbf{E} = \boldsymbol{\mathcal{E}}e^{i\omega t-\beta z}$ then Equation 6.7 becomes

$$\mu_0\epsilon_0\omega^2\boldsymbol{\mathcal{E}} = \boldsymbol{\nabla}\times\boldsymbol{\nabla}\times\boldsymbol{\mathcal{E}}. \tag{6.8}$$

Making use of the vector identity:

$$\boldsymbol{\nabla}\times\boldsymbol{\nabla}\times\boldsymbol{V} = \boldsymbol{\nabla}(\boldsymbol{\nabla}\cdot\boldsymbol{V}) - \nabla^2\boldsymbol{V}, \tag{6.9}$$

and dropping the divergence term as required by Equation 6.5b we now have the Helmholtz or Wave Equation

$$\nabla^2\boldsymbol{\mathcal{E}} + \mu_0\epsilon_0\omega^2\boldsymbol{\mathcal{E}} = 0. \tag{6.10}$$

The following sections will detail the discretization of this wave equation for two physical problems.

## 6.3 Rectangular Waveguide Modes

Here we consider a cross-section through an evacuated rectangular waveguide. The section forms the $x$-$y$ plane and it is perpendicular to the $z$-axis. In this case we are solving for a single field component, either $H_z$ for Transverse Electric (TE) modes or $E_z$ for Transverse Magnetic (TM) modes. We will refer to a single field quantity $\Phi$ in the following discussion, thus the governing equation becomes

$$\nabla^2\Phi + k^2\Phi = 0, \tag{6.11}$$

where the wavenumber $k$ is given by

$$k^2 = \mu_0\epsilon_0\omega^2 - \beta^2. \tag{6.12}$$

Equation 6.11 describes an eigenvalue problem in which $k$ and $\Phi$ are to be determined. Each cut-off wavelength $\lambda_c = 2\pi/k_c$ has a corresponding eigenmode solution $\Phi_c$ which represents the field configuration.

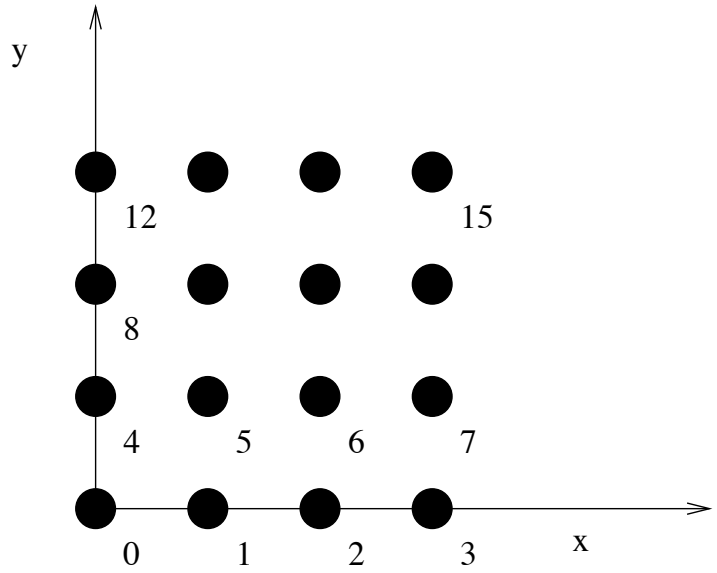


**Figure 6.2:** Square $4 \times 4$ mesh for a waveguide cross-section. The node numbering scheme is illustrated.

Solution of this eigenvalue problem with the finite difference method requires that we discretize the cross-section. Figure 6.2 illustrates the smallest mesh which will allow demonstration of the key features, a 4 node by 4 node square mesh.

The value of the field at each node $\Phi_i$ will be determined by solution of the eigenvalue problem for $\Phi$. Applying the central difference approximation described in Equation 6.3 to the cartesian expansion of Equation 6.11 gives

$$\begin{aligned} &\Phi(i+1,j) + \Phi(i-1,j) \\ &\qquad + \Phi(i,j+1) + \Phi(i,j-1) \\ &\qquad\qquad - \left(4 - h^2k^2\right)\Phi(i,j) = 0 \end{aligned} \tag{6.13}$$

where $\Delta x = \Delta y = h$ is the mesh spacing and $i$ and $j$ refer to the position of a particular node within the mesh. For example, the node in the lower left corner of Figure 6.2 which is at position $x = 0, y = 0$ has field value $\Phi_0 = \Phi(0,0)$. The node to its right $\Phi_1 = \Phi(1,0)$ and so on. The above Equation 6.13 applies for the interior nodes, boundary conditions must be specified separately.

### 6.3.1 Boundary Conditions

For TM modes we are solving for $E_z$, therefore, on the boundary nodes the field must be zero since the boundary is a perfect conductor.

$$\Phi_{\text{boundary}} = 0. \tag{6.14}$$

This is a Dirichlet boundary condition. Similarly, for TE modes in which we are solving for $H_z$ there is a Neumann boundary condition on $\Phi$:

$$\frac{\partial \Phi}{\partial n} = 0, \tag{6.15}$$

where $n$ corresponds to the normal derivative across the boundary. Consider Figure 6.3 in which the node $\Phi_2$ on the lower boundary is marked and surrounded by its neighbours $\Phi_L, \Phi_R, \Phi_U, \Phi_D$. Each node has a corresponding index form $\Phi(i,j)$ except for $\Phi_D$ which is a virtual node outside the problem domain. For this lower boundary the Neumann condition Equation 6.15 implies that $\Phi_D = \Phi_U$ so that the virtual node can be eliminated from Equation 6.13 to give

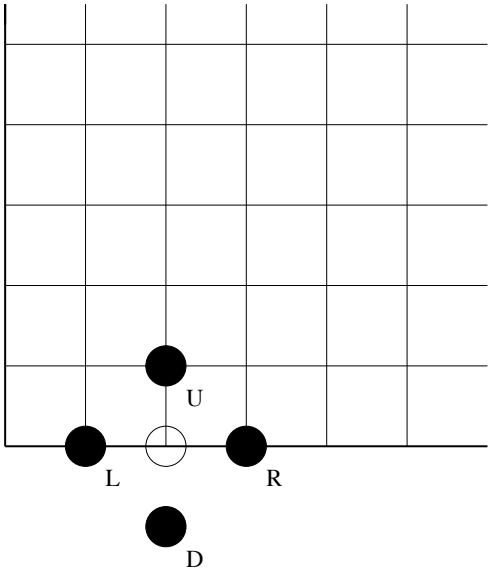


**Figure 6.3:** Lower mesh boundary.

$$\Phi_R + \Phi_L + 2\Phi_U - \left(4 - h^2k^2\right)\Phi_2 = 0. \tag{6.16}$$

The boundary equation for nodes on the left, right and upper boundaries can be similarly determined.

### 6.3.2 Eigenvalue problem

Applying Equations 6.13 and 6.16 or 6.14 to the mesh results in a system of $m$ simultaneous equations, where $m$ is the number of nodes. These $m$ equations are formed from the $m$ components in the solution vector $\Phi = (\Phi_0, \Phi_1, \Phi_2, \ldots, \Phi_m)$ and can be expressed as an eigenvalue problem

$$A\Phi = \lambda\Phi, \tag{6.17}$$

where $\lambda$ is the eigenvalue and $\Phi$ is the eigenvector for the $m \times m$ matrix $A$ to be solved. Clearly the governing equations defined above for a node $n$ specify the elements in row $n$ of the matrix $A$ *i.e.*

$$A_n^{\mathrm{T}} \cdot \Phi = \lambda\Phi_n \tag{6.18}$$

and from this and Equations 6.13, 6.16, 6.14 the $A$ matrix can be filled row by row. In the TM case the rows corresponding to boundary nodes are set to zero across the row. This implies that, for non-spurious eigenvalues, $\Phi_{\mathrm{boundary}} = 0$ as required by Equation 6.14. The leading diagonal in $A$ is set to 4 with up to four other elements in a particular row equal to unity according to Equation 6.13. For the case of a $4 \times 4$ mesh, as illustrated in Figure 6.2 the $16 \times 16$ element matrix $A$ is shown in Figure 6.4. Although many of the rows have been set to zero it is still possible to make out the sparse and banded nature of the matrix. This is a characteristic feature of finite difference and finite element discretizations.

Having populated the matrix $A$ it can then be passed to a standard eigensolver package in order to determine the eigenvalues. There are a two major types of eigensovler in wide spread use, direct solvers and iterative solvers. Direct solvers will return all possible eigenvalues for the system i.e. for the described $16 \times 16$ matrix there will be 16 eigenvalues returned. However, for a given limited mesh size the accuracy of the numerical solutions will drop after the most dominant modes. Further, particularly for the TM case where the Dirichlet boundary condition underconstrains the eigenvalue problem there will be spurious solutions which must be filtered out.

$$\begin{pmatrix}
0 & 0 & 0 & 0 & 0 & 0 & 0 & 0 & 0 & 0 & 0 & 0 & 0 & 0 & 0 & 0 \\
0 & 0 & 0 & 0 & 0 & 0 & 0 & 0 & 0 & 0 & 0 & 0 & 0 & 0 & 0 & 0 \\
0 & 0 & 0 & 0 & 0 & 0 & 0 & 0 & 0 & 0 & 0 & 0 & 0 & 0 & 0 & 0 \\
0 & 0 & 0 & 0 & 0 & 0 & 0 & 0 & 0 & 0 & 0 & 0 & 0 & 0 & 0 & 0 \\
0 & 0 & 0 & 0 & 0 & 0 & 0 & 0 & 0 & 0 & 0 & 0 & 0 & 0 & 0 & 0 \\
0 & -1 & 0 & 0 & -1 & 4 & -1 & 0 & 0 & -1 & 0 & 0 & 0 & 0 & 0 & 0 \\
0 & 0 & -1 & 0 & 0 & -1 & 4 & -1 & 0 & 0 & -1 & 0 & 0 & 0 & 0 & 0 \\
0 & 0 & 0 & 0 & 0 & 0 & 0 & 0 & 0 & 0 & 0 & 0 & 0 & 0 & 0 & 0 \\
0 & 0 & 0 & 0 & 0 & 0 & 0 & 0 & 0 & 0 & 0 & 0 & 0 & 0 & 0 & 0 \\
0 & 0 & 0 & 0 & 0 & -1 & 0 & 0 & -1 & 4 & -1 & 0 & 0 & -1 & 0 & 0 \\
0 & 0 & 0 & 0 & 0 & 0 & -1 & 0 & 0 & -1 & 4 & -1 & 0 & 0 & -1 & 0 \\
0 & 0 & 0 & 0 & 0 & 0 & 0 & 0 & 0 & 0 & 0 & 0 & 0 & 0 & 0 & 0 \\
0 & 0 & 0 & 0 & 0 & 0 & 0 & 0 & 0 & 0 & 0 & 0 & 0 & 0 & 0 & 0 \\
0 & 0 & 0 & 0 & 0 & 0 & 0 & 0 & 0 & 0 & 0 & 0 & 0 & 0 & 0 & 0 \\
0 & 0 & 0 & 0 & 0 & 0 & 0 & 0 & 0 & 0 & 0 & 0 & 0 & 0 & 0 & 0 \\
0 & 0 & 0 & 0 & 0 & 0 & 0 & 0 & 0 & 0 & 0 & 0 & 0 & 0 & 0 & 0
\end{pmatrix}$$

**Figure 6.4:** Matrix $A$ showing the sparse banded system resulting from finite difference discretization of a square mesh.

Figure 6.5 displays the longer wavelength eigenmodes which are calculated by a direct solver method for a $25 \times 25$ node discretization of a 1.4 cm square waveguide. The TM modes are offset from the TE modes due to the presence of modes with zero eigenvalues. The cutoff wavelength for a mode, $\mathrm{TM}_{lm}$ or $\mathrm{TE}_{lm}$, in a rectangular waveguide, sized $a$ by $b$, can be analytically calculated according to the following expression:

$$\frac{1}{\lambda_c^2} = \left(\frac{l}{2a}\right)^2 + \left(\frac{m}{2b}\right)^2, \tag{6.19}$$

where $l$ and $m$ are integers $0, 1, 2, 3 \ldots$. Table 6.1 contrasts the finite difference calculated cutoff wavelengths for the first few longest wavelength TE and TM modes with the analytical solutions from Equation 6.19. The finite difference solutions are

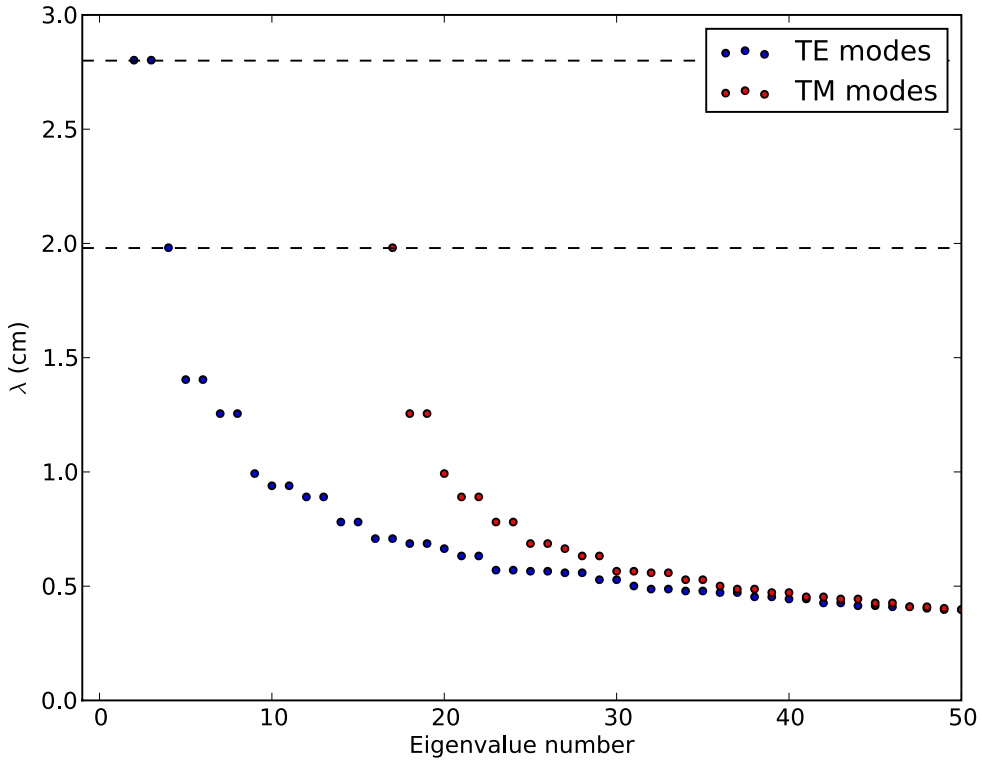


**Figure 6.5:** TE (blue) and TM (red) mode wavelengths in a 14 mm square waveguide section. The offset between the two spectra is related to the number of spurious eigenvalue solutions in the underconstrained TM problem.

in good agreement for this relatively fine mesh.

Figure 6.6 shows the field distribution corresponding to the $TM_{11}$ mode which also displays the correct properties, in particular that the $E_z$ field is zero on the metal boundaries.

## 6.4 Pillbox Cavity Monopole Modes

We now consider the simple example of a closed axis-symmetric cylindrical pillbox cavity. This can be easily treated in cylindrical polar coordinates with the finite difference method in order to find the most dominant eigenmode. In a pillbox cavity this takes the form of an azimuthally symmetric "monopole" mode. In this

| Mode | Analytical(cm) | FD(cm) |
|---|---|---|
| $TE_{01}$ | 2.800 | 2.802 |
| $TE_{10}$ | 2.800 | 2.802 |
| $TE_{11}$ | 1.9799 | 1.9813 |
| $TE_{21}$ | a | b |

| Mode | Analytical(cm) | FD(cm) |
|---|---|---|
| $TM_{11}$ | 1.9799 | 1.9813 |
| $TM_{21}$ | 1.9799 | 1.9813 |

**Table 6.1:** TE and TM eigenmodes from finite difference approximation and with the analytical solutions for a 1.4cm square waveguide discretized with a $25 \times 25$ node mesh.

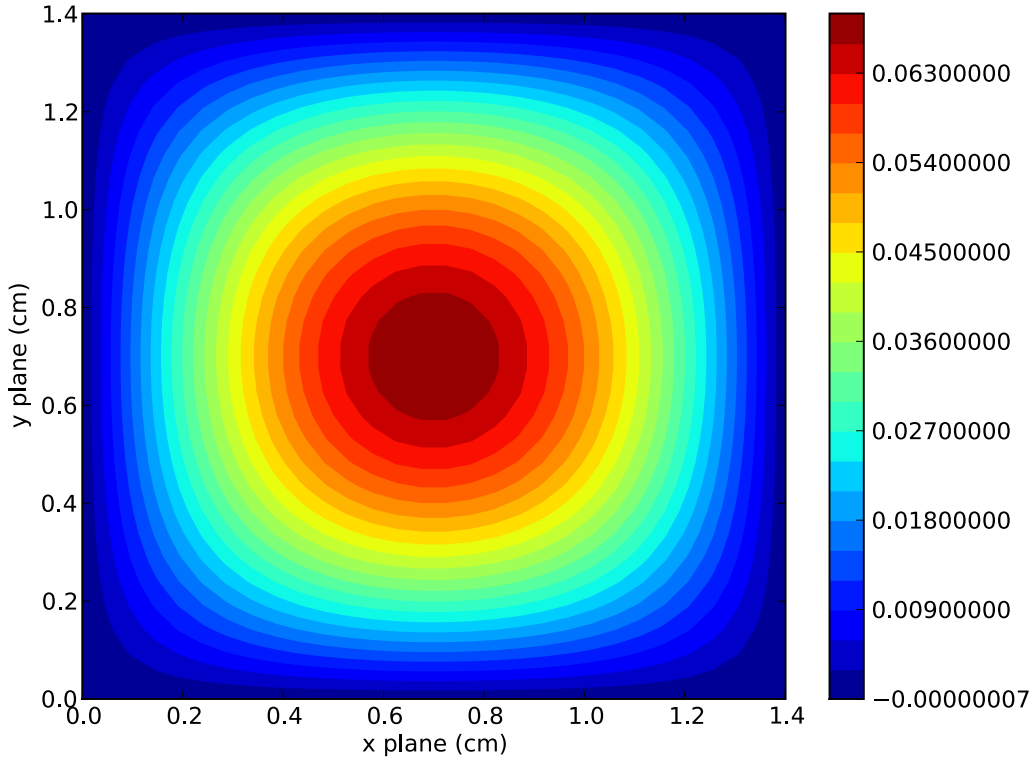


**Figure 6.6:** Cross-section in $x - y$ plane of $E_z$ field distribution for $TE_{11}$ mode in a 1.4 cm square waveguide section, calculated by finite difference method.

section we will illustrate the formation of the finite difference problem from the discretization of the cylindrical form of Equation 6.10 and in Section 6.4.4 present

the calculated frequencies for the lower monopole modes and vector field plots.

Beginning from Equation 6.10 we are first required to expand the vector form of the Laplacian operator on **E**.

$$\begin{aligned}\nabla^2\mathbf{E} &= \begin{pmatrix} \nabla^2 E_r - \dfrac{E_r}{r^2} \\ 0 \\ \nabla^2 E_z \end{pmatrix} \\ &= \begin{pmatrix} \dfrac{1}{r}\dfrac{\partial}{\partial r}\left(r\dfrac{\partial E_r}{\partial r}\right) + \dfrac{\partial^2 E_r}{\partial z^2} - \dfrac{E_r}{r^2} \\ 0 \\ \dfrac{1}{r}\dfrac{\partial}{\partial r}\left(r\dfrac{\partial E_z}{\partial r}\right) + \dfrac{\partial^2 E_z}{\partial z^2} \end{pmatrix} \\ &= \begin{pmatrix} \dfrac{\partial^2 E_r}{\partial r^2} + \dfrac{1}{r}\dfrac{\partial E_r}{\partial r} + \dfrac{\partial^2 E_r}{\partial z^2} - \dfrac{E_r}{r^2} \\ 0 \\ \dfrac{\partial^2 E_z}{\partial r^2} + \dfrac{1}{r}\dfrac{\partial E_z}{\partial r} + \dfrac{\partial^2 E_z}{\partial z^2} \end{pmatrix} = \begin{pmatrix} L_r \\ L_\phi \\ L_z \end{pmatrix}. \end{aligned} \tag{6.20}$$

In Equation 6.20 the azimuthal dependence has been explicitly set to zero in order to select monopole modes and the vector $\mathbf{L} = (L_r, L_\phi, L_z)$ simply introduces a shorthand. Note that there are no mixed derivatives and that the $r$ and $z$ components are not coupled. Higher Order Modes can be calculated by reinstating these terms with the correct order and functional form. In the case of dipole modes the variation would be described by $\dfrac{\partial}{\partial \phi} \sim e^{i\phi}$. It is now necessary, as before, to discretize the partial differential equations for each field component.

### 6.4.1 Discretization

Tackling the $z$-component equations first we can discretize term by term, employing the same central difference approximations described in Section 6.1. Applying a mesh similar to that displayed in Figure 6.2 except now orientated in the $z-r$ plane allows transformation from

$$L_z = \frac{\partial^2 E_z}{\partial r^2} + \frac{1}{r}\frac{\partial E_z}{\partial r} + \frac{\partial^2 E_z}{\partial z^2},$$

to the discretized form

$$L_z = \frac{E_z(i+1,j) - 2E_z(i,j) + E_z(i-1,j)}{(\Delta z)^2} + \frac{1}{r}\frac{E_z(i,j+1) - E_z(i,j-1)}{2\Delta r} + \frac{E_z(i,j+1) - 2E_z(i,j) + E_z(i,j-1)}{(\Delta r)^2}, \quad (6.21)$$

in which $\Delta r$ and $\Delta z$ are the mesh spacings in the $r$ and $z$ planes respectively. Rearranging the above form by collecting the terms involving particular mesh points gives:

$$L_z = E_z(i,j)\left[\frac{-2}{(\Delta z)^2} + \frac{-2}{(\Delta r)^2}\right] + E_z(i,j+1)\left[\frac{1}{(\Delta r)^2} + \frac{1}{r2\Delta r}\right] + E_z(i,j-1)\left[\frac{1}{(\Delta r)^2} - \frac{1}{r2\Delta r}\right] + \frac{E_z(i+1,j)}{(\Delta z)^2} + \frac{E_z(i-1,j)}{(\Delta z)^2} \quad (6.22)$$

and again implies that computation at a particular mesh point is dependent on the field at each of the neighbouring points. We can now write down the discretized form of the wave equation for the $z$-component of the electric field:

$$E_z(i,j+1)\left[1 + \frac{\Delta h}{2r}\right] + E_z(i,j-1)\left[1 - \frac{\Delta h}{2r}\right] + E_z(i+1,j) + E_z(i-1,j) + E_z(i,j)\left[k^2(\Delta h)^2 - 4\right] = 0, \quad (6.23)$$

where $\Delta h = \Delta z = \Delta r$ and the equation has been simplified by multiplying through by $(\Delta h)^2$. Computationally the value of $r$ will be taken at the mesh point $(i,j)$ and given by $r = \Delta h \cdot j$. Applying the same procedure to the $r$-component equation yields:

$$E_r(i,j+1)\left[1 + \frac{\Delta h}{2r}\right] + E_r(i,j-1)\left[1 - \frac{\Delta h}{2r}\right] + E_r(i+1,j) + E_r(i-1,j) + E_r(i,j)\left[k^2(\Delta h)^2 - \frac{(\Delta h)^2}{r^2} - 4\right] = 0. \quad (6.24)$$

### 6.4.2 Boundary Conditions

There must not be any parallel component of electric field at a perfectly conducting boundary, from Gauss's Law. We must therefore set $E_z = 0$ along the upper wall of the cavity and $E_r = 0$ along the left and right boundaries. These conditions will be easily implemented by setting the corresponding rows in the problem matrix to zero, as previously described. Of course, the orthogonal field component obeys a Neumann condition as described in Section 6.3.1. Taking the left hand wall of the cavity where the derivative of the $z$-component of electric field must be continuous.

Just as in the previous section a "computational molecule" is employed to setup the equation which describes the field at mesh points on the left wall (see Figure 6.3). As before a phantom node, $\Psi_L$, outside the computational volume has been used, the field at this node must equal the field at the inner node $\Psi_R$. The following equation applies for this node,

$$E_{zU}\left[1+\frac{\Delta h}{2r}\right]+E_{zD}\left[1-\frac{\Delta h}{2r}\right]+2E_{zR}+E_{z\text{Wall}}\left[k^2\left(\Delta h\right)^2-4\right]. \tag{6.25}$$

Thus far the lower boundary has not been addressed. Since the problem is axis-symmetric we choose to solve in the upper half of the $z-r$ plane with the lower boundary functioning as the axis of symmetry. The lower boundary must therefore be considered "open" and Neumann conditions apply. Close examination of Equations 6.23 and 6.24 suggests a further issue since there are $\frac{1}{r}$ terms which will result in a singularity along the lower boundary. The issue is neatly side-stepped by enforcing the partial derivatives with $r$ to be zero, since $r = 0$ is a turning point for both $E_r$ and $E_z$, and removing those terms from the boundary equations. The $r$-component is fully constrained once a knowledge of the physical system is applied. The fundamental monopole mode of a cavity such as used in RF accelerating cavities provides no transverse kick to particles *i.e.* there is zero $E_r$ on axis. We are finally left with just the second order derivatives from the $r$-component in Equation 6.20.

### 6.4.3 Eigenvalue problem revisted

Equations 6.23 and 6.24 together with the boundary conditions described in Section 6.4.2 are employed to setup the $2 \times m$ simultaneous equations which describe the field on a mesh of $m$ nodes ($m$ equations for each field component). This can, again, be expressed as an eigenvalue problem.

As described in Section 6.3.2 there is a problem matrix $A$ in which row $n$ is formed from the governing equations corresponding to node $n$ in the mesh. Since there are two field components there are in fact two rows in $A$ for each mesh point, one for each field component. The problem is simplified somewhat by the absence of $E_r$ terms in the equations governing $E_z$ at a particular node and vice-versa. This implies that a given row will be necessarily half-filled with zeroes. Presenting the resulting matrix is somewhat difficult in a compact form since for a $4 \times 4$ node mesh matrix $A$ is now sized $32 \times 32$. It is shown in two parts below. The matrix in Figure 6.7 shows the upper left quadrant and represents the matrix elements which govern the $z$ components of electric field. Figure 6.8 shows the matrix lower right quadrant and represents the corresponding matrix elements governing $E_r$.

### 6.4.4 Monopole mode

Figure 6.9 displays the computed electric field, as a vector, across the cavity. The radius and length of the cavity are 1.15 cm. The eigenmode frequencies for TM modes in a pillbox cavity can be calculated using the analytic formula in Equation 6.26 [72].

$$f_{mnp} = \frac{c}{2\pi\sqrt{\mu_r \epsilon_r}} \sqrt{\left(\frac{J_{mn}}{R}\right)^2 + \left(\frac{p\pi}{L}\right)^2} \tag{6.26}$$

where $J_{mn}$ is the $\mathrm{n}^{\mathrm{th}}$ root of the $\mathrm{m}^{\mathrm{th}}$ Bessel function. $R$ and $L$ are the radius and length of the cavity. For the $\mathrm{TM}_{010}$ mode, the fundamental mode of the cavity has a frequency of 9.978 GHz.

Figure 6.10 shows the frequency determined by the eigensolver for successively finer meshes. Using the 'direct' eigensolver employed by the toy code detailed here it is not possible to use a mesh more detailed than $45 \times 45 = 2025$ cells. With 2025

$$\begin{pmatrix}
2 & -2 & 0 & 0 & 0 & 0 & 0 & 0 & 0 & 0 & 0 & 0 & 0 & 0 & 0 & 0 & \cdots \\
-1 & 4 & -1 & 0 & 0 & -2 & 0 & 0 & 0 & 0 & 0 & 0 & 0 & 0 & 0 & 0 & \cdots \\
0 & -1 & 4 & -1 & 0 & 0 & -2 & 0 & 0 & 0 & 0 & 0 & 0 & 0 & 0 & 0 & \cdots \\
0 & 0 & -2 & 2 & 0 & 0 & 0 & 0 & 0 & 0 & 0 & 0 & 0 & 0 & 0 & 0 & \cdots \\
0 & 0 & 0 & 0 & 4 & -2 & 0 & 0 & -1 & 0 & 0 & 0 & 0 & 0 & 0 & 0 & \cdots \\
0 & 0 & 0 & 0 & -1 & 4 & -1 & 0 & 0 & -1 & 0 & 0 & 0 & 0 & 0 & 0 & \cdots \\
0 & 0 & 0 & 0 & 0 & -1 & 4 & -1 & 0 & 0 & -1 & 0 & 0 & 0 & 0 & 0 & \cdots \\
0 & 0 & 0 & 0 & 0 & 0 & -2 & 4 & 0 & 0 & 0 & -1 & 0 & 0 & 0 & 0 & \cdots \\
0 & 0 & 0 & 0 & 0 & 0 & 0 & 0 & 4 & -2 & 0 & 0 & -1 & 0 & 0 & 0 & \cdots \\
0 & 0 & 0 & 0 & 0 & 0 & 0 & 0 & -1 & 4 & -1 & 0 & 0 & -1 & 0 & 0 & \cdots \\
0 & 0 & 0 & 0 & 0 & 0 & 0 & 0 & 0 & -1 & 4 & -1 & 0 & 0 & -1 & 0 & \cdots \\
0 & 0 & 0 & 0 & 0 & 0 & 0 & 0 & 0 & 0 & -2 & 4 & 0 & 0 & 0 & -1 & \cdots \\
0 & 0 & 0 & 0 & 0 & 0 & 0 & 0 & 0 & 0 & 0 & 0 & 0 & 0 & 0 & 0 & \cdots \\
0 & 0 & 0 & 0 & 0 & 0 & 0 & 0 & 0 & 0 & 0 & 0 & 0 & 0 & 0 & 0 & \cdots \\
0 & 0 & 0 & 0 & 0 & 0 & 0 & 0 & 0 & 0 & 0 & 0 & 0 & 0 & 0 & 0 & \cdots \\
0 & 0 & 0 & 0 & 0 & 0 & 0 & 0 & 0 & 0 & 0 & 0 & 0 & 0 & 0 & 0 & \cdots \\
\vdots & \vdots & \vdots & \vdots & \vdots & \vdots & \vdots & \vdots & \vdots & \vdots & \vdots & \vdots & \vdots & \vdots & \vdots & \vdots & \ddots
\end{pmatrix}$$

**Figure 6.7:** Upper left quadrant of matrix describing the eigenvalue problem for finite difference solution of pillbox cavity.

cells the frequency calculated is 9.9735 GHz.

## 6.5 Comment

As with all numerical methods the Finite Difference method will only produce an approximation to the system under study. In the simplest terms, a high accuracy can be achieved with very fine meshes i.e. a very large problem size. Unfortunately computational demands scale with $N^3$ and in practice there is a limit the problem size which can be solved on a given machine. Further, care must be taken to ensure

$$\begin{pmatrix}
\ddots & \vdots & \vdots & \vdots & \vdots & \vdots & \vdots & \vdots & \vdots & \vdots & \vdots & \vdots & \vdots & \vdots & \vdots & \vdots & \vdots \\
\cdots & 0 & 0 & 0 & 0 & 0 & 0 & 0 & 0 & 0 & 0 & 0 & 0 & 0 & 0 & 0 & 0 \\
\cdots & -1 & 2 & -1 & 0 & 0 & 0 & 0 & 0 & 0 & 0 & 0 & 0 & 0 & 0 & 0 & 0 \\
\cdots & 0 & -1 & 2 & -1 & 0 & 0 & 0 & 0 & 0 & 0 & 0 & 0 & 0 & 0 & 0 & 0 \\
\cdots & 0 & 0 & 0 & 0 & 0 & 0 & 0 & 0 & 0 & 0 & 0 & 0 & 0 & 0 & 0 & 0 \\
\cdots & 0 & 0 & 0 & 0 & 0 & 0 & 0 & 0 & 0 & 0 & 0 & 0 & 0 & 0 & 0 & 0 \\
\cdots & 0 & 0 & 0 & 0 & -1 & 5 & -1 & 0 & 0 & -1 & 0 & 0 & 0 & 0 & 0 & 0 \\
\cdots & 0 & 0 & 0 & 0 & 0 & -1 & 5 & -1 & 0 & 0 & -1 & 0 & 0 & 0 & 0 & 0 \\
\cdots & 0 & 0 & 0 & 0 & 0 & 0 & 0 & 0 & 0 & 0 & 0 & 0 & 0 & 0 & 0 & 0 \\
\cdots & 0 & 0 & 0 & 0 & 0 & 0 & 0 & 0 & 0 & 0 & 0 & 0 & 0 & 0 & 0 & 0 \\
\cdots & 0 & 0 & 0 & 0 & 0 & 0 & 0 & 0 & -1 & 4 & -1 & 0 & 0 & -1 & 0 & 0 \\
\cdots & 0 & 0 & 0 & 0 & 0 & 0 & 0 & 0 & 0 & -1 & 4 & -1 & 0 & 0 & -1 & 0 \\
\cdots & 0 & 0 & 0 & 0 & 0 & 0 & 0 & 0 & 0 & 0 & 0 & 0 & 0 & 0 & 0 & 0 \\
\cdots & 0 & 0 & 0 & 0 & 0 & 0 & 0 & 0 & 0 & 0 & 0 & 0 & 0 & 0 & 0 & 0 \\
\cdots & 0 & 0 & 0 & 0 & 0 & 0 & 0 & 0 & 0 & -2 & 0 & 0 & -1 & 4 & -1 & 0 \\
\cdots & 0 & 0 & 0 & 0 & 0 & 0 & 0 & 0 & 0 & 0 & -2 & 0 & 0 & -1 & 4 & -1 \\
\cdots & 0 & 0 & 0 & 0 & 0 & 0 & 0 & 0 & 0 & 0 & 0 & 0 & 0 & 0 & 0 & 0
\end{pmatrix}$$

**Figure 6.8:** Lower right quadrant of matrix describing the eigenvalue problem for finite difference solution of pillbox cavity.

that the particular algorithm chosen to attack the problem is convergent in the required regime. Numerical errors can easily be introduced by a naïve choice of algorithm, particularly in iterative time domain problems.

GdfidL employs multiple techniques, published and proprietary, to improve accuracy and reduce computation time. This includes such things as "generalised diagonal fillings" where many types of prism can be used in multiple orientations in order to better approximate the boundary of the problem geometry [73] and more exotic 'tricks' such as computing wake potentials in a moving frame in which the problem domain (cavity) has been Lorentz contracted - thus reducing the computa-

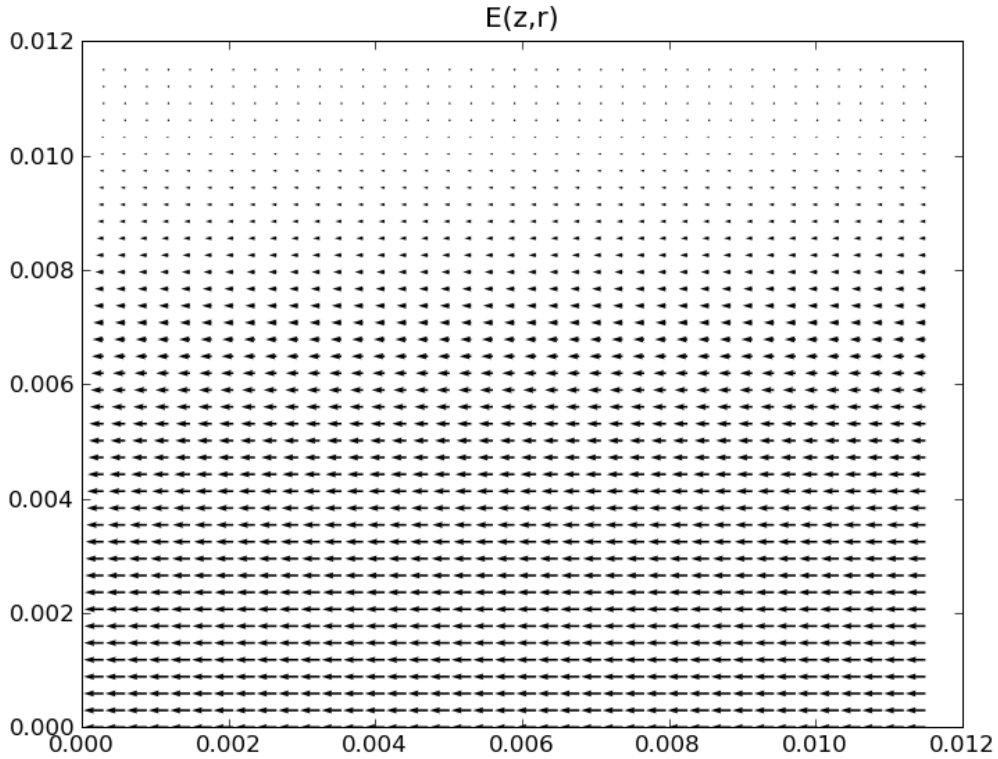


**Figure 6.9:** Electric field for $TM_{010}$ mode in pillbox cavity. $z$ and $r$ components are on the horizontal and vertical axes, respectively.

tional load [74].

In the next chapter the results of detailed eigenmode calculations, using GdfidL, for the Reentrant and Ichiro accelerating cavities are presented. The techniques and care with boundary conditions discussed above for the simple test cases apply equally to the 3D simulations undertaken with the more sophisticated code for the next chapter.

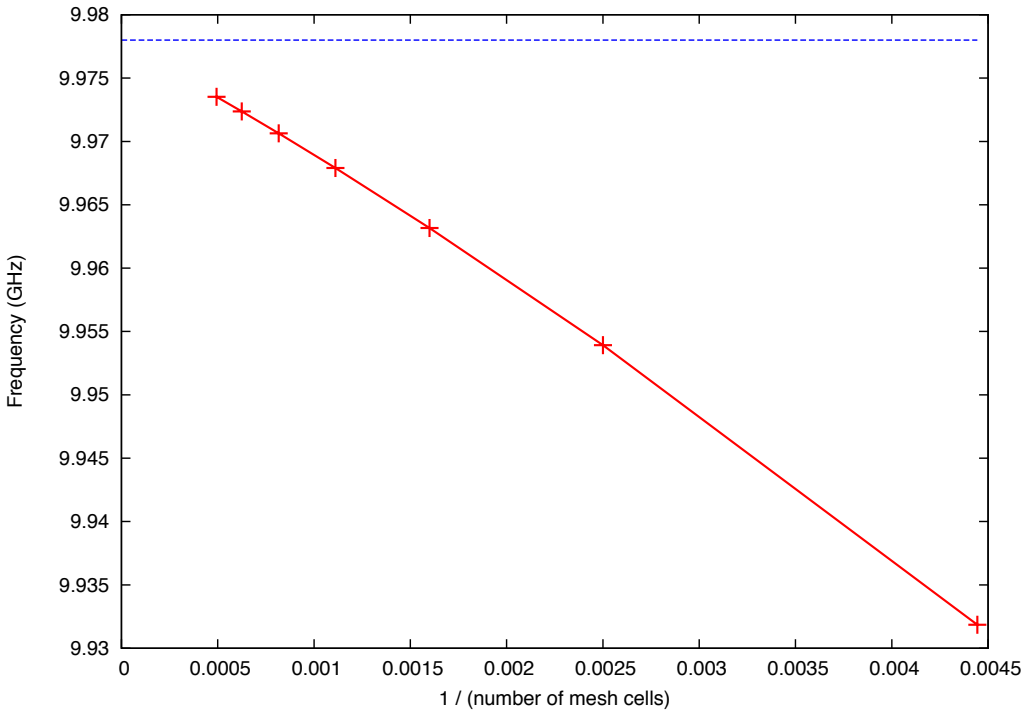


**Figure 6.10:** Convergence plot for the $TM_{010}$ mode frequency. The analytic result, 9.978 GHz, is show in blue. The horizontal axis is the reciprocal of the total number of mesh cells used.

# Chapter 7

# Cavity Simulation Results

Finite difference simulations of the electromagnetic fields in the Reentrant and Ichiro cavities were performed using the code GdfidL. Section 7.1 presents simulations of single cells, which give the dipole band structure while Section 7.2 details simulations of the 9 cell cavities for each of the cavity shapes under test. The discrete dipole modes from the 9 cell cavities are then employed in order to calculate the long range wakefield over the ILC bunch train, see Section 7.4. The eigenmode frequencies, kickfactors and wakefields calculated here are required as input to the beam dynamics study detailed in the next chapter in order to incorporate the long range wakefields due to the new cavity types.

All figures presented in this chapter were prepared by myself, unless labelled otherwise.

## 7.1 Single Cell Results

The resonant modes of definite frequency within a cavity structure are arranged in "bands", where each mode has a characteristic phase also. If we consider an infinite string of identical cells joined together, this mode frequency within a band is a continuous function of the phase advance in the field across the single cell. The field obeys periodicity criterion known as the Floquet condition:

$$E_z(z+L) = E_z(z)e^{-i\phi} \tag{7.1}$$

where $L$ is the cell length and $\phi$ is the phase advance in the electric field $E$. By performing a simulation in which the phase is prescribed as one of the boundary conditions this continuous function - the dispersion curve - can be calculated for each mode. Sets of modes are confined to pass-bands. The non-propagating regions between pass-bands are known as stop-bands. Figure 7.1 shows the dispersion curve for the fundamental mode of the Cornell University Reentrant cell. The lightline is also plotted - notice that it intersects with the dispersion curve at 180° and 1.3 GHz - this is by design.

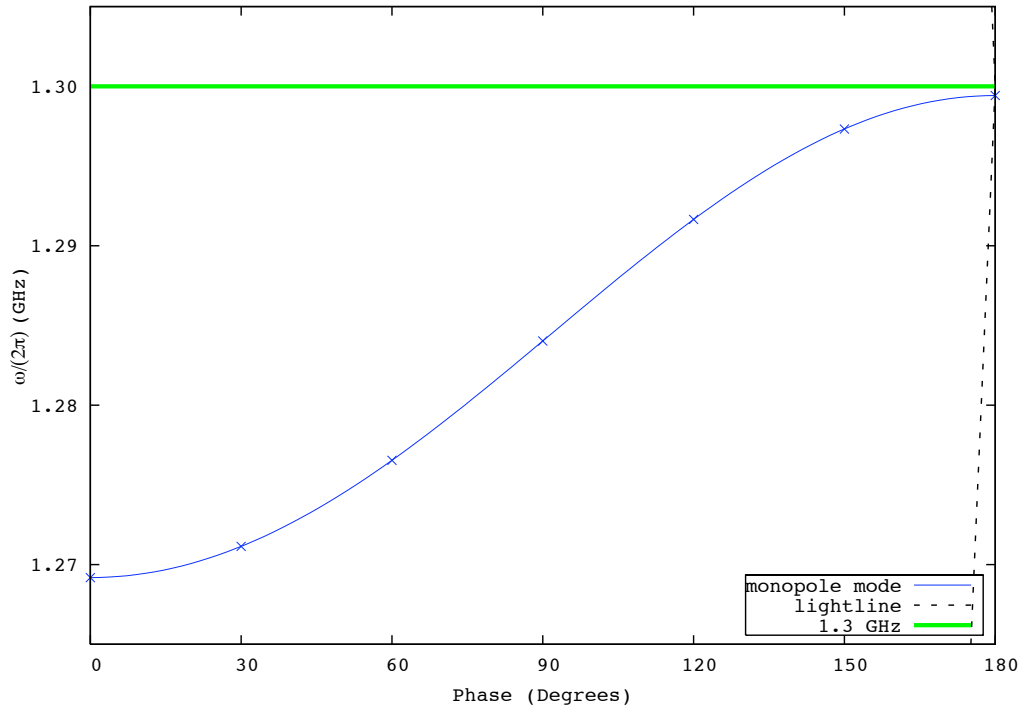


**Figure 7.1:** Dispersion curve for Monopole mode in single cell 35mm reentrant cell, with lightline.

Since an electron bunch is ultra-relativistic, crossings with the lightline indicate that the the mode is synchronous with the passage of the bunch. A mode operating at this point will maximally transfer its energy to the beam. For the fundamental mode, which does the accelerating, this is of course desired. There will be higher

order modes which are also synchronous with the beam, in this case the possible deflection is most severe and care must be taken to damp down the effect.

Simulations of the deflecting dipole modes within single cell cavities were performed for the Ichiro design cells and for the Reentrant design with cavity iris radius of 35 mm and 30 mm. Dispersion curves for the dipole bands in these designs, up to 4 GHz are shown in Figure 7.2. Although the designs are quite similar and all are optimized to accelerate a beam at 1.3 GHz in the $\pi$-mode the slight variations cause the higher order modes to be repartioned and the detailed effects on the passage of an electron bunch must be investigated. We note two features, firstly, that the two 30mm iris designs are quite closely matched. Despite the differences in the geometries of the ichiro and reentrant 30 mm designs, with the same iris dimension we expect the same coupling between neighbouring cells and this drives the bandwidth in the dispersion curves.

Secondly, that the fifth dipole band in each design shows a very low gradient dispersion curve.

The gradient $\frac{df}{f\phi}$ is related to the group velocity, $v_g$, via Equations 7.2 and 7.3.

$$\phi = 2\pi\frac{L}{\lambda} = Lk, \tag{7.2}$$

where $\phi$ is the phase advance per cell of length $L$, $\lambda$ is the wavelength and $k$ the angular wavenumber. The group velocity is given by:

$$v_g = \frac{\partial\omega}{\partial k} = \frac{\partial\omega}{\partial\phi}\frac{\partial\phi}{\partial k} = \frac{\partial\omega}{\partial\phi}L \tag{7.3}$$

and thus a very low gradient in the dispersion curve implies a group velocity close to zero and the possibility of trapped modes in this band.

## 7.2 Higher Order Mode Simulations

### 7.2.1 Reentrant cavity

The Reentrant cavity geometry detailed in Section 5.4 and Figure 5.2 was modelled in GdfidL, choosing a mesh cell spacing of, on average, 1 mm. This resulted in a

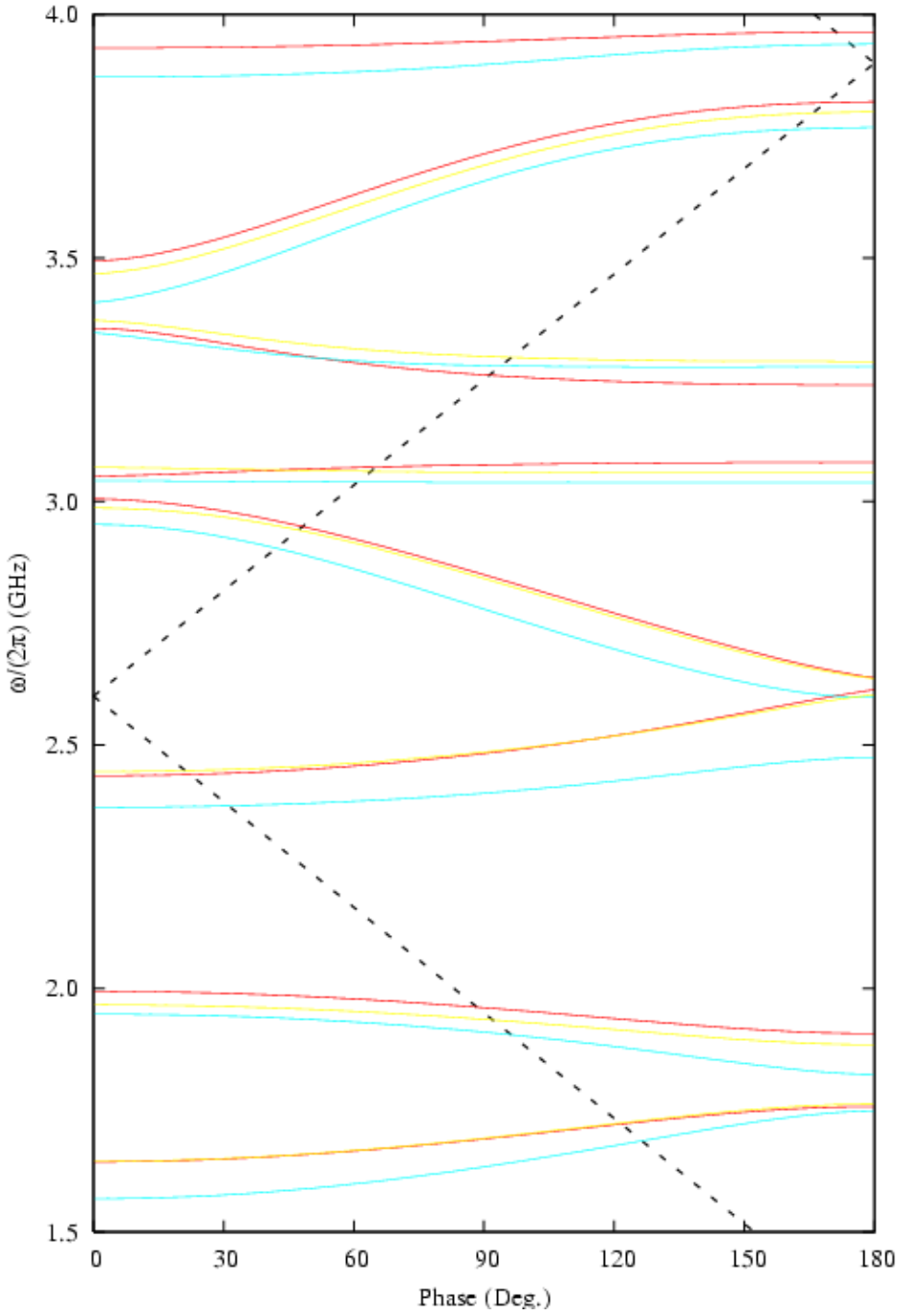


**Figure 7.2:** Dispersion curve for dipole modes within single cell Reentrant 35mm (blue), Reentrant 30mm (red) and Ichiro 30mm (yellow) designs.

total mesh size in excess of 18 million cells. In order to process this very large mesh effectively a parallel version of GdfidL was employed in which the computation can be distributed across multiple machines. In this case we made use of 24 computing nodes.

Eigenmodes were computed in the range 1.5 GHz to 4 GHz. The electromagnetic fields were then used to calculate the $R/Q$s and kickfactors according to Equations 4.30 and 4.28. By making use of the Floquet condition on the longitudinal component of electric field the phase advance for each mode was calculated. This data is usefully presented with the frequencies in the form of a Brillouin or dispersion diagram. This is shown in Figure 7.10. The points correspond to the discrete cavity modes while the curves correspond to a single cell with infinitely periodic boundary conditions. The discrete modes for each band are expected to lie on the curves although it is clear that 9 cells does not well approximate the infinite case. In particular, modes whose fields are localized towards the end cells of the cavity are expected to be somewhat shifted from the curves. Likewise, notable exceptions observed in Figure 7.10 are the beam pipe modes (see section 7.3). Modes located in regions where the gradient of the dispersion curve is close to zero have very low group velocity and may exhibit trapping. Such modes may not be adequately damped by higher order mode couplers located outside the cavity and thus are a concern for beam dynamics. Trapped modes are discussed in detail by Schuhmann & Weiland [75] and investigations into a poorly damped mode observed at the TESLA Test Facility are detailed by Baboi [13]. The $R/Q$s are displayed in Figure 7.3, in which a comparison has been made between the modes of this structure and those calculated for an older design (see [1, 2]). We note a mode at 3.936 GHz which has a significant $R/Q \sim 2$ Ohms/cm$^2$ in contrast to the usual behaviour in which modes beyond the third band have $R/Q$s orders of magnitude less.

### 7.2.2 Ichiro Cavity

The Ichiro cavity geometry discussed in Section 5.5 was also modelled using GdfidL. In this case the mesh spacing was 0.8 mm, resulting in a mesh of more than 16 million cells for half of the longitudinally symmetric structure. The higher density mesh here was achieved by halving the structure volume to be meshed. The complete set of modes is recreated by performing two simulations, the first with a perfect electric boundary condition in the reflection plane and the second with a perfect

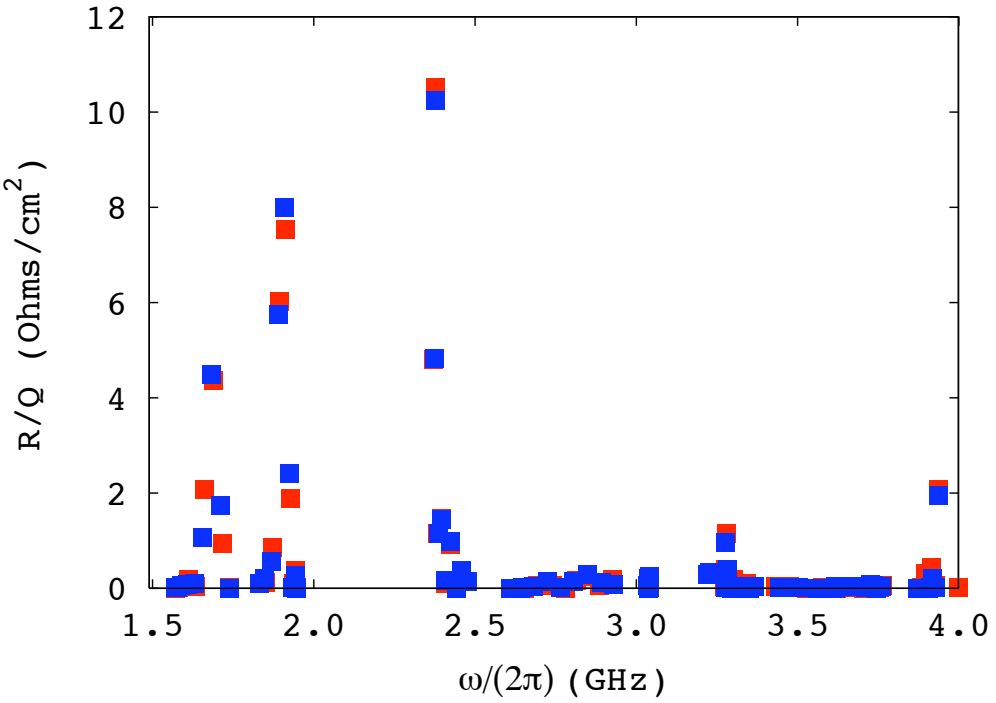


**Figure 7.3:** Cavity dipole $R/Q$s for the two Reentrant cavity designs. Red points show modes from the original 35mm design. Blue are modes from the redesigned, expanded beam pipe geometry. [1, 2]

magnetic boundary. The simulated geometry is displayed in Figure 7.4 with the lowest frequency dipole mode electric field superimposed. Dipole modes in the range

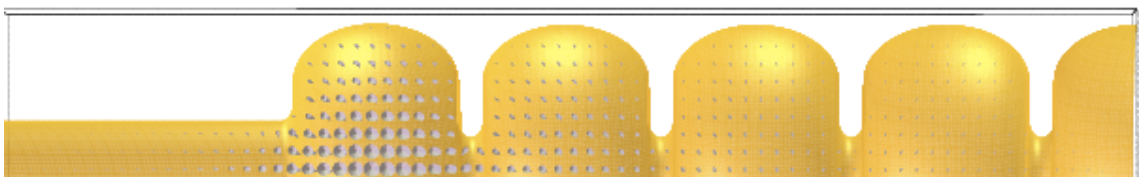

**Figure 7.4:** Ichiro cavity geometry modelled in GdfidL and showing the first dipole mode electric field which is strongly localized to the end cells.

1.5 GHz to 4 GHz were simulated. Their phases and frequencies are displayed in the dispersion curves of Figure 7.11. In this figure note that there are waveguide modes

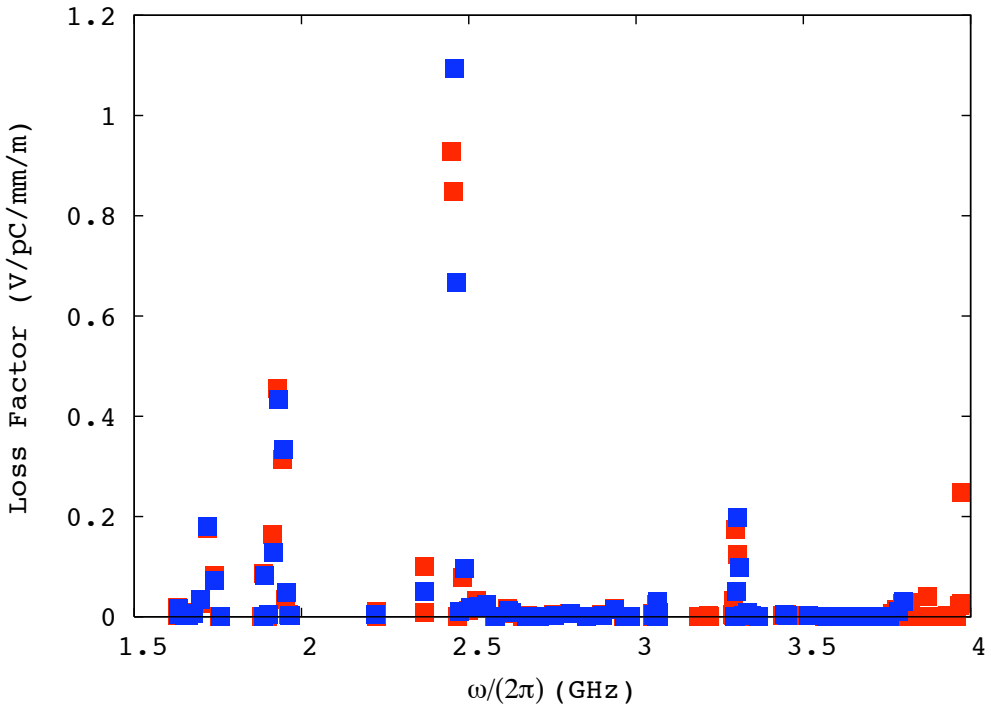


**Figure 7.5:** Dipole mode loss factors for the Ichiro cavity calculated using GdfidL (red) and MAFIA 2D (blue). The MAFIA results were prepared by Burt [78].

shown as well, these are identified as being well separated from the cavity dispersion curves with approximately $90^o$ phase advance (See section 7.3). Loss factors for each dipole mode were calculated, according to Equation 4.13. These results are displayed in Figure 7.5. Superimposed are the modal frequencies and loss factors calculated by the code MAFIA 2D [76, 77]. MAFIA is a finite difference code and, in this case, the 2D axis-symmetric system was discretized using 500,000 cells. These latter calculations were performed by G. Burt [78]. The Ichiro cavity was also simulated by J. de Ford & B. Held[1] using the parallel finite element code Analyst, before post-processing in Manchester. Figures 7.6 and 7.7 show the magnitude of the electric field for the first dipole mode in the third dipole band (at 2.4498 GHz)

[1]from STAAR Inc. now part of AWR Corporation

**Figure 7.6:** Magnitude of the electric field for the first dipole mode in the third dipole band (at 2.4498 GHz) as calculated with the Analyst code. Figure prepared by B. Held & J. de Ford.

and a multi-cavity mode in the region of the third dipole band (at 2.64203 GHz) [78]. In this case an adaptively refined, second order finite element mesh, consisting of more than $10^6$ elements in two dimensions, was used. The modal frequencies

**Figure 7.7:** Magnitude of the electric field for a multi-cavity mode in the region of the third dipole band (at 2.64203 GHz) as calculated with the Analyst code. Figure prepared by B. Held & J. de Ford.

and $R/Q$s calculated by the various codes are tabulated in Tables 7.1 and 7.2 (see also [78]).

### 7.2.3 Comparison of eigenmode results

As we have previously discussed in Chapter 6 we can expect the accuracy of a numerical simulation on a given mesh to decrease as the frequency increases, in particular as the wavelength approaches the mesh spacing. This effect can be verified by observing, in the above data, that as frequency increases the discrepancy between the four codes gets larger. For example, the first band modes, presented in Table 7.1, are no more than 1 MHz separated across the codes. Similarly, in the second band, the Analyst and GdfidL results are separated by less than 1 MHz, while HFSS differs by at most 1.7 MHz and MAFIA results are displaced furthest at a uniform displacement of $\sim 3$ MHz.

The third band demonstrates markedly different behaviour. The maximum difference between GdfidL and MAFIA has now increased to 7 MHz. HFSS shows a

| GdfidL short $\omega/2\pi$ | GdfidL R/Q short | GdfidL long $\omega/2\pi$ | GdfidL long R/Q | MAFIA short $\omega/2\pi$ | MAFIA R/Qs | HFSS short $\omega/2\pi$ | Analyst short$\omega/2\pi$ | Analyst short R/Q |
|---|---|---|---|---|---|---|---|---|
| 1.63035 | 0.385 | 1.63035 | 0.379 | 1.63094 | 0.342 | 1.63032 | 1.62941 | |
| 1.63044 | 0.050 | 1.63045 | 0.086 | 1.63109 | 0.119 | 1.63062 | 1.62950 | |
| 1.64907 | 0.039 | 1.64907 | 0.038 | 1.64927 | 0.045 | 1.64888 | 1.64816 | |
| 1.66102 | 0.080 | 1.66102 | 0.070 | 1.66133 | 0.066 | 1.66097 | 1.66015 | |
| 1.67769 | 0.202 | 1.67769 | 0.171 | 1.67812 | 0.150 | 1.67772 | 1.67687 | |
| 1.69757 | 0.568 | 1.69757 | 0.690 | 1.69813 | 0.713 | 1.69777 | 1.69679 | |
| 1.71897 | 3.639 | 1.71897 | 3.759 | 1.71971 | 3.713 | 1.71923 | 1.71826 | |
| 1.73962 | 1.672 | 1.73962 | 1.529 | 1.74050 | 1.473 | 1.73994 | 1.73892 | |
| 1.75578 | 0.002 | 1.75578 | 0.000 | 1.75680 | 0.000 | 1.75613 | 1.75511 | |
| 1.88201 | 0.000 | 1.88201 | 0.001 | 1.88507 | 0.000 | 1.88367 | 1.88158 | |
| 1.88522 | 1.615 | 1.88523 | 1.533 | 1.88830 | 1.541 | 1.88678 | 1.88480 | |
| 1.89865 | 0.004 | 1.89865 | 0.044 | 1.90172 | 0.073 | 1.90004 | 1.89815 | |
| 1.91403 | 3.041 | 1.91403 | 2.581 | 1.91709 | 2.380 | 1.91529 | 1.91343 | |
| 1.92902 | 8.365 | 1.92902 | 8.283 | 1.93207 | 7.950 | 1.93007 | 1.92832 | |
| 1.94216 | 5.705 | 1.94216 | 5.909 | 1.94519 | 6.079 | 1.94296 | 1.94135 | |
| 1.95274 | 0.623 | 1.95274 | 0.801 | 1.95576 | 0.867 | 1.95348 | 1.95183 | |
| 1.96044 | 0.082 | 1.96044 | 0.057 | 1.96343 | 0.040 | 1.96105 | 1.95943 | |
| 1.96509 | 0.052 | 1.96509 | 0.047 | 1.96807 | 0.039 | 1.96564 | 1.96402 | |
| 2.22302 | 0.174 | 2.20725 | 0.001 | 2.22185 | 0.083 | | | |
| 2.22302 | 0.004 | 2.20725 | 0.032 | 2.22185 | 0.083 | | | |
| | | 2.26551 | 0.099 | 2.36820 | 0.746 | | 2.39381 | 1.097 |
| | | 2.26551 | 0.228 | 2.36822 | 0.745 | | 2.39381 | 1.108 |
| 2.36660 | 0.128 | 2.36541 | 0.037 | 2.36822 | 15.739 | | 2.39381 | 14.884 |
| 2.36660 | 1.499 | 2.36541 | 0.985 | 2.36822 | 9.588 | | 2.39381 | 9.700 |

**Table 7.1:** Modal frequencies, $\omega/2\pi$ (GHz) and $R/Q$s (Ohms/cm$^2$) for the first two dipole bands, calculated using GdfidL, MAFIA, HFSS and Analyst. "Short" and "long" mark simulations made with 150 mm and 172 mm beam pipe sections, respectively.

similar, albeit smaller, frequency deviation from GdfidL. The modes from the Analyst simulations, which were performed with the highest resolution mesh, show an unexpected behaviour.

The frequencies of the lower four modes in the third band, which are in a low group velocity region, are only deviated from the GdfidL results by 1 MHz. However, this difference between the GdfidL and Analyst result begins to rise from the fifth mode and the final mode in the band is shifted by 26 MHz. A frequency shift of the order of 10 MHz could usually be expected from a significant change in the cavity

| GdfidL short $\omega/2\pi$ | GdfidL R/Q short | GdfidL long $\omega/2\pi$ | GdfidL long R/Q | MAFIA short $\omega/2\pi$ | MAFIA R/Qs | HFSS short $\omega/2\pi$ | Analyst short $\omega/2\pi$ | Analyst short R/Q | Analyst long $\omega/2\pi$ | Analyst long R/Q |
|---|---|---|---|---|---|---|---|---|---|---|
| 2.44882 | 13.393 | 2.44875 | 14.986 | 2.45610 | 0.154 | 2.45421 | 2.44978 | 0.078 | 2.44940 | 14.922 |
| 2.45507 | 12.229 | 2.45475 | 11.471 | 2.46210 | 1.370 | 2.46033 | 2.45609 | 1.324 | 2.45344 | 9.948 |
| 2.46556 | 0.020 | 2.46462 | 0.083 | 2.47221 | 0.271 | 2.47039 | 2.46671 | 0.184 | 2.45640 | 0.164 |
| 2.48040 | 1.129 | 2.47772 | 1.308 | 2.48654 | 0.297 | 2.48493 | 2.48176 | 0.327 | 2.45985 | 1.202 |
| 2.52290 | 0.188 | 2.49125 | 0.264 | 2.50509 | 0.351 | 2.50383 | 2.50135 | 0.273 | 2.46859 | 0.050 |
| 2.52290 | 0.443 | 2.50140 | 0.024 | 2.52765 | 0.001 | 2.52670 | 2.52542 | 0.014 | 2.48288 | 1.122 |
| 2.54957 | 0.265 | 2.51266 | 0.000 | 2.55351 | 0.170 | 2.55297 | 2.55350 | 0.197 | 2.50180 | 0.164 |
| 2.57804 | 0.016 | 2.53200 | 0.215 | 2.58107 | 9.126 | 2.58094 | 2.58363 | 0.168 | 2.52473 | 0.312 |
| 2.61523 | 0.222 | 2.55826 | 0.166 | 2.61877 | 0.020 | 2.61766 | 2.64203 | | 2.54992 | 0.300 |
| 2.62637 | 0.096 | 2.58672 | 0.012 | 2.62793 | 0.002 | | 2.66659 | | 2.57189 | 0.000 |

**Table 7.2:** Modal frequencies, $\omega/2\pi$ (GHz) and $R/Q$s (Ohms/cm$^2$) for the third dipole band, calculated using GdfidL, MAFIA, HFSS and Analyst. "Short" and "long" mark simulations made with 150 mm and 172 mm beam pipe sections, respectively.

geometry. In contrast, an 8 MHz shift is observed following a 1 mm change in the cell radius at the equator due to electron-beam welding [79]. In order to investigate this effect further GdfidL simulations were commissioned in which the end cell geometry was perturbed. Specifically, the horizontal half-axis of the ellipse which defines the equator region was perturbed by 0.05 mm.

Under these perturbed conditions certain modes show significant sensitivity, in particular the lowest two dipole modes in the first band shift by $\sim 0.1$ MHz. The field for these two modes is strongly localized in the end cells and beam pipe region. The difference for the lowest lowest modes in the third dipole band was just 0.005 MHz compared to the 0.2 MHz shift observed for the higher frequency modes in the band. Figure 7.6 shows the electric field in the modes at 2.4488 GHz, which is trapped in the inner cells of the cavity.

To contrast this trapped mode Figure 7.7 displays a mode which exists throughout the cavity and through the region of the beam tubes. This latter mode is also located in the region of the third band and can be described as a 'multi-cavity' mode. This type of mode exhibits a sensitivity to the length of the beam tubes used in simulations and exposed a difference in the geometries modelled by GdfidL and

Analyst.

In the GdfidL simulations a beam pipe length of 172 mm was chosen, equivalent to 1.5 cell lengths at either end of the cavity. In Tables 7.1 and 7.2 simulations with the 172 mm pipes are referred to as "long". In the Analyst case the beam pipes were 150 mm long, referred to as "short" in the Tables. We made additional simulations in order to investigate the sensitivity to the beam pipe length. GdfidL simulations were performed with 3 cell lengths of beam pipe attached to either end of the cavity and while new Analyst calculations employed 4.5 cell lengths. As expected, those modes whose field is well contained within the cavity revealed little sensitivity to the pipe length. The first mode in the third dipole band, at 2.44882 GHz, for example, shifted by approximately 70 kHz in the GdfidL simulations, the expected accuracy is not expected to be better than several hundred kHz. Modes with significant field in the end-cell and pipe region were, however, markedly effected. The $9^{\text{th}}$ mode in the third dipole band shifted down in frequency by 57 MHz from 2.615 GHz. For the Analyst result, with the longest beam pipes, the same mode shifted down by 92 MHz from 2.642 GHz.

The above results demonstrate that the electric field of the first mode in the third dipole band, which has the largest $R/Q$, does not penetrate to the beam tube region. This is significant since it may well not be damped effectively by higher order mode couplers located outside the cavity. Further, this mode is sensitive to the exact end cell configuration. Small perturbations in the end cell geometry may redistribute the field and allow the mode to be damped. The present asymmetric design of the TESLA cavity is a response to a similarly poorly damped mode in the previous generation in which the cavity was longitudinally symmetric [23].

## 7.3 Beam pipe modes

Figures 7.10 and 7.11 both show points marked in the "stop bands" i.e. between the dipole band dispersion curves. The field pattern for these modes is strongly localised to the region between the main cavity and the simulation boundaries. Very little field is present in the central regions of the cavity. These modes are closely related

to the modes present if a section of cylindrical pipe was simulated alone. In the same manner that the transition to beam pipes perturbs the cavity modes away from those expected if there was an infinite chain of cells, the boundary conditions imposed by the presence of the cavity against the pipe section perturbs the waveguide modes. For the dispersion diagrams the phase of the main cavity modes was calculated using the Floquet condition on the field in the central region. For these modes, with no field in the centre of the cavity, this algorithm is not valid and the modes were reported with an "artificial" phase of $\pi/2$ and hence appear in the centre of the plots.

## 7.4 Long Range Wakefields

The transverse long range wakefield experienced by a bunch train is given by [52]:

$$W_T(t) = 2\sum_p K_p \sin(\omega_p t)\, e^{-\frac{\omega_p t}{2Q_p}} \tag{7.4}$$

where $\omega_p/2\pi$, $K_p$ and $Q_p$ are the modal frequencies, kick factors and damping $Q$s respectively for the dipole modes $p$. The definitions of transverse wakefield and kick factor were introduced in Chapter 4, see also Equation B.53. Consider the vertical case, the wake can be both positive or negative implying a kick to the bunch either upwards or downwards. In the operation of the linac we are equally concerned with kicks in either direction and in particular the maximum amplitude of that kick, hence we evaluate the absolute value of the sum in Equation 7.4 - the envelope of the transverse wakefield, representing the maximum excursion in the amplitude of the wakefield at a given $t$.

The envelope of the transverse wakefield is displayed in Figures 7.8 and 7.9 for the reentrant and Ichiro cavities respectively. The black line shows the rapidly varying wake, oscillating for each mode in the sum, while the red dots in each figure mark the location of the bunches, i.e. the wake the bunch will see on arriving at the cavity. A crucial aspect of the long range wakefield is the rate at which the wake decays, these plots show the wake decaying through six orders of magnitude. To aid the comparison between the cavities the wakes have been normalized with respect

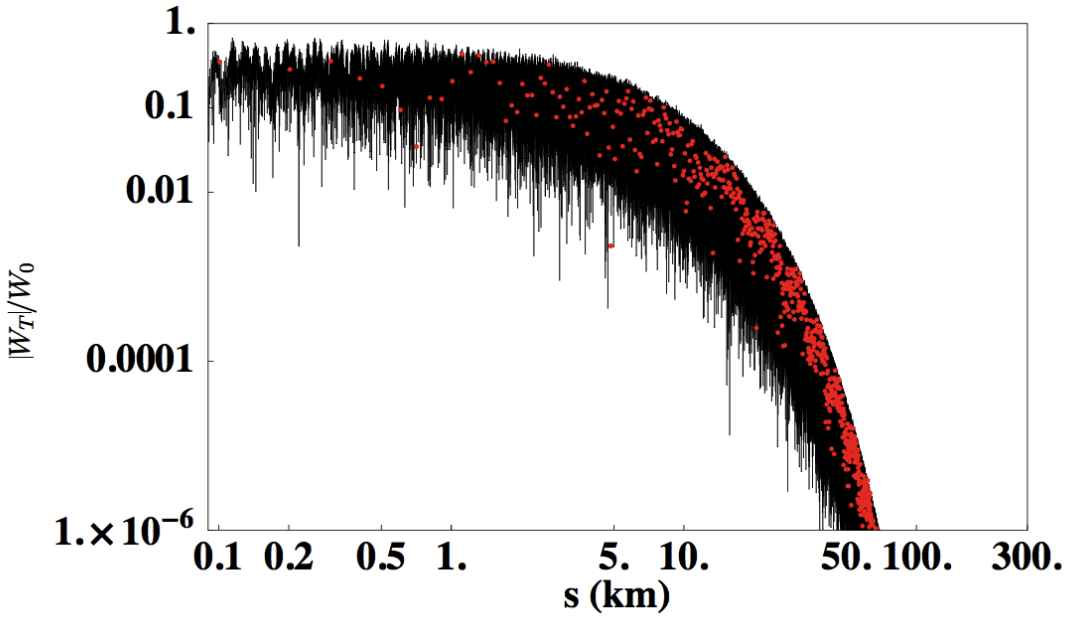


**Figure 7.8:** Envelope of the long range transverse wakefield for the Reentrant cavity with Q=$10^5$, and normalized with respect to $W_0$ = 0.16V/pC/mm/m. Points show the locations of the bunches.

to the wake at the first bunch, 0.16 V/pC/mm/m and 0.147 V/pC/mm/m for the reentrant and ichiro cavities respectively. For this work a, conservative, damping $Q$ of $10^5$ has been applied to all modes. In both cases the figures show the wake has decayed away through by six orders of magnitude in less than 75 km i.e. before the $700^{\text{th}}$ bunch, for a bunch spacing of 369 ns. Contrast this with the 2625 bunches in the complete ILC bunch train.

In effect we have, at the exit of a cavity, measured the rapidly varying wakefield effect on the second bunch due to the first, on the third bunch due to the combined effect of the first and then second, and so on.

These transverse long range wakefields are also employed by the code LIAR in order to calculate the beam dynamics properties and emittance growth resulting from transporting the multibunch beam through the 16,000 main linac cavities of the ILC. These beam dynamics simulations are discussed in detail in Chapter 8.

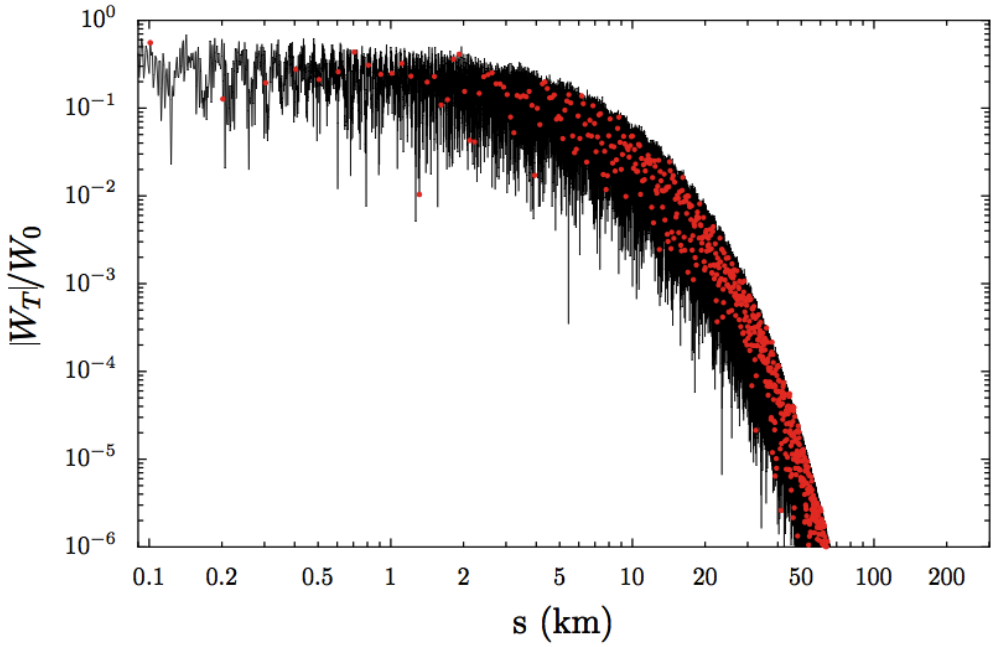


**Figure 7.9:** Envelope of the long range transverse wakefield for the Ichiro cavity with Q=$10^5$, $W_0 = 0.1472$V/pC/mm/m. Points show the locations of the bunches.

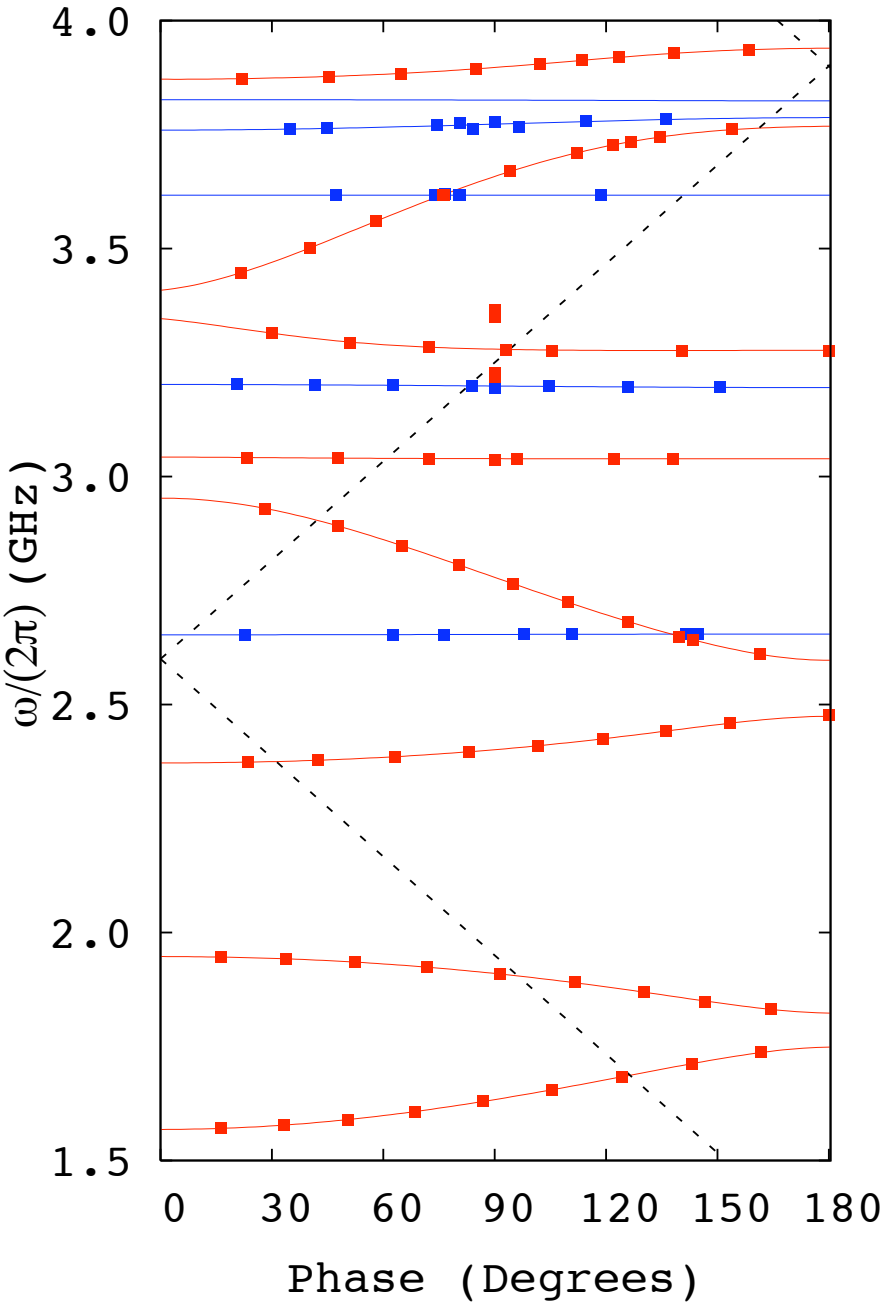


**Figure 7.10:** Brillouin diagram showing the phase and frequency of Reentrant cavity dipole(red) and sextupole(blue) modes. The solid curves are the single cell dispersion curves.

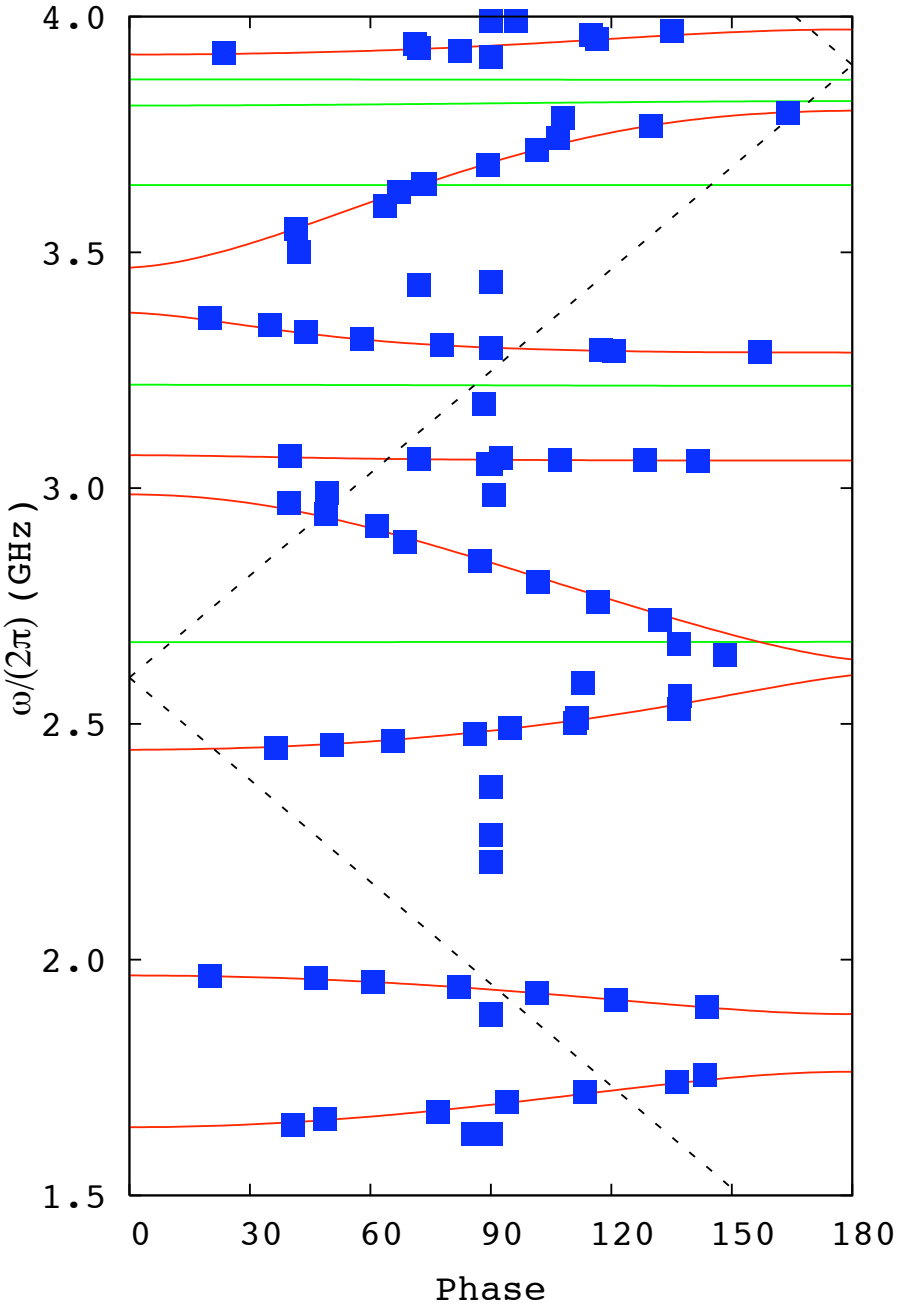


**Figure 7.11:** Dispersion curves showing dipole (red) and sextupole (green) bands, with cavity modes (blue) for the Ichiro cavity.

# Chapter 8

# Beam Dynamics Simulation Results

The main linacs could be a major source of degradation in the beam quality at the ILC. Here the emittance can be diluted by a number of factors including energy spread, phase jitter in cavities, beam position feedback errors, quadrupole magnet misalignments and wakefield effects. Here we focus on the dilution in the transverse emittance due to transverse wakefields and in particular on long range wakefields due to higher order modes in the accelerating cavities [14]. These wakefields have been calculated from detailed simulations of the cavity eigenmodes, discussed in Chapter 7, and are now utilized in beam dynamics codes which track multi-bunch beams through the lattice of the main linac.

## 8.1 Emittance definition

The quantity emittance was first mentioned in the introduction. In a real accelerator we are concerned with particle bunches and trains of bunches in a beam. We have an ensemble of particles which have a range of positions and momenta (amplitudes and phases in their orbit through the machine). The emittance of a bunch in a particular plane, the vertical plane for example, is proportional to the area in phase space $y-y'$ enclosing the beam. It can be calculated from the second order moments of the particle distribution about the bunch centroid:

$$\overline{y^2} = \frac{1}{q}\sum_i q_i(y_i - \overline{y})^2, \quad \overline{y'^2} = \frac{1}{q}\sum_i q_i(y'_i - \overline{y'})^2 \tag{8.1}$$

and

$$\overline{yy'} = \frac{1}{q}\sum_i q_i(y_i - \overline{y})(y_i' - \overline{y'}) \tag{8.2}$$

as

$$\epsilon_y = \sqrt{\overline{y^2 y'^2} - \overline{yy'}^2} \tag{8.3}$$

where the over-bars imply an average over the bunch. For a Gaussian bunch, a good approximation at the entrance to the linac, the bunch occupies an ellipse in phase space. Considering first just the drift spaces, bending dipole magnets and focussing quadrupole magnets in the lattice we have a system in which the bunches are acted on by conservative forces, that is, Liouville's Theorem applies. The area in phase space is conserved throughout the motion - one sees the ellipse rotate its axis, but not shrink or grow. For the the main linac the act of accelerating the bunches is non-conservative so we work with the "normalized emittance", defined as;

$$\epsilon_N = \gamma\epsilon_y \tag{8.4}$$

which is conserved throughout acceleration. Here $\gamma$ is usual the relativistic factor. During acceleration the particles undergo adiabatic damping, the angle of the particle $y'$ decreases since the longitudinal momentum increases while the transverse momentum remains constant.

Electrons and positrons in the linac are governed by the equation of motion [6, 39]:

$$\frac{1}{\gamma(s)}\frac{d}{ds}\left(\gamma(s)\frac{dy}{ds}\right) + K_y(s)y(s) = \frac{1}{\rho(s)}\frac{\Delta p(s)}{p(s)} \tag{8.5}$$

where $y$ is the offset from the design trajectory in the vertical plane at a given position $s$. $\rho(s)$, $p$, $\Delta p$ and $K_y(s)$ are the bending radius, design momentum, momentum deviation and the focussing strength of the magnets at position $s$, respectively.

Through linear elements of the lattice such as the drift spaces and focussing quadrupole magnets "transfer matrices" can be used as a proxy for Equation 8.5 and provide the particle position and angle $y'$ resulting from transport from one location to another:

$$\begin{pmatrix} y \\ y' \end{pmatrix}_{s_2} = \mathbf{M}_{12}\begin{pmatrix} y \\ y' \end{pmatrix}_{s_1}. \tag{8.6}$$

The solution to Equation 8.5 can be written in terms of the Twiss Parameters, $\alpha$, $\beta$ and phase $\mu$ [80]:

$$y(s) = \sqrt{a^2\beta\hat{(}s)}\cos(\mu(s) - \mu_0), \tag{8.7}$$

$$y'(s) = \sqrt{\frac{a^2}{\hat{\beta}(s)}}(-\alpha(s)\cos(\mu(s) - \mu_0) - \sin(\mu(s) - \mu_0)). \tag{8.8}$$

Here $\hat{\beta}(s)$ is the well known *beta function* and is a property of the lattice configuration. The other parameters are derived from $\hat{\beta}$. $\alpha(s) = -1/2\, d\hat{\beta}(s)/ds$ represents the divergence of the bunch trajectory, while $\mu(s) = \int_0^s ds/d\hat{\beta}(s)$ is the betatron phase advance. The particles execute betatron oscillations about the design orbit with amplitude $a$. The Twiss parameters are further related through the Courant-Snyder invariant:

$$\gamma y^2 + 2\alpha y y' + \beta y'^2 = \epsilon_y, \tag{8.9}$$

where here $\gamma = \frac{1+\alpha^2}{\beta}$, $y' = \frac{dy}{ds}$ is the divergence angle and $\epsilon$ is the emittance. A rigorous exposition of this area was delivered by Wolski from the Hamiltonian perspective in his "Linear Dynamics" lectures to The Cockcroft Institute [81].

The beam tracking codes LIAR [82], Lucretia [83] and PLACET [84] simulate particle motion under these equations, with representations for each magnet element in the lattice. Further, they treat transverse wakefield effects in cavities as perturbations to this motion - each cavity in the lattice applies a transverse momentum kick to the particles according to the prescribed wakefield. These codes make it possible to investigate the behaviour of a particular lattice, the impact of short or long range wakefields and the potential of various steering and correction algorithms to mitigate issues arising from misalignments etc. Here we make particular use of the capability to simulate the effect of long range wakefields on multi-bunch beams.

## 8.2 Combined Systematic Frequency Shifts and Detuning

A fictitious linac made up of identical cavities with identical modal frequencies would impart the same kick coherently from cavity-to-cavity to the accelerated beam. This

clearly would resonantly drive BBU and lead to severe emittance dilution. In constructing the ILC linacs approximately 16,000 cavities will be required. During industrial fabrication of these cavities small manufacturing errors will inevitably occur. These will cause each cavity to exhibit slightly different modal frequencies and effectively interleave the resonances. Thus, errors in the frequencies of the modes will occur as a natural consequence of fabricating these cavities and will allow BBU and severe emittance dilution to be avoided. Nonetheless, there will still be emittance dilution and we investigate this by subjecting the beam to an initial injection offset of $\sim \sigma_y/3$ and tracking it down the complete linac.

The simulations detailed here incorporated the manufacturing errors by calculating 50 wakefields based on randomly detuned modal frequencies with an RMS spread of 1 MHz, 3 MHz or 10 MHz and with, initially, a uniform damping Q of $10^6$. These 50 wakefields are then randomly distributed through the length of the linac, i.e. between the cavities, by LIAR before beam tracking occurs. The results presented here are the average of 100 machines formed with different random number seeds. The complete ILC beam consists of 2625 bunches and we utilised the USCold lattice [85]. The projected emittance for the whole beam was recorded at the end of the tracking procedure.

As shown in Equation 7.4 the amplitude of the wakefield depends on $\sin(\omega_p t)$. Random and systematic fabrication errors will alter the mode frequencies as described earlier. The time $t$ is determined by the bunch spacing. Should any modes lie such that $\omega t$ is close to $\pi/2 + 2n\pi$ or $3\pi/2 + 2n\pi$ $(n = 0, 1, 2, ...)$ then resonant BBU could occur. In this section we wish to investigate the effect of a systematic shift in the modal frequencies on emittance growth due to the long range wakefield. Having calculated wakefields for cavities with *random* errors and provided these as input for LIAR to track we make a simple transformation in order to make the systematic shifts prior to tracking. The transformation is to vary the bunch spacing by a small fractional amount ($\pm 0.1\%$) as a single input rather than recalculate all the input wakefields i.e. to adjust the $t$ rather than $\omega$ in $\omega t$.

Figure 8.1 contrasts the resulting emittance dilutions for linacs made up of Reentrant and Ichiro cavities and provided with uniform damping of $10^6$ and random

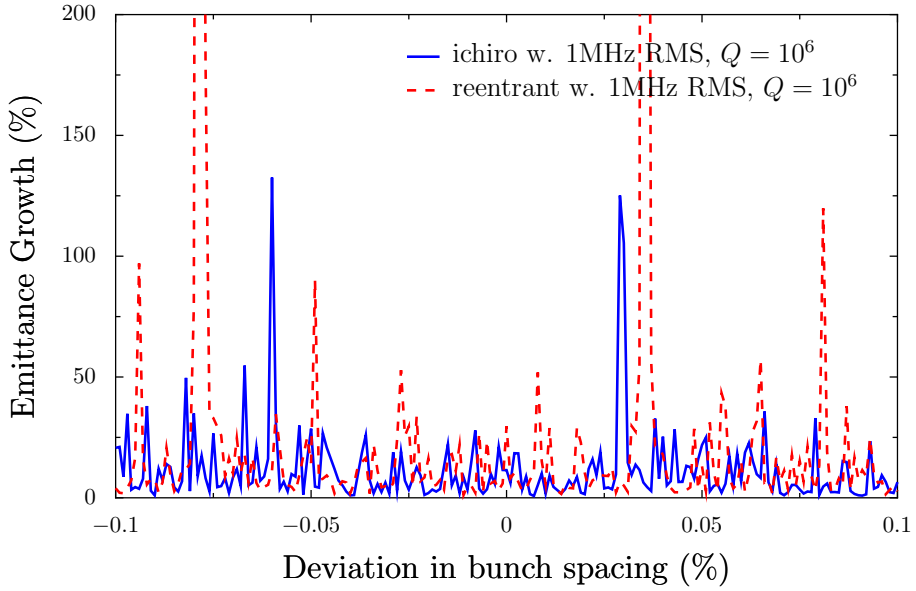


**Figure 8.1:** Emittance dilution as a function of deviation in the bunch spacing, ($Q = 10^6$, 1 MHz RMS spread).

frequency spread of 1 MHz. The abscissa in all cases is fractional deviation in the bunch spacing from the nominal design value of 369 ns. In order to assess the dependence of emittance dilution on the spread in frequency errors we increased the RMS random detuning of the higher order modes to 3 MHz and 10 MHz respectively. These results are displayed in Figures 8.2 and 8.3. In all cases we see little dependence on the specific value of the RMS introduced, as expected.

Damping of the Higher Order Modes will be provided by damping couplers which, with careful design, should allow damping to a $Q$ of $10^5$ or below [86]. Figures 8.4 and 8.5 show the emittance dilution resulting in the case of 1 MHz and 3 MHz RMS spread and a uniform damping $Q = 10^5$ for all modes. It is interesting to consider the case in which optimal damping of all modes has not been achieved and while some are well damped, a limited number of modes remain poorly damped. Such modes are often trapped away from the higher order mode couplers and end cells. In Figure. 8.6 the case of sub-optimal damping is considered. Here $Q = 10^5$ has only been achieved for the five modes with largest kick factors, which are the most destructive to the beam, the rest of the modes considered were simulated using $Q = 10^6$. This we refer to as targeted damping of the modes as we focus on

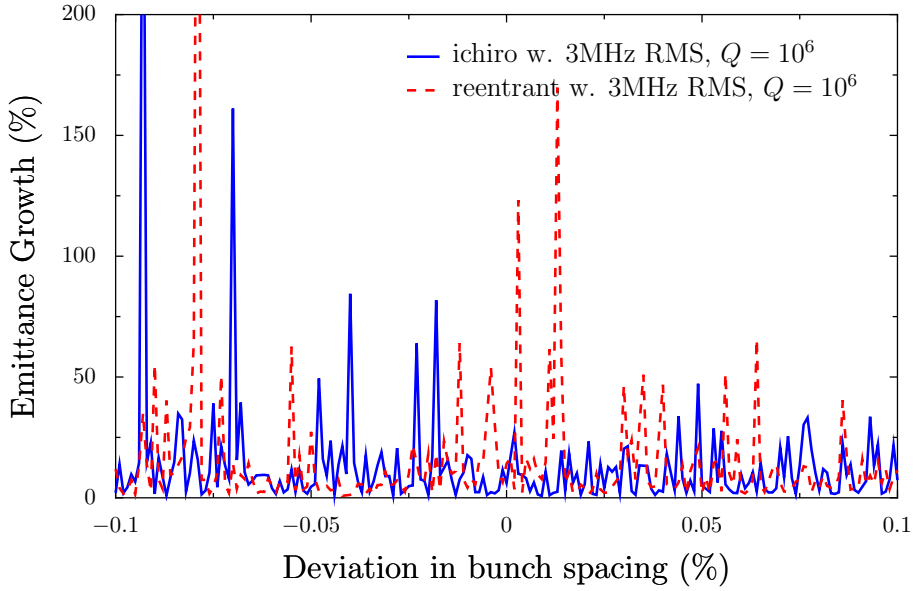


**Figure 8.2:** Emittance dilution as a function of deviation in the bunch spacing, ($Q = 10^6$, 3 MHz RMS spread).

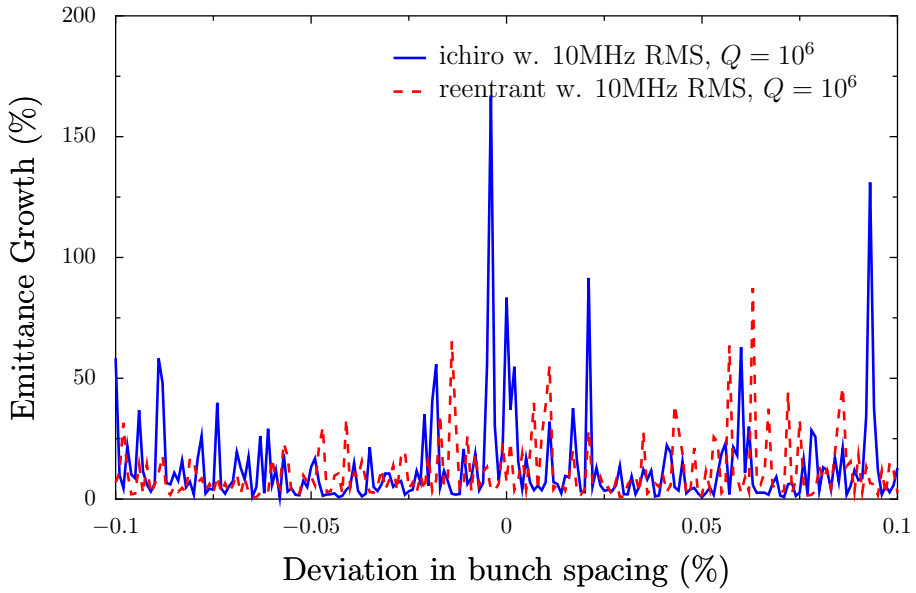


**Figure 8.3:** Emittance dilution as a function of deviation in the bunch spacing, ($Q = 10^6$, 10 MHz RMS spread).

damping a limited number of modes properly. We investigate the implications on emittance dilution of allowing the remaining modes to be non-optimally damped. This simulation reveals that provided the modes with the highest kick factors are well-damped the emittance dilution is well-contained it is below 10% in all cases.

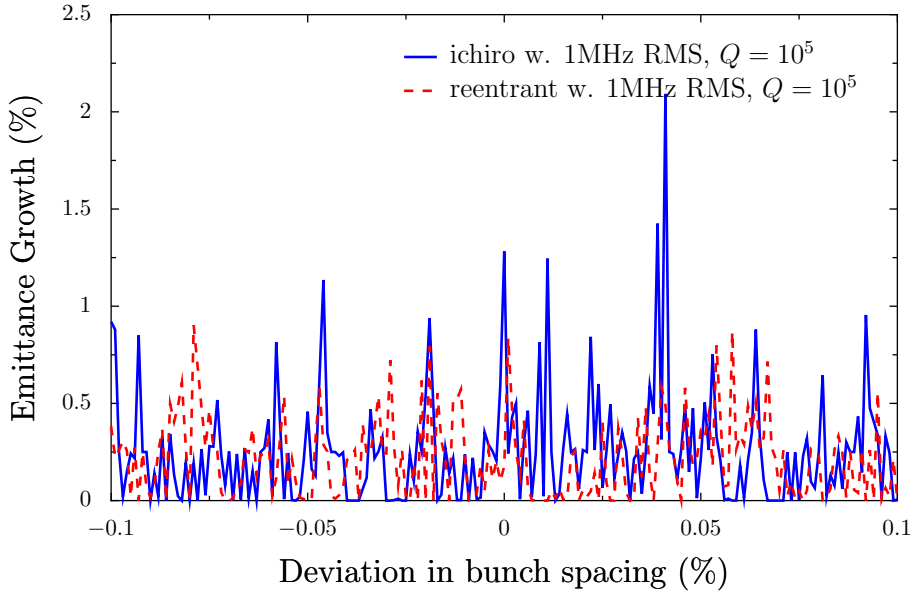


**Figure 8.4:** Emittance dilution as a function of deviation in the bunch spacing, ($Q = 10^5$, 1 MHz RMS spread).

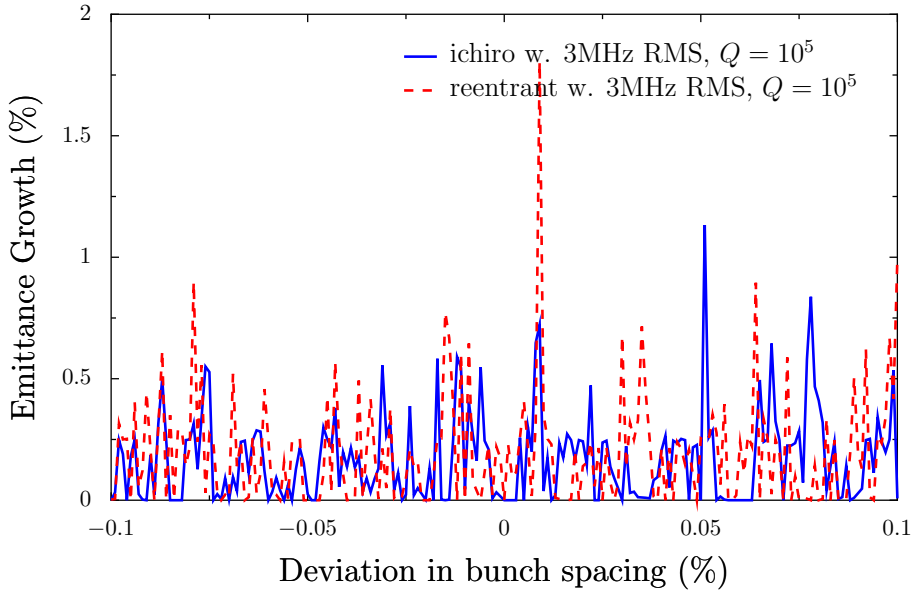


**Figure 8.5:** Emittance dilution as a function of deviation in the bunch spacing, ($Q = 10^5$, 3 MHz RMS spread).

## 8.3 Normally distributed frequency errors

The simulations detailed here undertaken using the Matlab-based code Lucretia incorporated the manufacturing errors by generating 100 sets of dipole mode frequen-

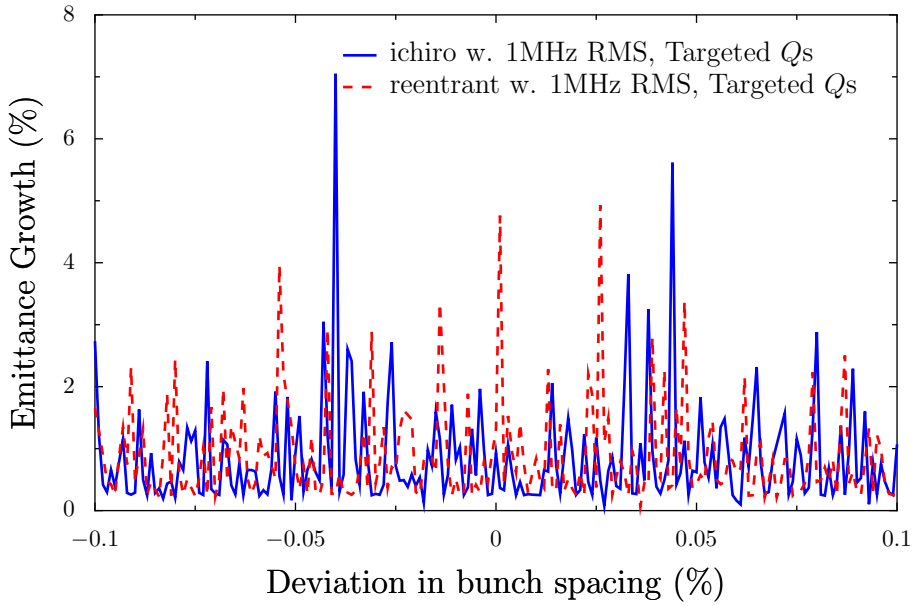


**Figure 8.6:** Emittance dilution as a function of deviation in the bunch spacing, (Targeted Damping, 1 MHz RMS spread).

cies in which each mode has been shifted by a random number generated according to a Normal distribution, these define 100 different cavity types. These cavity types are then randomly distributed throughout the linac before beam tracking occurs. In this case we applied a 1 MHz spread to the dipole modes and a uniform damping Q of $10^6$. Trains of 500 bunches were then tracked through the linac with the nominal bunch spacing of 369 ns [16], each bunch was injected with an offset of $6\mu m \sim \sigma_y$.

Figure 8.7 shows the dilution in the projected emittance for the bunch train at each beam position monitor position in the lattice that results from tracking down 40 machines, each with generated with a different random seed, made up of TESLA (21%) cavities. Curves showing the mean and one standard deviation from the mean are also displayed. Figures 8.8 and 8.9 present the results for machines consisting of Reentrant (27%) and Ichiro (31%) cavities respectively.

Figure 8.10 displays a comparison of the mean value of the emittance dilution for each cavity type.

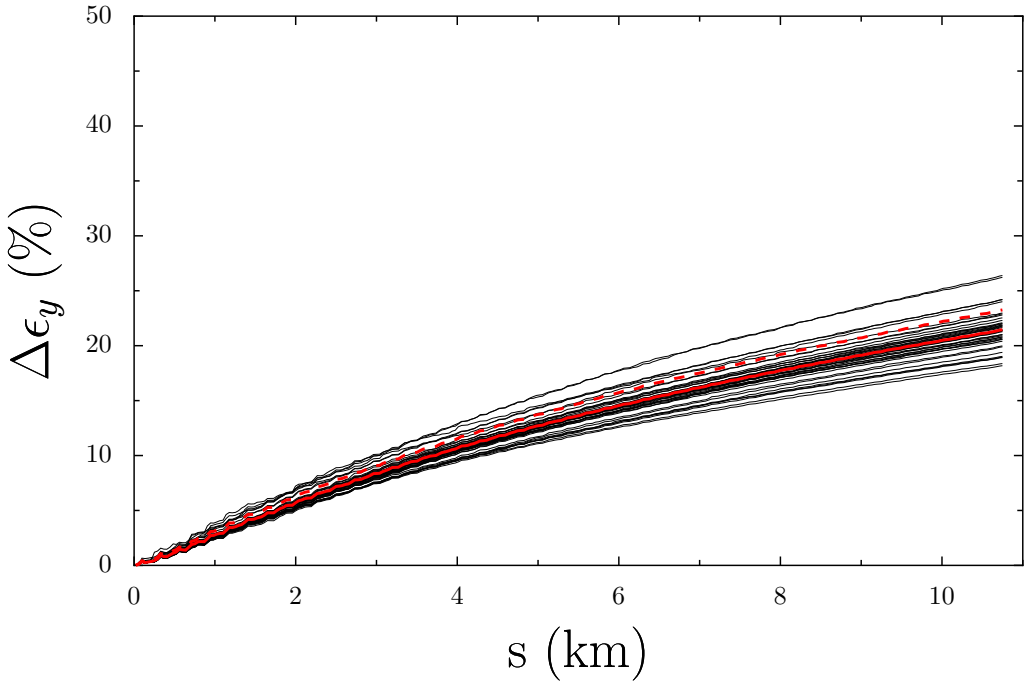


**Figure 8.7:** Emittance dilution simulated with Lucretia for 40 machines consisting of TESLA cavities. The mean curve is displayed in red, with one standard deviation dashed.

## 8.4 Summary

Taking the mode frequencies and kick factors calculated in Chapter 7 as input to LIAR and Lucretia this chapter has described the first direct comparison of beam dynamics in ILC linacs constructed with the Reentrant and Ichiro cavities (Section 8.2).

The vertical emittance growth due to long range wakefields has been calculated in multiple scenarios, showing that the collider is tolerant to random frequency errors due to the fabrication process up to 10 MHz provided the modes are well damped. It has been shown that *targeted* damping of the five most significant dipole modes to $Q = 10^5$, while leaving the remainder sub-optimally damped at $Q = 10^6$, is sufficient to reduce the emittance growth to less than 10% across a range of bunch spacings (equivalent to systematic shifts in the modal frequencies) - see Figure 8.6.

At the nominal bunch spacing beam dynamics simulations with Lucretia were undertaken, using the ILC2007b lattice, and built from a larger population of cavity

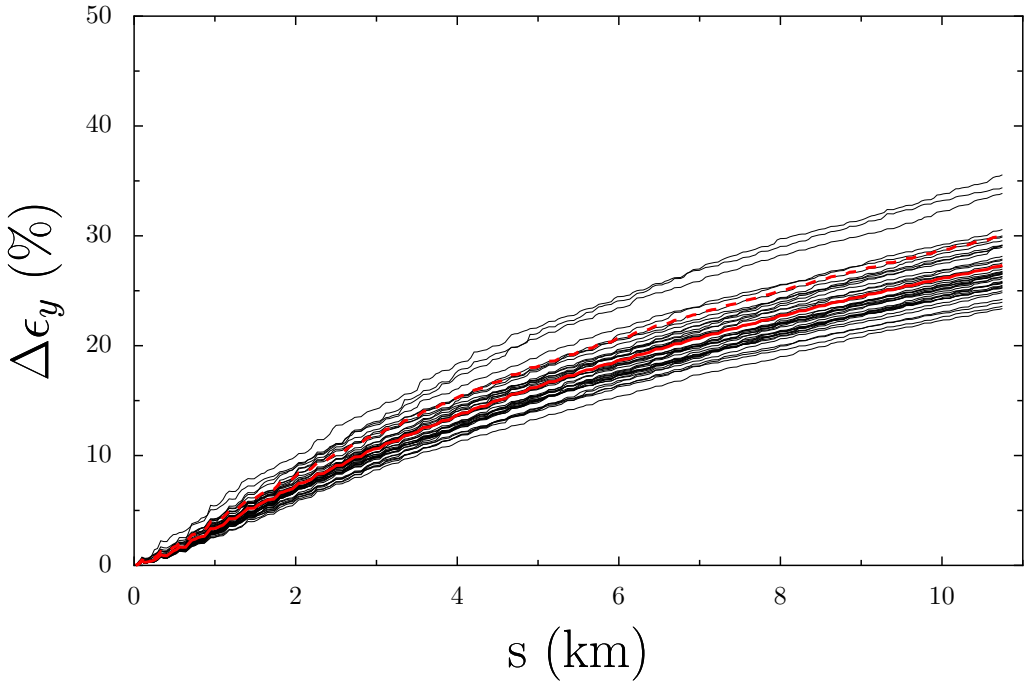


**Figure 8.8:** Emittance dilution simulated with Lucretia for 40 machines consisting of Reentrant cavities. The mean curve is displayed in red, with one standard deviation dashed.

"types" - a better approximation to the real situation in which all 16,000 cavities would differ slightly (Section 8.3). These simulations have shown that the emittance dilution across the three cavity types is of the same order and within the allowed emittance budget for the main linacs, however the Ichiro design is the most sensitive showing 31% growth.

In the next chapter beam dynamics results which demonstrate the importance of the crab cavity system to maintaining high luminosity at linear colliders are presented. In particular the optimal deflecting voltage is determined for the CLIC beam delivery system and the combined effect of the crab deflection and multipole corrector magnets is considered.

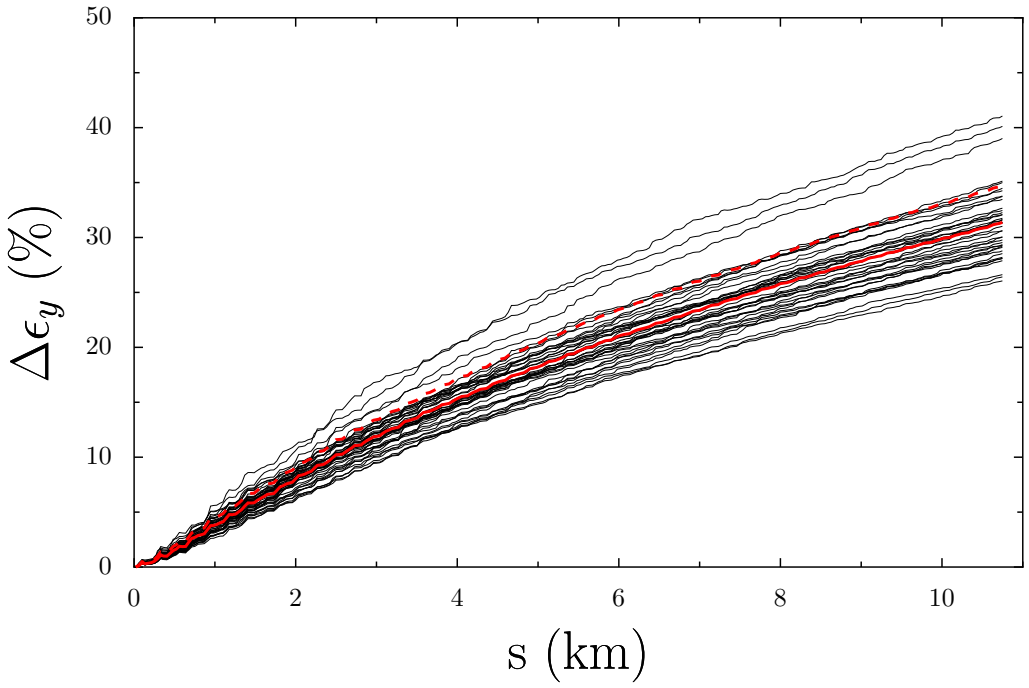


**Figure 8.9:** Emittance dilution simulated with Lucretia for 40 machines consisting of Ichiro cavities. The mean curve is displayed in red, with one standard deviation dashed.

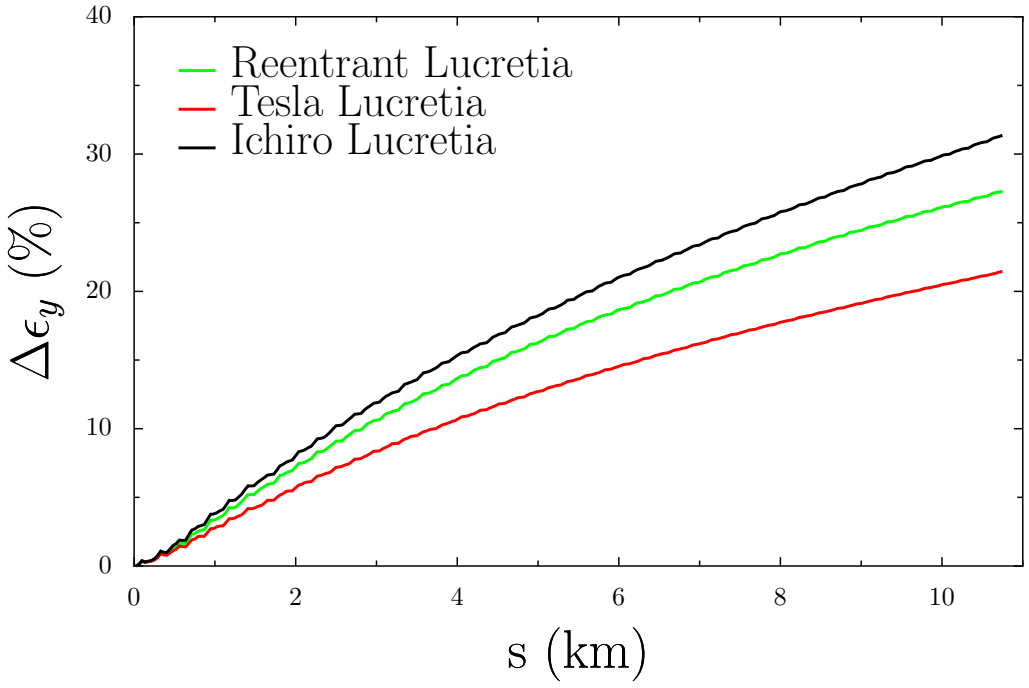


**Figure 8.10:** Comparison of the mean value of the emittance dilution for each cavity type.

# Chapter 9

# Beam dynamic simulations of the CLIC crab cavity

Previous chapters have detailed the efforts and techniques used to provide high quality low emittance bunches to the interaction region. After collision the bunches are highly disrupted - the bunch shape has been distorted due to beamstralung and there is a large energy spread. Further, positrons are now passing 'backwards' through the electron delivery magnets and vice versa. The technical considerations required to safely extract these disrupted bunches to beam dumps lead to a collider design incorporating a small crossing angle, 14 mrad in the case of the ILC [16] and 20 mrad for CLIC [7].

By introducing this crossing angle the achievable luminosity is reduced compared to that of the optimal "head on" case [87]. This loss is intolerable for both the ILC and CLIC designs as it would serve to make the colliders uneconomic and unnecessarily delay Particle Physics analyses. A system to mitigate and reduce this loss must be introduced. The leading system in both cases is that of a set of crab cavities.

In this chapter the idea of a crab cavity is briefly introduced to provide context for a series of beam dynamics simulation results which show the impact of the corrective crab cavity system on achievable collision luminosity at CLIC. In particular the collective effect of the crab cavity and the high order multipole magnets in the beam delivery system is investigated. This work has been published in the paper Shinton et al. [88] in which the cavity design work by Burt was combined with beam

| Overall parameters | Symbol | Value |
|---|---|---|
| Centre of mass energy | $E_{cm}$ | 3 TeV |
| Main linac frequency | $f_{RF}$ | 11.994 GHz |
| Number of particles per bunch | $N_b$ | $3.72\times10^6$ |
| Number of bunches per pulse | $k_b$ | 312 |
| Bunch separation | $\Delta t_b$ | 0.5 (6 periods) |
| Bunch train length | $\tau_{train}$ | 156 |

**Table 9.1:** CLIC main linac parameters [89, 90]

dynamics simulations performed by the present author and I.R.R. Shinton. Main linac parameters for CLIC are shown in Table 9.1, while Table 9.2 details the beam parameters utilized by PLACET for the beam delivery system.

## 9.1 Crab Cavities

A crab cavity or cavity operating in a "crabbing mode" is a transverse mode RF cavity distinct from the accelerating cavities discussed in detail earlier in this thesis. The primary mode of operation is the $TM_{110}$-like hybrid mode of an iris loaded cavity [88]. The transverse electric and magnetic fields which compose this mode act together to kick the head and tail of the bunch in opposite directions, within the same plane - such that the bunches are rotated. Achieving this effect requires careful tuning of the crab cavities. Only when the phase is such that the centre of the bunch passes through the centre of the cavity when the magnetic field is zero will the desired rotation take place alone. Should there be some phase error the bunch will be, overall, deflected transversely. This effect is illustrated in Figures 9.1 and 9.2.

## 9.2 Analytic Estimations

The luminosity reduction factor due to the crossing angle can be estimated using Equation 9.1, from [87]. For the current CLIC parameters where $\sigma_z = 44$ $\mu$m,

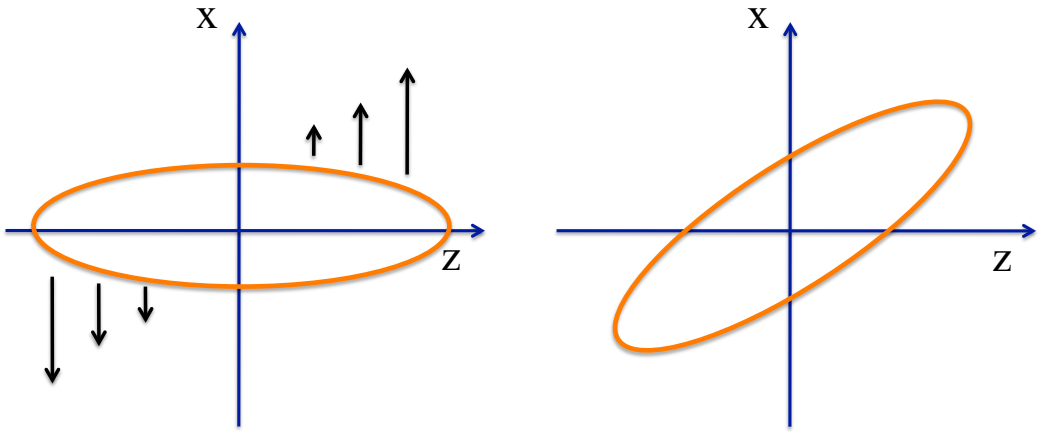


**Figure 9.1:** Sketch showing the rotation achieved by the crab cavity field for a bunch arriving on phase.

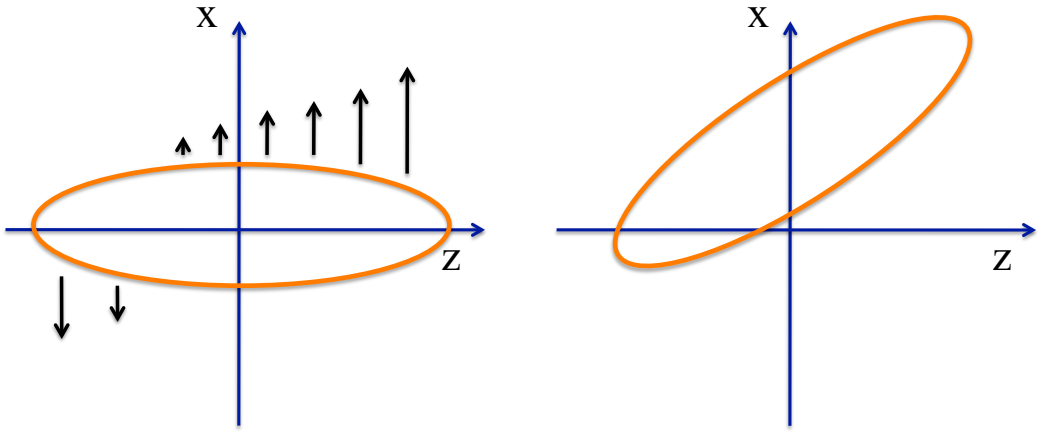


**Figure 9.2:** Sketch showing the combined rotation and transverse kick applied to a bunch with a phase offset, such that the bunch arrives early.

$\sigma_x = 45$ nm and $\theta_c = 0.02$ the reduction factor is 9.95% [89, 91].

$$\frac{\Delta L}{L} = \left(1 + \left(\frac{\sigma_z \theta_c}{2\sigma_x}\right)^2\right)^{\frac{1}{2}} \tag{9.1}$$

The deflecting voltage $V_\perp$ required from the crab cavity to correctly rotate the

| Beam delivery System plus IP | Symbol | Value |
|---|---|---|
| Crossing angle at IP | $\theta_c$ | 20 mrad |
| Bunch length | $\sigma_s$ | 44 |
| Initial RMS energy spread | $\sigma_{\Delta E/E}$ | 0.029 |
| Horizontal IP beta function | $\beta_x^*$ | 6.9 |
| Vertical IP beta function | $\beta_y^*$ | 0.068 |
| Horizontal IP beam size before pinch | $\sigma_x^*$ | 45 |
| Vertical IP beam size before pinch | $\sigma_y^*$ | 1 |
| Transverse horizontal emittance (norm) | $\gamma\epsilon_x$ | 660 |
| Transverse vertical emittance (norm) | $\gamma\epsilon_y$ | 20 |

**Table 9.2:** CLIC beam delivery system parameters [89, 90]

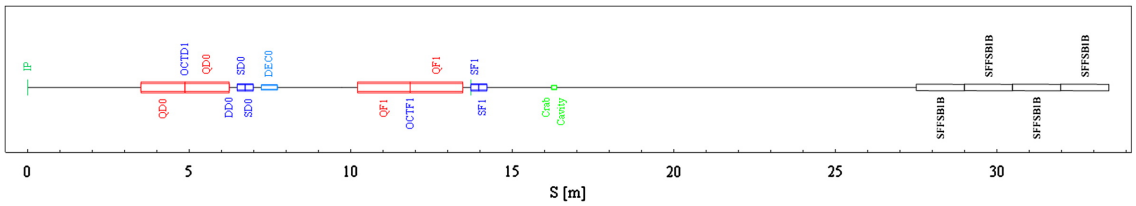


**Figure 9.3:** Schematic of the final 32 m section of the CLIC BDS, including the location of the crab cavity.

bunches can also be estimated using Equation 9.2.

$$V_\perp = \frac{\theta_c E_0 c}{4\pi f R_{12}}, \tag{9.2}$$

where $E_0$ is the beam energy, $f$ the operating frequency of the cavity, 12 GHz and $R_{12}$ is the element of the transfer matrix which relates the offset at the IP to the $x'$ at the crab cavity - see Equation 9.3 and Figure 9.3. For the current design $R_{12}$ is 23.4 m [92], resulting in a required voltage of $\sim 2.55$ MV.

$$\begin{pmatrix} X \\ X' \end{pmatrix}_{\text{IP}} = \begin{pmatrix} R_{11} & R_{12} \\ R_{21} & R_{22} \end{pmatrix} \begin{pmatrix} x \\ x' \end{pmatrix}_{\text{crab}} \tag{9.3}$$

## 9.3 Finding the optimum crab cavity gradient and tolerances

For a given accelerator lattice, bunch specifications, centre of mass energy and crossing angle there will be an optimum setting at which the crab cavity acts to produce the maximum luminosity [93, 92].

The simulations detailed here used PLACET [84] as the particle tracking code and the code GUINEA-PIG [94, 95] to take the distorted beams from PLACET and calculate the luminosity. Full details of the simulation setup and recent modifications to PLACET to allow crab cavity elements to be accurately modelled are given in [88].

Particle tracking commenced from the entrance to the CLIC beam delivery system. The input bunches had idealised Gaussian distributions according to tables 9.2, 9.1 and were injected on axis. Neither wakefield nor synchrotron radiation effects were considered in these simulations.

Individual PLACET simulations take place in their own coordinate frames, defined by the direction of acceleration. Thus, in order to mimic the crossing angle which would exist at the interaction point (IP) in the physical collider the position and momenta of bunches must be numerically transformed prior to passing to GUINEA-PIG .

A straightforward rotation matrix in two dimensions is used, this matrix, $R$, is defined in Equation 9.4. The vertical plane is not involved in the rotation.

$$R = \begin{pmatrix} \cos\theta & \sin\theta \\ -\sin\theta & \cos\theta \end{pmatrix} \tag{9.4}$$

where $\theta$ is the angle of rotation.

In this case we rotate the electron bunches through the full 20 mrad, equivalent to 10 mrad rotations of both the electron and positron bunches.

In Figure 9.4 the variation of luminosity with applied crab cavity voltage $V_0$ is displayed. A cubic spline fit has been applied [96]. The voltage which results in the

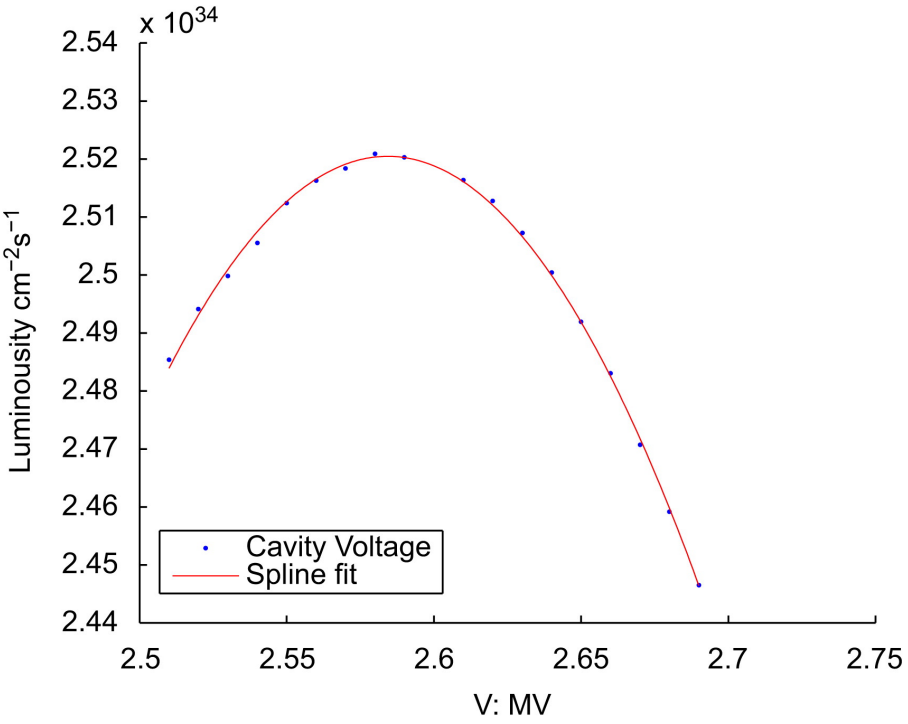


**Figure 9.4:** Collision luminosity calculated by GUINEA-PIG for a range of crab cavity voltages i.e. for a range of bunch rotations.

desired bunch rotation, and therefore the maximum luminosity, is given by the peak of the curve as 2.58 MV. This figure agrees well with the estimate from Section 9.2

Having established the correct operating voltage the tolerances to phase differences between the cavities and to roll about the beam axis can be investigated.

### 9.3.1 Phase and Roll tolerance

Fixing the phase on the positron line and applying a varying phase offset to the electron line crab cavity one can see the effect on luminosity in Figure 9.5. The 98% requirement results in a tolerance of $\pm 0.02°$. This value matches closely with that expected from analytical considerations. Dexter et al. have estimated the tolerance to a relative phase difference between the electron and positron line crab cavities as $0.019°$ [92].

The roll tolerance measurement was performed in a similar fashion. Again the positron line was kept fixed while a small roll was imparted to the crab cavity in the electron line lattice. Roll about the beam axis changes the plane of crab rotation

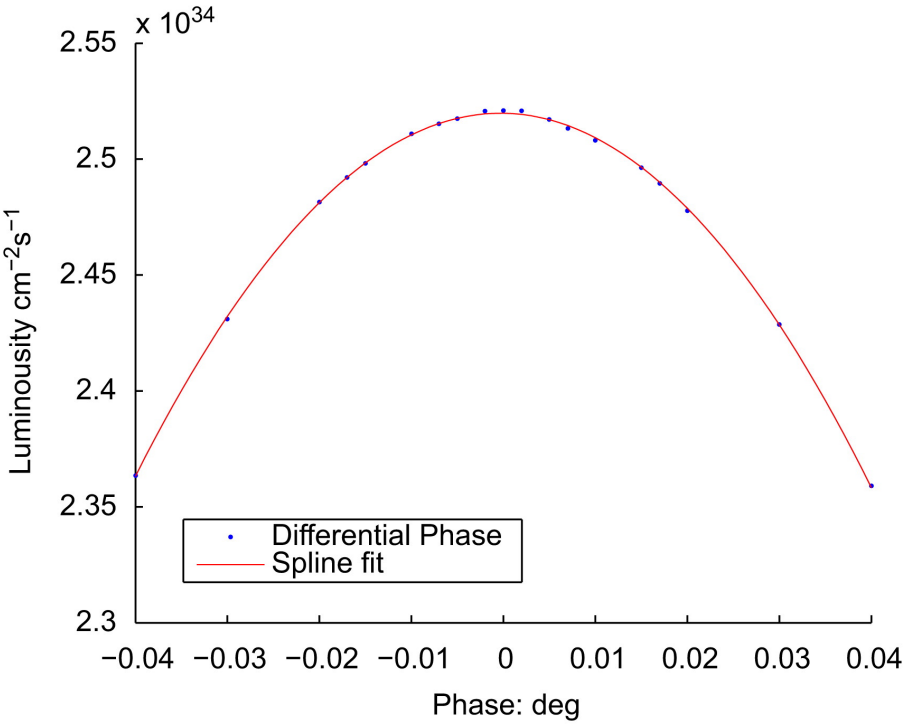


**Figure 9.5:** Luminosity as a function of phase offset applied to to the crab cavity system.

from purely in the horizontal $x-z$ plane into one having a component in the vertical plane. It therefore leads to bunch offsets at the IP. The tolerance is determined to be extremely tight at 5.9 millidegrees (0.1 mrad).

## 9.4 Unexpected Luminosity Degradation

When comparing with the nominal head on case, calculated with PLACET and GUINEA-PIG in the same fashion, but with no crab cavity elements in the lattice, an unacceptable drop in luminosity is observed. The luminosity with crossing angle and crab cavity system is 10% lower than that of the head on case.

In Figure 9.6 the $z-y$ bunch distribution at the IP is displayed in the form of RMS value of the $y$ displacement for each slice in $z$. The head on case and the crab cavity rotated case are shown, in red and blue respectively. This vertical beam size shows a slight increase in the rotated case, particularly at the head and tail of the bunch.

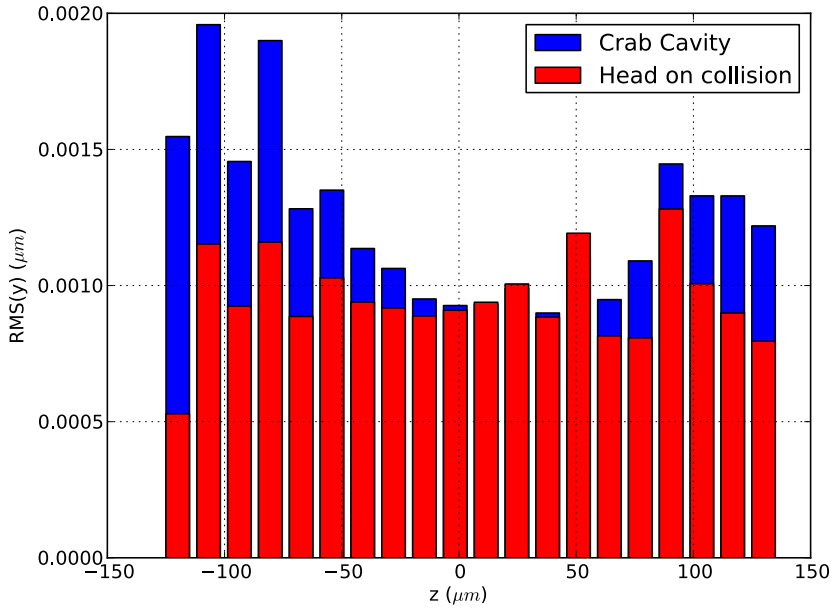


**Figure 9.6:** Here the RMS value of the $y$ displacement is shown for individual slices of the bunch in $z$. The head-on collision is shown in red and the crab cavity corrected 20 mrad crossing angle case appears in blue.

Similarly, Figure 9.7 shows a comparison of the $y - y'$ phase space of electron bunches for each case. In the rotated case there has been some distortion in the phase space. Recall that the crab operates in the $x - z$ plane for a crab cavity without roll angle and also that the emittance in the vertical plane must be kept small to suppress beamstrahlung.

From the previously described figures the source of this increase in luminosity is not readily identified. There are a number of nonlinear effects that may be responsible and the other elements in the beamline must therefore be considered. In particular the $y-y'$ distribution of Figure 9.7 which shows some correlation between $y$ and $y'$ for particles away from the core indicates the action of a sextupole magnet. Two sextupoles are present in the lattice downstream of the crab cavities in order to correct chromatic aberration at the IP. They impart a kick in the vertical plane

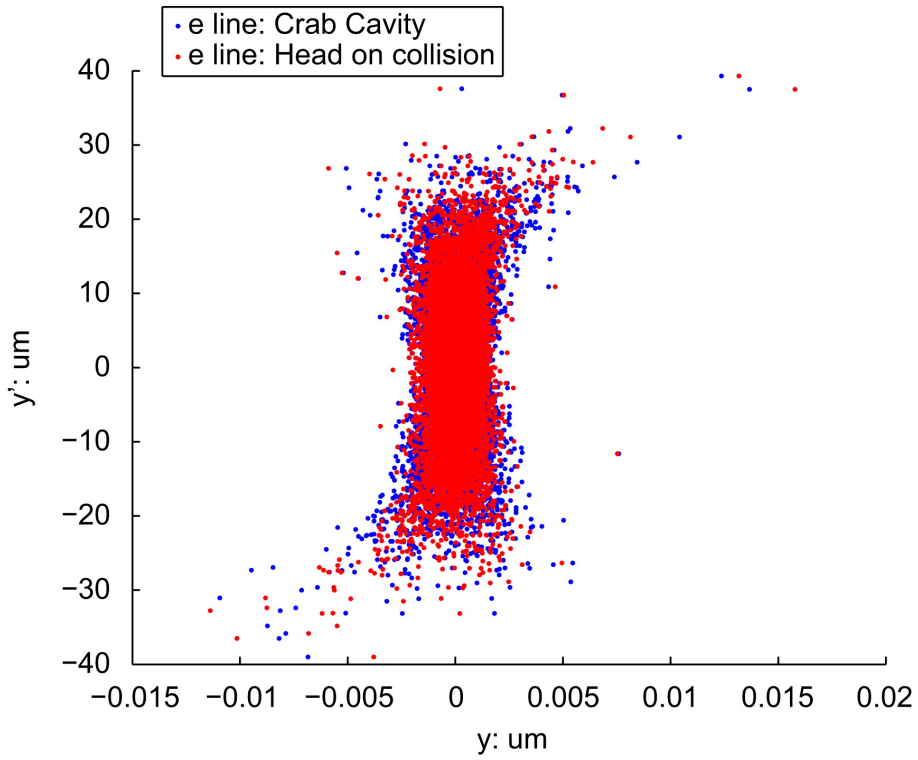


**Figure 9.7:** Particle distribution in $y-y'$ space for the case of a head-on collision (red). Overlaid with the, crab cavity corrected, 20 mrad crossing angle case (blue).

dependent on the product of $x$ and $y$ displacements[1]:

$$\Delta y = kxy. \tag{9.5}$$

The crab rotation applies the greatest kick at the head and tail of the bunch in order to correctly rotate the bunch, but solely in the $x$-plane. Figure **??** shows greater displacement in the $y$ plane at the head and tail of the bunch. It is likely that the sexupole kick is translating the horizontal offset imparted by the crab in vertical emittance degradation and luminosity reduction.

Simply removing the sextupoles from the lattice leaves the chromaticity uncorrected and the bunches reaching the IP are therefore much distorted. In simulation it is possible to eliminate the chromatic effects by reducing the bunch energy spread to zero and performing the tracking again. The bunch remains highly distorted due to the effect of a decapole magnet, present in the lattice only to control multipole

[1]See the full equation of motion in Raubenheimer [26] or Chao's book [97]

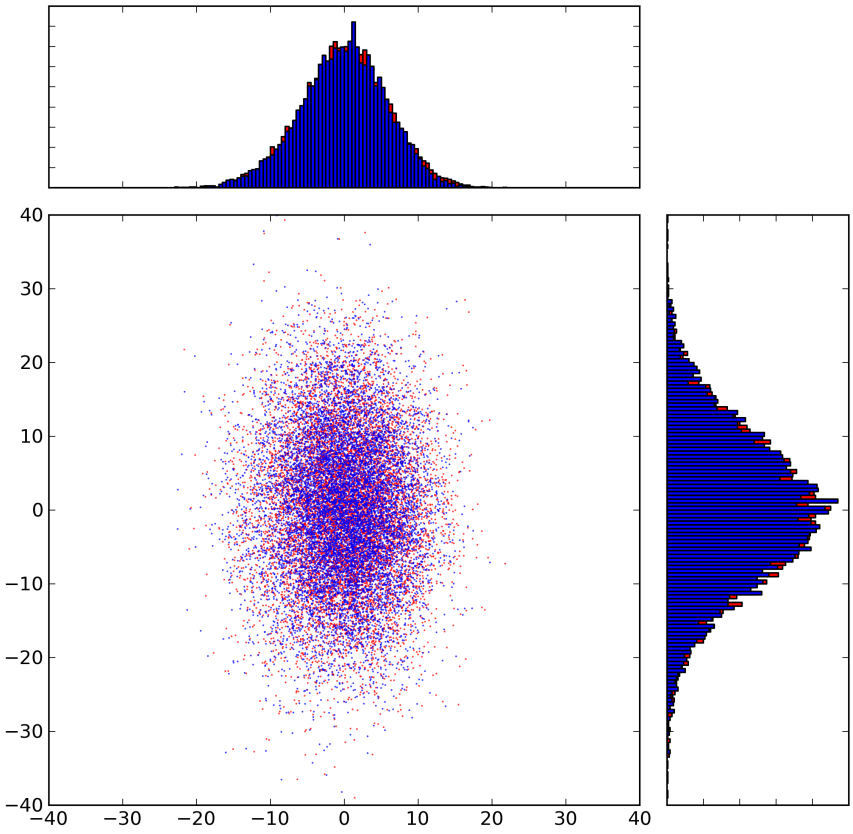


**Figure 9.8:** Particle distribution in $(x' - y')$ for the case of a head-on collision (red). Overlaid with the, crab cavity corrected, 20 mrad crossing angle case (blue). In this case tracking occurred with zero energy spread and the sextupole and decapole magnets downstream of the crab cavity have been turned off.

errors from the sextupoles. Finally we can deactivate that magnet's effect in the lattice as well. This data is presented in Figure 9.8. Here there is no discernible difference between the case of head on collisions and the crab cavity rotated case. In fact the luminosity is now equal for both cases.

## 9.5 Summary

Beam dynamics simulations of the 1.5 TeV CLIC beam were performed, tracking through the beam delivery system to the IP, contrasting with the 250 GeV ILC

main linac simulations considered elsewhere in this thesis. Analytic estimations of the crabbing voltage required, differential phase tolerance and roll tolerance have been verified with PLACET simulations, see Sections 9.2 and 9.3.1. In particular, it was shown that a crab cavity operating at 2.58 MV will act to rotate the bunches through the 10 mrad angle required to maximise collision luminosity at the IP (in the case of a 20 mrad crossing angle BDS design).

These studies entailed inserting the crab cavity into the CLIC beam delivery system lattice and then performing multiple beam dynamics studies, passing the tracked and rotated bunch populations to GUINEA-PIG which calculates the luminosity of the collisions, see Figure 9.5 for example.

An unexpected and intolerable degradation of the luminosity was observed even when operating at the optimum crabbing voltage, i.e when the bunches had been rotated correctly. Section 9.4 describes the investigation undertaken to track this problem to the combined effect of the crab deflection with the sextupole and decapole magnets, placed in the lattice to correct chromaticity errors prior to the final focus. The lattice should be modified to mitigate this issue.

In the next chapter a brief overview of the results contained in this thesis is presented followed by some concluding remarks.

# Chapter 10

# Conclusion

This thesis details finite difference electromagnetic simulations of two high gradient accelerating cavity designs for the ILC. The eigenmodes calculated have been used to calculate transverse wakefields and further employed in multiple beam dynamics simulations. The higher order mode damping required to achieve the nominal emittance and luminosity required for the ILC has been verified. These simulations have demonstrated that ILC linacs made up of the new high gradient cavities would meet wakefield requirements for delivering high quality beams for particle physics studies. This result is important since any upgrade of the ILC from 500 GeV to 1 TeV centre of mass energy would make use of one of these high gradient cavity designs in the extension to the linacs.

A study of beam dynamics in the beam delivery system at CLIC has also been detailed. These simulations included the crab cavity system and were compared to estimates from geometric and analytic considerations as well as the expected and required behaviour. The crab cavity is necessary in order to restore the luminosity lost in the crossing-angle configuration due to collisions no longer occurring "head-on" at the interaction point.

Dispersion curves for the Cornell designed Reentrant cavity have been produced. Dipole modes up to 4 GHz were simulated for the full 9-cell cavity design, with 35 mm iris radius, using GdfidL. Having an iris radius equal to that of the TESLA cavities the Reentrant shows a broadly similar pattern of modes, the highest $R/Q$ mode is present in the 3$^{\text{rd}}$ dipole band in both cases for example. We note, however, a mode at 3.936 GHz which has a significant $R/Q \sim 2$ Ohms/cm$^2$ (Section 7.2.1).

If this mode is not well damped then unacceptable emittance dilution could occur due to the long range wakefields generated.

Similarly, the Ichiro cavity, designed at KEK was simulated. A good agreement is found between results from the GdfidL, MAFIA 2D, HFSS and Analyst simulation packages. Where discrepancies were found beyond that which can be expected simply from the different mesh discretizations further careful investigations were carried out. These investigations led to the identification of certain modes which do not show sensitivity to the applied boundary conditions. Notably the first $3^{\text{rd}}$ band dipole mode at 2.4498 GHz appears to be trapped, displaying little field in the region of the end cells and showing negligible sensitivity to the boundary conditions applied in simulation (Section 7.2.3).

In both cases modes have been identified which must be borne in mind while optimizing the cavity end-groups and higher order mode couplers. TESLA cavities have an asymmetric end cell design in order to improve damping of previously trapped dipole modes. Modification of the end groups could be employed in a similar fashion for both the Ichiro and Reentrant cavities, which are longitudinally symmetric, in order to improve the coupling and damping of the modes described above.

The modes and wakefields described above, calculated from finite difference simulations, were used as the basis for the first direct comparison of beam dynamics in ILC linacs constructed with the Reentrant and Ichiro cavities (Section 8.2). The vertical emittance growth due to long range wakefields was calculated in multiple scenarios. It was demonstrated that targeted damping of the five most significant dipole modes to $Q = 10^5$, while leaving the remainder sub-optimally damped at $Q = 10^6$, is sufficient to reduce the emittance growth to less than 10% across a range of bunch spacings, equivalent to systematic shifts in the modal frequencies.

At the nominal bunch spacing beam dynamics simulations with Lucretia, incorporating an improved approximation of the population of cavities within the linac, were performed (Section 8.3). These simulations show that the emittance dilution across the three cavity types is of the same order and within the allowed emittance budget for the main linacs, however the Ichiro design is the most sensitive showing 31% growth.

Both the LIAR and Placet simulations demonstrate the importance that random fabrication errors have to the operation of the main linacs. If a linac was constructed from 16,000 identical cavities the emittance dilution resulting from the transverse wakefield generated would be catastrophic - beam break up would occur - driven by the resonant superposition of identical kicks from each cavity in the linac. While extreme care is taken during the construction and preparation of the superconducting cavities they are all different and each will require tuning to achieve the design frequency of the fundamental mode (1.3 GHz). Each of the cavities will have random errors in their higher order modes, leading to differing long range transverse wakefields. Rather than superpose constructively to cause BBU, the $\sin \omega t$ terms from Eq. 7.4 all have slightly different phases and therefore the combined "detuned" effect is much reduced and BBU is avoided.

Future work in this area should include higher order modes from the latest cavity designs (section 5.6) as well as $Q$ factors measured from bench tests of newly fabricated cavities. As is the case with all finite difference and finite element work the continued advance of Moore's Law and the expansion of computing hardware and memory available means that higher fidelity simulations will become possible, this is to be encouraged.

This work has benefitted from the "open source" nature of the beam dynamics codes Lucretia and PLACET . The authors of these codes have published extensively on the techniques used as well as being responsive to questions from fellow researchers. Further, the exact implementation of a particular physics process is always available in the supplied source code, for inspection or modification. Sadly this has not been the case for the electromagnetic field solvers which are commercial codes and proprietary in nature. A finite element Maxwell solver developed in house, even for axis-symmetric structures, would be beneficial. Such a code would allow extremely accurate solutions to be rapidly determined even for large problem geometries. In addition, the necessary customizations for geometry optimization, calculation of quantities derived from the raw fields and other tasks usually left to inefficient post-processing could be built into the main tool. Much of the groundwork has been done in other groups, for example the multi-physics finite element

library `oomph-lib` has been developed at Manchester in the School of Mathematics [98, 99].

Beam dynamics simulations of the beam delivery system at CLIC have shown the impact of the crab cavity system in maintaining the luminosity of the collider despite the crossing angle (Chapter 9). The required crab cavity voltage has been determined as 2.55 MV, in line with that expected from analytic estimations. The importance of incorporating the crab cavity effect in the design of the BDS has been emphasised by the unexpected 10% degradation in luminosity observed in simulations despite operating at the optimum crabbing voltage. It was demonstrated that responsibility lay with the combined effect of the crab cavity deflection and sextupole magnets present to correct chromatic errors. The BDS design must be modified to mitigate this effect.

The work presented in this thesis employed codes developed over the previous 15 years, running on desktops, servers and the Grid and touching upon numerical methods for solving Maxwell's equations, the physics of intense electron bunches in superconducting accelerating cavities and the beam dynamics of multi-bunch beams transported through thousands of beamline elements. Bunches have been tracked from the start of the main linacs through to the interaction point, highlighting some of the careful work which must be undertaken to produce a reliable linear collider delivering a high energy, high luminosity beam for particle physics studies.

# Appendix A

# Point Charge Wake function

Consider two particles, a driving particle $q_1$ and a test particle $q$, traveling with velocity $v \approx c$ both with a trajectory parallel to the axis of a cavity as shown in Figure A.1. The longitudinal and transverse position of the driving particle are $z_1$ and $\mathbf{r}_1$ respectively. Similarly, the coordinates of the test particle $q$ moving with the same velocity a distance $s$ behind are labeled $z$ and $\mathbf{r}$.

The electromagnetic fields $\mathbf{E}$ and $\mathbf{B}$ produced by the driving charge can be derived by solving Maxwell's equations with the proper boundary conditions.

$$\nabla \times \mathbf{B} = \mu_0 \mathbf{j} + \frac{1}{c_2} \frac{\partial \mathbf{E}}{\partial t} \tag{A.1}$$

$$\nabla \cdot \mathbf{E} = \frac{1}{\epsilon_0} \rho \tag{A.2}$$

$$\nabla \times \mathbf{E} = -\frac{\partial \mathbf{B}}{\partial t} \tag{A.3}$$

$$\nabla \cdot \mathbf{B} = 0 \tag{A.4}$$

For a point particle the charge and current density are written as

$$\rho(\mathbf{r}, t) = \delta^2(\mathbf{r} - \mathbf{r}_1)\delta(z - vt), \quad j(\mathbf{r}, t) = \mathbf{v}\, \rho(\mathbf{r}, t), \tag{A.5}$$

where $\delta^2$ denotes the delta function in two dimensions. The Lorentz force acting on the test charge at a given position $(\mathbf{r}, z)$ is given by Equation A.6,

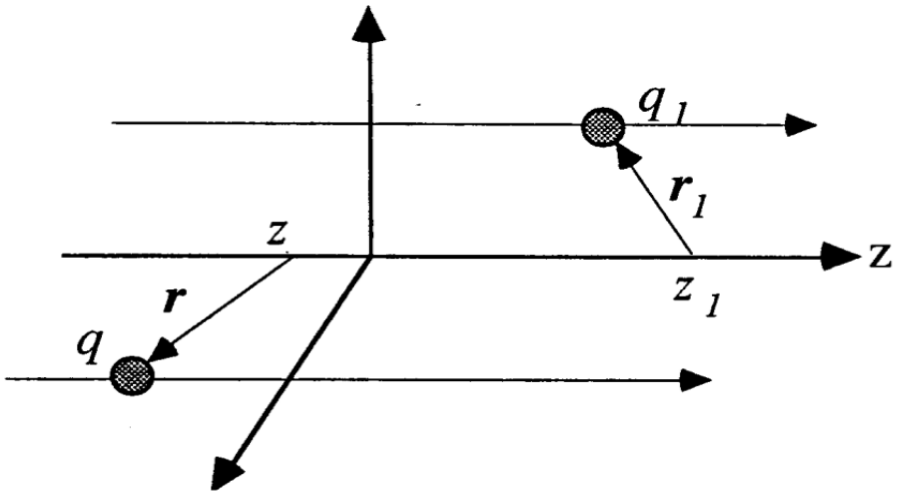


**Figure A.1:** Coordinates of a driving and a test charge traveling parallel to the $z$ axis of a cavity.

$$\mathbf{F}(\mathbf{r}, z, t) = q\,\mathbf{E}(\mathbf{r}, z, t) + q\,\mathbf{v} \times \mathbf{B}(\mathbf{r}, z, t). \tag{A.6}$$

Passage through the cavity produces changes in the energy and the transverse momentum of both particles. The test particle is affected by the fields generated by the driving particle, while the latter is affected by its interaction with the environment. The integrated forces along the length of the cavity, $L$ will also depend on the transverse position of the driving charge $r_1$. Thus, the *wake* force acting on a test charge is given by:

$$\mathbf{F}(\mathbf{r}, \mathbf{r}_1, z, t) = q[\mathbf{E}(\mathbf{r}, \mathbf{r}_1, z = vt - s, t) + v\,\mathbf{e}_z \times \mathbf{B}(\mathbf{r}, \mathbf{r}_1, z = vt - s, t)]. \tag{A.7}$$

The total change in momentum after passage through the cavity is obtained by integrating this wake force:

$$\Delta\mathbf{p}(\mathbf{r}, \mathbf{r}_1, s) = \int_L dt\,\mathbf{F}(\mathbf{r}, \mathbf{r}_1, z, t). \tag{A.8}$$

The variables $s$, $z$, and $t$ are related and therefore the integration with respect

to time can be replaced by an integration with respect to the longitudinal position $z$ of the driving charge, thus obtaining the following wake function:

$$\mathbf{W}^{\delta}(\mathbf{r}, \mathbf{r}_1, s) = \frac{1}{q} \int_{-\infty}^{\infty} dz \, [\mathbf{E}(\mathbf{r}, \mathbf{r}_1, z, t) + v \, \mathbf{e}_z \times \mathbf{B}(\mathbf{r}, \mathbf{r}_1, z, t)]_{t=(z+s)/v}, \tag{A.9}$$

where the superscript $\delta$ refers to the $\delta$-function properties of the driving charge. This function describes the shock response of a cavity due to the field created by a point like charged particle.

Consider now a line charge density $\lambda$ moving with constant velocity $\mathbf{v}$ in a trajectory parallel to the $z$ axis, $(\mathbf{r} = \mathbf{r}_1)$.

The wake potential at a distance $s$ with respect to a particle inside the bunch is obtained as follows:

$$\mathbf{W}^{\lambda}(\mathbf{r}, s) = \int_{-\infty}^{\infty} ds' \, \lambda(s') \, \mathbf{W}^{\delta}(\mathbf{r}, s - s'), \tag{A.10}$$

where the charge density is normalised to unity,

$$\int_{\infty}^{\infty} dz \, \lambda(z) \; = 1 \tag{A.11}$$

Hence, the wake function for a point like source is the Green's function for the wake potential of a line charge distribution.

The wake potential of a three-dimmensional bunch is calculated by superimposing the wake functions for different values of $\mathbf{r}_1$, weighted by the transverse charge distribution $\lambda(\mathbf{r}_1)$.

# Appendix B

# The Condon Method

Following the method laid out in the exposition by Bane *et al* [100], here we show how to calculate the longitudinal and transverse wakefields from the eigenmodes of electric field within an empty cavity. This rigorous approach is known as the Condon Method [40]. Some sections are expanded to clarify the method while others, treated in detail by Bane, are abridged.

## B.1 Fields In A Cavity

We define a vector potential $\mathbf{A}(\mathbf{x}, \mathrm{t})$ and a scalar potential $\Phi(\mathbf{x}, \mathrm{t})$ and can now write

$$\begin{aligned} \mathbf{B} &= \nabla \times \mathbf{A} \\ \mathbf{E} &= -\frac{\partial \mathbf{A}}{\partial t} - \nabla\Phi. \end{aligned} \tag{B.1}$$

We choose the Coulomb gauge and set $\nabla.\mathbf{A} = 0$. Using equations B.1 Maxwell's equation

$$\nabla \times \mathbf{B} = \mu_0 \mathbf{j} + \frac{1}{\mathrm{c}^2}\frac{\partial \mathbf{E}}{\partial \mathrm{t}} \tag{B.2}$$

becomes

$$\nabla^2 \mathbf{A} = \mu_0 \mathbf{j} - \frac{1}{\mathrm{c}^2}\frac{\partial^2 \mathbf{A}}{\partial \mathrm{t}^2} - \frac{1}{\mathrm{c}^2}\nabla\left(\frac{\partial \Phi}{\partial \mathrm{t}}\right). \tag{B.3}$$

Restricting consideration to within a closed cavity which has perfectly conducting walls we can expand the vector potential in terms of a complete and orthogonal set of vectors $\mathbf{a}_\lambda$ thus

$$\mathbf{A}(\mathbf{x},\mathrm{t}) = \sum_\lambda \mathrm{q}_\lambda(\mathrm{t})\mathbf{a}_\lambda(\mathbf{x}) \tag{B.4}$$

with

$$\nabla^2\mathbf{a}_\lambda + \frac{\omega_\lambda^2}{\mathrm{c}^2}\mathbf{a}_\lambda = 0 \tag{B.5}$$

and $\nabla.\mathbf{a}_\lambda = 0$. Also $\mathbf{a}_\lambda \times \hat{\mathbf{n}}$ on the metallic surface since it is perfectly conducting. The scalar potential is similarly expanded,

$$\Phi(\mathbf{x},\mathrm{t}) = \sum_\lambda \mathbf{r}_\lambda(\mathrm{t})\phi_\lambda(\mathbf{x}) \tag{B.6}$$

where

$$\nabla^2\phi_\lambda + \frac{\Omega_\lambda^2}{c^2}\phi_\lambda = 0, \tag{B.7}$$

with $\phi_\lambda = 0$ on the metallic surface. The $\phi_\lambda$ serve to account for any source terms present in the cavity. Now, expanding the vector and scalar potentials within Equation B.3 using Equations B.4 and B.6, we get

$$\sum_\lambda \left[\left(\ddot{q}_\lambda + \omega_\lambda^2 q_\lambda\right)\mathbf{a}_\lambda + \dot{\mathbf{r}}_\lambda \nabla\phi_\lambda\right] = \mu_0 c^2 \mathbf{j}. \tag{B.8}$$

Integrating over the cavity volume, using the orthogonality condition for the $\mathbf{a}_\lambda$, setting

$$\frac{\epsilon_0}{2}\int_V \mathbf{a}_{\lambda'}.\mathbf{a}_\lambda \mathrm{dV} = \mathrm{U}_\lambda \delta_{\lambda\lambda'}, \tag{B.9}$$

we obtain

$$\ddot{q}_\lambda + \omega_\lambda^2 q_\lambda = \frac{1}{2U_\lambda}\int_V \mathbf{j}.\mathbf{a}_\lambda \mathrm{dV}. \tag{B.10}$$

When there is no current in the cavity the righthand side of Equation B.10 drops to zero and the $q_\lambda$ are governed by a simple harmonic relation. It is now possible to write $\mathbf{A}$ as

$$\mathbf{A}(\mathbf{x}, \mathrm{t}) = \sum_\lambda \mathrm{C}_\lambda \mathbf{a}_\lambda \cos(\omega_\lambda \mathrm{t} + \theta_\lambda) \tag{B.11}$$

where $C_\lambda$ and $\theta_\lambda$ are determined by the initial conditions which generated the modes. The $\mathbf{a}_\lambda$ are eigenmodes of the cavity, when free from currents, with corresponding resonant frequencies $\omega\lambda$.

The $r_\lambda$ can be found in a similar fashion starting from

$$\nabla.\mathbf{E} = \frac{\rho}{\epsilon_0} \tag{B.12}$$

to get

$$r_\lambda = \frac{1}{2T_\lambda} \int_V \rho \phi_\lambda d\mathcal{V}, \tag{B.13}$$

with the $\phi_\lambda$ normalized by

$$\frac{\epsilon_0}{2} \int_\mathcal{V} \nabla\phi_{\lambda'}.\nabla\phi_\lambda d\mathcal{V} = T_\lambda \delta_{\lambda\lambda'}. \tag{B.14}$$

Putting this all together we can now write down the electric field

$$\mathbf{E} = -\sum_\lambda (\dot{\mathrm{q}}_\lambda \mathbf{a}_\lambda + \mathrm{r}_\lambda \nabla\phi_\lambda) \tag{B.15}$$

and the magnetic induction

$$\mathbf{B} = \sum_\lambda \mathrm{q}_\lambda \nabla \times \mathbf{a}_\lambda. \tag{B.16}$$

The stored energy can also be expressed as a sum

$$\begin{aligned} \mathcal{E} &= \frac{1}{2} \int_\mathcal{V} (\epsilon_0 E^2 + B^2/\mu_0) d\mathcal{V} \\ &= \sum_\lambda (\dot{q}_\lambda^2 U_\lambda + \omega_\lambda^2 q_\lambda^2 U_\lambda + r_\lambda^2 T_\lambda). \end{aligned} \tag{B.17}$$

## B.2 Longitudinal Wake-field

A particle with charge $Q$ traverses with velocity $v = c$ a closed, otherwise empty, cavity which has perfectly conducting walls. Axes are arranged on this arbitrary cavity such that the charge enters at $z = 0$ and at time $t = 0$. It leaves at $z = L$. The longitudinal wake potential $W_z$ is obtained from the total voltage lost by a test charge which follows at a distance $s$, divided by $Q$, where the following test charge takes the same path as the driving charge $Q$ and also travels at $v = c$. This voltage is obtained from the line integral of the $z$ component of electric field along the path followed, thus

$$W_z(s) = -\frac{1}{Q}\int_0^L dz E_z(z,(z+S)/c) \tag{B.18}$$

where $E_z(z,t)$ is the $z$ component of electric field $\mathbf{E}$ on the axis due to the exciting charge. $W_z = 0$ for all $s < 0$ since the signal can not propagate faster than the speed of light and "over-take" the driving charge.

We must write down the source terms due to the exciting charge in order to find the fields in the cavity and further calculate $W_z$. Consider the charge $Q$ as a delta-function in $x$ and $y$ and advancing through the cavity along $Z$ thus

$$\begin{aligned} \rho(\mathbf{x},\mathrm{t}) &= Q\delta(x)\delta(y)\delta(z-ct) \\ \mathbf{j}(\mathbf{x},\mathrm{t}) &= \hat{\mathbf{z}}c\rho(\mathbf{x},\mathrm{t}). \end{aligned} \tag{B.19}$$

These source terms can now be inserted into Equation B.10 to give

$$\ddot{q}_\lambda + \omega_\lambda^2 q_\lambda = \frac{Qc}{2U_\lambda}\begin{cases} 0 & t < 0 \\ a_{\lambda z}(0,0,ct) & 0 < t < L/c \\ 0 & t > L/c, \end{cases} \tag{B.20}$$

where we take the $z$ component of $\mathbf{a}_\lambda$. This second order differential equation is approached by variation of parameters[1] and with the initial conditions determined

[1]The homogeneous equation is solved separately.

by excluding fields from the cavity before the charge enters $q(0) = \dot{q}(0) = 0$. B.20 then yields

$$q_\lambda(t) = \frac{Qc}{2U_\lambda\omega_\lambda}\int_0^{\min(t,L/c)} dt' \sin\omega_\lambda(t-t')\; a_{\lambda z}(0,0,ct'). \tag{B.21}$$

Similarly, using Equation B.13 we get

$$r_\lambda(t) = \frac{Q}{2T_\lambda}\begin{cases} 0 & t<0 \\ \phi_\lambda(0,0,ct) & 0<t<L/c \\ 0 & t>L/c, \end{cases} \tag{B.22}$$

where $\phi_\lambda$ depends on $x$, $y$ and $z$. With the above expressions for $q_\lambda$ and $r_\lambda$ and using Equations B.15, B.16 and B.17 we can now describe the electromagnetic fields and stored energy due to the exciting charge at any time in terms of the empty cavity solutions $\mathbf{a}_\lambda$, $\phi_\lambda$, $\omega_\lambda$.

Equation B.17 is easily expanded using Equation B.21 and for times ($t > L/c$) after the exciting charge has left the cavity the energy deposited is

$$\begin{aligned} \mathcal{E} &= \sum_\lambda \left(\dot{q}_\lambda^2 + \omega_\lambda^2 q_\lambda^2\right) u_\lambda \\ &= Q^2 \sum_\lambda \frac{|V_\lambda|^2}{4U_\lambda}, \end{aligned} \tag{B.23}$$

where

$$V_\lambda = \int_0^L dz e^{i\omega_\lambda z/c} a_{\lambda z}(0,0,z). \tag{B.24}$$

One now recognises the loss factor[2] $k_\lambda$ as

$$k_\lambda = \frac{|V_\lambda|^2}{4U_\lambda} \tag{B.25}$$

and the stored energy can now be written in the simple form

$$\mathcal{E} = Q^2 \sum_\lambda k_\lambda. \tag{B.26}$$

[2]This is the same quantity discussed in Chapter 4.

The loss factor $k_\lambda$ is the amount of electromagnetic energy deposited in mode $\lambda$ by the exciting charge. From Equation B.9 we see that $U_\lambda$ differs from the total energy stored in the mode by just a multiplicative factor. For a test charge traversing the cavity along the $z$-axis at $v = c$ the quantity $|V_\lambda|^2$ is the square of the maximum voltage gained from the mode, up to the same factor. Therefore, it is safe to use the measured values directly in calculating the loss factors of a real cavity.

Using Equation B.15 the wake potential B.18 can now be expanded in terms of the cavity eigenmodes to give

$$W_z(s) = \frac{1}{Q}\sum_\lambda \int_0^L dz \left[\dot{q}_\lambda\left(\frac{z+s}{c}\right) a_{\lambda z}(0,0,z) + r_\lambda\left(\frac{z+s}{c}\right)\frac{\partial \phi_\lambda}{\partial z}(0,0,z)\right]. \quad \text{(B.27)}$$

We now introduce the shorthand that $a_{\lambda z}(z)$ represents $a_{\lambda z}(0,0,z)$ and substitute for $q_\lambda$ and $r_\lambda$ from Equations B.21 and B.22 to get the result. There are clearly three cases to consider, when the test charge enters after the exciting charge has left, when both the charges are within the cavity and, finally, when the test charge enters in advance of the exciting charge.

a) $s > L$: In this case we can set $r_\lambda = 0$ since there are no source terms. We require $\dot{q}_\lambda$ and, using Equation B.21, take the time-derivative directly

$$\begin{aligned}\dot{q}_\lambda(t) &= \frac{d}{dt}\left[\frac{Qc}{2U_\lambda\omega_\lambda}\int_0^{L/c} dt' \sin\omega_\lambda(t-t')\; a_{\lambda z}(ct')\right] \\ &= \frac{Qc}{2U_\lambda\omega_\lambda}\int_0^{L/c} dt'\omega_\lambda \cos\omega_\lambda(t-t')\; a_{\lambda z}(ct') \qquad \text{(B.28)}\end{aligned}$$

and then, remembering that both charges are ultra-relativistic and that the test charge traverses a distance $s$ behind the exciting charge, make the change of variables from time to position using the relation $t - t' = \frac{z+s}{c} - \frac{z'}{c}$ to get

$$\dot{q}_\lambda = \frac{Qc}{2U_\lambda}\int_0^L dz' \cos\frac{\omega_\lambda}{c}(z+s-z')\; a_{\lambda z}(z'). \quad \text{(B.29)}$$

We now have

$$W_z(s) = \sum_\lambda \frac{I_{1\lambda}(s)}{2U_\lambda} \qquad s > L, \quad \text{(B.30)}$$

with

$$\begin{aligned} I_{1\lambda}(s) &= \int_0^L dz \int_0^L dy a_{\lambda z}(z) a_{\lambda z}(y) \cos\frac{\omega_\lambda}{c}(z+s-y) \\ &= \mathcal{R}e\left\{V_\lambda^* V_\lambda e^{i\omega_\lambda s/c}\right\}, \end{aligned} \tag{B.31}$$

where we have made the change of variable $z' \rightarrow y$ to match the notation in [100]. Equation B.30 can be rewritten as

$$W_z(s) = \sum_\lambda 2k_\lambda \cos\frac{\omega_\lambda s}{c} \qquad s > L. \tag{B.32}$$

b) $0 < s < L$: The source terms induced by the exciting charge must be considered here but it can be shown that the problem serendipitously reduces to

$$\begin{aligned} W_z(s) &= \sum_\lambda \frac{I_{1\lambda}(s)}{2U_\lambda} \\ &= \sum_\lambda 2k_\lambda \cos\frac{\omega_\lambda s}{c} \qquad 0 < s < L. \end{aligned} \tag{B.33}$$

c) $s < 0$: From causality

$$W_z(s) = 0 \qquad s < 0. \tag{B.34}$$

The simple forms derived here are due to the assumption that the velocities are $c$. For cases $v \not\approx c$ the scalar potential terms need to be evaluated and $W_z$ becomes difficult to deal with.

## B.3 Transverse Wake-fields

The transverse momentum kick experienced by a test charge following on the same path a distance $s$ behind the driving charge $Q$ defines the transverse wake potential $W_\perp$ up to a factor of $Q$. Consider the same closed, empty, perfectly conducting cavity traversed by the same pair of ultra-relativistic charges.

$$\begin{aligned}
\mathbf{W}_\perp(s) &= \frac{1}{Q}\int_0^L dz\,[\mathbf{E}_\perp + (\mathbf{v}\times\mathbf{B})_\perp]_{t=(z+s)/c} \\
&= \frac{1}{Q}\int_0^L dz\left[\nabla_\perp(\mathbf{v}\cdot\mathbf{A}) - \left(\frac{\partial}{\partial t} + \mathbf{v}\cdot\nabla\right)\mathbf{A}_\perp - \nabla_\perp\Phi\right]_{t=(z+s)/c} \\
&= \frac{1}{Q}\int_0^L dz\,[c\nabla_\perp A_z - \nabla_\perp\Phi]_{t=(z+s)/c} \\
&\quad -\frac{1}{Q}\int_0^L dz\left[\left(\frac{\partial}{\partial t} + \mathbf{v}\cdot\nabla\right)\mathbf{A}_\perp\right]_{t=(z+s)/c}. \qquad \text{(B.35)}
\end{aligned}$$

The second integral in Equation B.35 above can be evaluated directly remembering the total derivative $d\mathbf{A}_\perp$ and then transforming variables. For $\mathbf{A}_\perp(x,y,z,t)$ we have

$$d\mathbf{A}_\perp = \frac{\partial A_\perp}{\partial x}dx + \frac{\partial A_\perp}{\partial y}dy + \frac{\partial A_\perp}{\partial z}dz + \frac{\partial A_\perp}{\partial t}dt. \qquad \text{(B.36)}$$

The integral $J$ can now be evaluated as follows

$$\begin{aligned}
J &= \frac{1}{Q}\int_0^L dz\left[\left(\frac{\partial}{\partial t} + \mathbf{v}\cdot\nabla\right)\mathbf{A}_\perp\right]_{t=(z+s)/c} \\
&= \frac{1}{Q}\int_0^L dz\left[\frac{\partial A_\perp}{\partial t} + v_x\frac{\partial A_\perp}{\partial x} + v_y\frac{\partial A_\perp}{\partial y} + v_z\frac{\partial A_\perp}{\partial z}\right] \\
&= \frac{1}{Q}\int_0^L dz\left[\frac{\partial A_\perp}{\partial t} + \frac{dx}{dt}\frac{\partial A_\perp}{\partial x} + \frac{dy}{dt}\frac{\partial A_\perp}{\partial y} + \frac{dz}{dt}\frac{\partial A_\perp}{\partial z}\right]. \qquad \text{(B.37)}
\end{aligned}$$

Of course $\frac{dz}{dt}$ is just the velocity $c$ and the integral now reduces such that

$$\begin{aligned}
J &= \frac{1}{Q}\int\left[\frac{\partial A_\perp}{\partial t}cdt + c\frac{\partial A_\perp}{\partial x}dx + c\frac{\partial A_\perp}{\partial y}dy + c\frac{\partial A_\perp}{\partial z}dz\right] \\
&= \frac{c}{Q}\int d\mathbf{A}_\perp \\
&= \frac{c}{Q}\mathbf{A}_\perp\Big|_0^L. \qquad \text{(B.38)}
\end{aligned}$$

Equation B.35 can now be written

$$\mathbf{W}_\perp(s) = \frac{1}{Q}\int_0^L dz\,[c\nabla_\perp A_z - \nabla_\perp\Phi]_{t=(z+s)/c} - \frac{c}{Q}\mathbf{A}_\perp\Big|_{0,t=s/c}^{L,t=(L+s)/c}. \qquad \text{(B.39)}$$

For cavities with walls perpendicular to the $z$-axis where the charges enter and exit the cavity the boundary terms in Equation B.39 are zero and can be dropped. In their absence the treatment becomes neater but they can be added at the end. Substituting Equations B.4 and B.6 into Equation B.39 to get

$$\mathbf{W}_\perp(s) = \frac{1}{Q}\sum_\lambda \int_0^L dz \left[ cq_\lambda \left(\frac{z+s}{c}\right) \nabla_\perp a_{\lambda z}(z) - r_\lambda \left(\frac{z+s}{c}\right) \nabla_\lambda \phi_\lambda(z) \right]. \quad \text{(B.40)}$$

Again, having substituted for $q_\lambda$, $r_\lambda$ from Equations B.21 and B.22 the transverse wakefield can now be solved in three parts.

a) $s > L$:

$$\mathbf{W}_\perp(s) = \sum_\lambda \frac{cI'_{1\lambda}(s)}{2U_\lambda \omega_\lambda} \quad s > L, \quad \text{(B.41)}$$

and using the same notation that $y$ stands for $t'$, $I'_{1\lambda}$ is written

$$\begin{aligned} I'_{1\lambda}(s) &= \int_0^L dz \int_0^L dy \left(\nabla_\perp a_{\lambda z}(z)\right) a_{\lambda z}(y) \sin\frac{\omega_\lambda}{c}(z+s-y) \quad \text{(B.42)} \\ &= \mathcal{I}\mathrm{m}\{V_\lambda^* \nabla_\perp V_\lambda e^{i\omega_\lambda s/c}\}. \end{aligned}$$

b) $0 < s < L$: Here

$$\mathbf{W}_\perp(s) = \sum_\lambda \left( c\frac{I'_{1\lambda}(s) - I'_{2\lambda}(s)}{2U_\lambda\omega_\lambda} - \frac{K'_{1\lambda}(s)}{2T_\lambda} \right) \quad 0 < s < L, \quad \text{(B.43)}$$

where

$$I'_{2\lambda}(s) = \int_0^{L-s} dz \int_{z+s}^L dy (\nabla_\perp a_{\lambda z}(z)) a_{\lambda z}(y) \sin\frac{\omega_\lambda}{c}(z+s-y) \quad \text{(B.44)}$$

and

$$K'_{1\lambda}(s) = \int_0^{L-s} dz (\nabla_\perp \phi_\lambda(z)) \phi_\lambda(z+s). \quad \text{(B.45)}$$

In the range $-L < s < 0$ we get the relation

$$\mathbf{W}_\perp(s) = \sum_\lambda \left( c\frac{I'_{3\lambda}(s)}{2U_\lambda\omega_\lambda} - \frac{K'_{2\lambda}(s)}{2T_\lambda} \right) = 0 \quad -L < s < 0, \quad \text{(B.46)}$$

with

$$\begin{aligned} I'_{3\lambda}(s) &= \int_{-s}^{L} dz \int_{0}^{z+s} dy (\nabla_\perp a_{\lambda z}(z)) a_{\lambda z}(y) \sin \frac{\omega_\lambda}{c}(z+s-y) \\ &= -\int_{0}^{L+s} dz \int_{z-s}^{L} dy a_{\lambda z}(z) \nabla_\perp(y) \sin \frac{\omega\lambda}{c}(z+s-y) \end{aligned} \tag{B.47}$$

and

$$\begin{aligned} K'_{2\lambda}(s) &= \int_{-s}^{L} dz (\nabla_\perp \phi_\lambda(z)) \phi_\lambda(z+s) \\ &= \int_{0}^{L+s} dz (\nabla_\perp \phi_\lambda(z-s)) \phi(z). \end{aligned} \tag{B.48}$$

In general these integral terms cannot be simplified. However, there are certain conditions of the geometry under which Equation B.43 can be simplified for $0 < s < L$.

c) $s < 0$: From causality we know

$$\mathbf{W}_\perp(s) = 0 \quad s < 0. \tag{B.49}$$

Observing the form of $I'_{2\lambda}$, $I'_{3\lambda}$ and $K'_{1\lambda}$, $K'_{2\lambda}$ we see that there is some similarity. For a cavity with the geometry of a right cylinder with arbitrary cross-section, axis aligned along the $z$-axis $a_{\lambda z}$ can be written as

$$a_{\lambda z}(x, y, z) = f_\lambda(x, y) g_\lambda(z) \tag{B.50}$$

and similarly $\phi_\lambda$. In this case

$$\begin{aligned} I'_{2\lambda}(s) &= -I'_{3\lambda}(-s) \\ K'_{1\lambda}(s) &= K'_{2\lambda}(-s) \end{aligned} \qquad 0 < s < L, \tag{B.51}$$

Utilizing Equation B.51 the form of $\mathbf{W}_\perp$ for $0 < s < L$ reduces to the same form as in the range $s > L$ and we now have

$$\mathbf{W}_\perp(s) = \sum_\lambda c \frac{V_\lambda^* \nabla_\perp V_\lambda}{2 U_\lambda \omega_\lambda} \sin \frac{\omega_\lambda}{c} \quad s > 0 \tag{B.52}$$

for cavities with translational symmetry along the $z$-axis.

Further, for infinitely repeating structures which are cylindrically symmetric using cylindrical polar coordinates $(r, \theta)$ - the modes depend on $\theta$ as $e^{im\theta}$ where $m$ is an integer. $m = 0, 1, 2$ refer to the longitudinal / monopole mode, dipole modes and quadrupole modes respectively. The transverse wake component for modes $m \neq 0$ can be written, for $s > 0$ as

$$\mathbf{W}_{\perp m} = m \left(\frac{r'}{a}\right)^m \left(\frac{r}{a}\right)^{m-1} \left(\hat{r}\cos m\theta - \hat{\theta}\sin m\theta\right) \sum_\lambda \frac{2k_{m\lambda}(a)}{\omega_{m\lambda}a/c} \sin\frac{\omega_{m\lambda}s}{c} \qquad \text{(B.53)}$$

where $k_{m\lambda}$ is the loss factor calculated at $r = a$.

# Appendix C

# Panofsky-Wenzel Theorem

There is a relation between the transverse and the longitudinal wake potential, usually called the Panofsky-Wenzel theorem, which was published by Panofsky and Wenzel in 1956 [41]. The derivation requires only the use of Faraday's induction law

$$\mathbf{e}_z \times \frac{\partial}{\partial t}\mathbf{B}_\perp = \frac{\partial}{\partial z}\mathbf{E}_\perp - \nabla_\perp E_z \tag{C.1}$$

and it relates the net transverse kick experienced by a test charge crossing a cavity that contains electromagnetic fields derived form a vector potential. Applying the above equation to the transverse wake potential in Equation 4.16 we obtain:

$$\begin{aligned}
\partial_s \mathbf{W}_\perp(\mathbf{r}_\perp, s) &= \frac{1}{q}\int_{-L/2}^{L/2} dz \left[\frac{\partial}{\partial s}\mathbf{E}_\perp(\mathbf{r}_\perp, z, t) + v\mathbf{e}_z \times \frac{\partial}{\partial s}\mathbf{B}_\perp(\mathbf{r}_\perp, z, t)\right]_{t=(z+s)/v} \\
&= \frac{1}{q}\int_{-L/2}^{L/2} dz \left[\frac{1}{v}\frac{\partial}{\partial t}\mathbf{E}_\perp(\mathbf{r}_\perp, z, t) + \mathbf{e}_z \times \frac{\partial}{\partial t}\mathbf{B}_\perp(\mathbf{r}_\perp, z, t)\right]_{t=(z+s)/v} \\
&= \frac{1}{q}\int_{-L/2}^{L/2} dz \left[(\frac{\partial}{\partial z} + \frac{1}{v}\frac{\partial}{\partial t})\mathbf{E}_\perp(\mathbf{r}_\perp, z, t) - \nabla_\perp E_z(\mathbf{r}_\perp, z, t)\right]_{t=(z+s)/v} \\
&= \frac{1}{q}\int_{-L/2}^{L/2} dz \left[\frac{d}{dz}\mathbf{E}_\perp(\mathbf{r}_\perp, z, t) - \nabla_\perp E_z(\mathbf{r}_\perp, z, t)\right]_{t=(z+s)/v} \\
&= -\nabla_\perp W_\parallel(\mathbf{r}_\perp, s) + \frac{1}{q}\mathbf{E}_\perp(\mathbf{r}_\perp, z, t)_{t=(z+s)/v}\Big|_{-L/2}^{L/2}.
\end{aligned} \tag{C.2}$$

When the transverse field for a given $s$ is equal at the beginning and the end of

the cavity the last term on the right hand side will vanish and hence

$$\partial_s \mathbf{W}_\perp(\mathbf{r}_\perp, s) = -\nabla_\perp \mathbf{W}_\parallel(\mathbf{r}_\perp, s) \tag{C.3}$$

giving a relation between the longitudinal derivative of the transverse wake potential and the transverse gradient of the longitudinal potential that allows for the calculation, by integration, of the transverse potential once the longitudinal is known.

# References


[1] R.M. Jones & C.J. Glasman. *Higher Order Mode Wake-field Simulations And Beam Dynamics Simulations In The ILC Main Linacs.* LINAC06, 2006.

[2] C.J. Glasman. *Higher Order Mode Wake-fields in the Main Linacs of the International Linear Collider.* Thesis, University of Manchester, UK, 2006.

[3] https://twiki.cern.ch/twiki/bin/view/AtlasPublic/LuminosityPublicResults.

[4] *Statement on Linear Colliders.* International Committee On Future Accelerators, http://www.fnal.gov/directorate/icfa/icfa_LCstatement.html, 1999.

[5] G. Moortgat-Pick. *Impact of polarized $e^-$ and $e^+$ beams at a future Linear Collider and a Z-factory.* Journal of Physics: Conference Series 298 (2011) 01200), 2011.

[6] Helmut Wiedemann. *Particle Accelerator Physics.* Springer, 2007.

[7] *CLIC Conceptual Design Report.* http://clic-study.org/ accelerator/CLIC-ConceptDesignRep.php, 2011.

[8] ITRP Recommendation, http://www.fnal.gov/directorate/icfa/ITRP Report Final.pdf, 2004.

[9] F. Zimmermann. Accelerators physics lectures, part 2. In *Ambleside Linear Collider School*, 2009.

[10] International Committee On Future Accelerators, ICFA endorses the Technology Recommendation Panel report, http://www.interactions.org/cms/?pid=1014290, 2004.

[11] A. Grudiev *et al.*. *Optimum Frequency And Gradient For The CLIC Main Linac*. EPAC, CERN-AB-2006-028, 2006.

[12] V.F. Khan, A. D'Elia, R.M. Jones, A. Grudiev, W. Wuensch, G. Riddone, and V. Soldatov. *Wakefield and surface electromagnetic field optimisation of manifold damped accelerating structures for CLIC*. Nuclear Instruments and Methods in Physics Research Section A: Accelerators, Spectrometers, Detectors and Associated Equipment, V 657, 1 pp131, 2011.

[13] N. I. Baboi. *Studies on Higher Order Modes in Accelerating Structures for Linear Colliders*. PhD Thesis, DESY-University of Hamburgh., 2001.

[14] P.B. Wilson. Introduction to wakefields and wake potentials. *AIP Conference Proceedings*, 184(1):525–564, April 1989.

[15] W.K.H. Panofsky R.B. Neal. *Electrons Accelerated to the 10-20 GeV Range*. Science, Vol. 152, p, 1353, SLAC-PUB-0197, June 1966.

[16] The International Linear Collider Reference Design Report, http://www.linear collider.org/about/Publications/Reference-Design-Report, 2007.

[17] T. Nishitani et al. *Highly polarized electrons from GaAsGaAsP and InGaAsAlGaAs strained-layer superlattice photocathodes,*. J. Appl. Phys. 97, 094907, 2005.

[18] T. Maruyama et al. *Systematic study of polarized electron emission from strained GaAs/GaAsP superlattice photocathodes*. Appl. Phys. Lett. 85, 2640, 2004.

[19] N. Chanlek. *Quantum Efficiency Lifetime Studies using the Photocathode Preparation Experimental Facility Developed for the ALICE Accelerator*. Thesis, University of Manchester, 2011.

[20] F. Zhou et al. *Start-to-end transport design and multi-particle tracking for the ILC*. SLAC-PUB 12240, 2007.

[21] The International Linear Collider, a Technical Progress Report, http://www.linearcollider.org/about/Publications/interim-report.

[22] XFEL Technical Information, http://xfel.desy.de/technical_information/.

[23] B. Aune, R. Bandelmann, D. Bloess, B. Bonin, A. Bosotti, M. Champion, C. Crawford, G. Deppe, B. Dwersteg, D. Edwards, H. Edwards, M. Ferrario, M. Fouaidy, P.-D. Gall, A. Gamp, A. Gössel, J. Graber, D. Hubert, M. Hüning, M. Juillard, T. Junquera, H. Kaiser, G. Kreps, M. Kuchnir, R. Lange, M. Leenen, M. Liepe, L. Lilje, A. Matheisen, W.-D. Möller, A. Mosnier, H. Padamsee, C. Pagani, M. Pekeler, H.-B. Peters, O. Peters, D. Proch, K. Rehlich, D. Reschke, H. Safa, T. Schilcher, P. Schmüser, J. Sekutowicz, S. Simrock, W. Singer, M. Tigner, D. Trines, K. Twarowski, G. Weichert, J. Weisend, J. Wojtkiewicz, S. Wolff, and K. Zapfe. Superconducting TESLA cavities. *Physical Review Special Topics - Accelerators and Beams*, 3(9):092001, September 2000.

[24] C. Simon et al. Performance of a reentrant cavity beam position monitor. *Physical Review Special Topics - Accelerators and Beams*, 11(8):082802–, August 2008.

[25] Roger M. Jones and R.H. Miller. Mitigation of emittance dilution due to transverse mode coupling in the L-band linacs of the ILC. *Conf.Proc.*, C060626:843–845, 2006.

[26] T. Raubenheimer. *The Generation And Acceleration of Low Emittance Flat Beams For Future Linear Colliders.* Thesis, Stanford University & SLAC-387, 1991.

[27] G. Burt, A. Dexter, and P Goudket. *Effect and tolerances of RF phase and amplitude errors in the ILC crab cavity.* EUROTeV-Report-2006-098, 2006.

[28] E. Jensen. *Normal Conducting CLIC Technology.* CLIC Note 641, Switzerland., 2005.

[29] M. Battaglia et al. *Physics at the CLIC mlulti-TeV linear collider.* http://documents.cern.ch/cernrep/2004/2004-005/2004-005.html, 2005. Report of the CLIC Physics Working Group, CERN 2004-05.

[30] R. W. Assmann et al. *A 3 TeV $e^+ e^-$ Linear Collider based on CLIC Technology.* 2000.

[31] H. H. Braun et al. CLIC 2008 Parameters, CLIC Note 764, 2008.

[32] http://clic-study.web.cern.ch/clic-study/Layout/OverallCLIC3.html.

[33] F. Antoniou and Y. Papaphilippou. Optics Design Considerations for the CLIC Pre-damping Rings. *Conf.Proc.*, C0806233:MOPP062, 2008.

[34] J. D. Jackson. *Classical Electrodynamics.* New York, John Wiley & Son, Inc.Second edition, 1975.

[35] K.L.F. Bane. *Wakefields and Wakefield Acceleration.* Invited Talk Presented at The Third Summer School On High Energy Particle Accelerator USA, SLAC-PUB-3528, *et al.*

[36] I. Zagorodnov and T. Weiland. *TE/TM field solver for particle beam simulations without numerical Cherenkov radiation.* Phys. Rev. ST Accel. Beams, vol. 8, p. 042001, 2005.

[37] P. Wilson. *High Energy Electron Linacs: Applications To Storage Ring RF Systems and Linear Colliders.* SLAC-PUB-2884, 1991.

[38] J. Buon. *Beam Phase Space and Emittance.* CERN Accelerator School, University of Jyaskyla, Finland, 1992.

[39] J. Rossbach and P. Schmuser. *Basic Course on Accelerator Optics.* CERN Accelerator School, University of Jyaskyla, Finland, 1992.

[40] E.U. Condon. *Forced Oscillations in Cavity Resonators.* J. Appl. Phys.12, 129, 1941.

[41] W.K.H. Panofsky and W.A Wenzel. *Some Considerations Concerning the Transverse Deflection of Charged Particles in Radio-Frequency Fields.* Rev. Sci. Instrum. 27, 967, 1956.

[42] R. Zennaro. *Study Of The validity Of The K. Bane's Formulae For The CLIC Accelerating Structures.* Proceedings Of European Particle Accelerator Conference, EPAC08, Italy., 2008.

[43] K. L. F. Bane. Short-range dipole wakefields in accelerating structures for the nlc. *SLAC-PUB-9663.*, 2003.

[44] T. Weiland and R. Wazenberg. *Wakefields and Impedances.* US-CERN Accelerator Course, Carolina, USA, 1991.

[45] E. Keil. *Diffraction radiation of charged rings moving in a corrugated cylindrical pipe A model of radiation losses in an electron ring accelerator.* Nucl. Instr. Meth. 100, 419-427, 1972.

[46] D. Brandt and B.Zotter. *Calculation of the Wakefield with the Optical Resonator Model.* CERN-ISR/TH/82-13 and LEP Note 388, 1982.

[47] L.A. Vainshtein. *The Theory of diffraction and the factorization method: (generalized Wiener-Hopf technique).* Golden Press, Boulder CO, USA, 1969.

[48] K. Bane and Perry B. Wilson. *Longitudinal and Transverse Wake Potentials in SLAC. (Talk).* 1980.

[49] B.W. Zotter & S.A. Kheifets. *Impedances and Wakes in High-Energy Particle Accelerators.* World Scientific, 1998.

[50] Y. H. Chin. *Users guide for new ABCI version 6.1 (azimuthal beam cavity interaction).* CERN-SL-92-49-AP.

[51] V. Khan. *A Damped and Detuned Accelerating Structure for the Main Linacs of the Compact Linear Collider.* University of Manchester, UK, 2011.

[52] K.A. Thompson & R.D. Ruth. *Multibunch Beam Breakup in High Energy Linear Colliders*. PAC 1989, 1989.

[53] J. Bardeen & L.N. Cooper & J.R. Schieffer. *Theory of Superconductivity*. Phys. Rev. Lett. 1, 399-400, 1957.

[54] L.N Cooper. *Bound Electron Pairs in a Degenerate Fermi Gas*. Physical Review, 104 pp 1189-1190, November 1956.

[55] Hasan Padamsee, Jens Knobloch, and Tomas Hays. *RF Superconductivity For Accelerators*. Wiley, 2008.

[56] F. London. *Superfluids: Macroscopic Theory of Superconductivity, Vol. I*. New York: Wiley, London:Chapman & Hall, 1950.

[57] J. Bardeen. *Theory of the Meissner Effect in Superconductors*. Phys. Rev. 97, 1724-1725, 1955.

[58] K.Saito. *Fundamental RF Critical Field Overview*. Pushing The Limits Of RF Superconductivity Workshop, Argonne, USA, 2004.

[59] D.L. Moffat, T. Flynn, J. Kirchgessner, H. Padamsee, D. Rubin, J. Sears, and Q. Shu. Superconducting Niobium RF Cavities Designed to Attain High Surface Electric Fields. In *Proceedings of the Fourth Workshop on RF Superconductivity, KEK, Tsukuba, Japan*, 1989.

[60] J Graber, C Crawford, J Kirchgessner, H Padamsee, D Rubin, and P Schmueser. Reduction of field emission in superconducting cavities with high power pulsed RFQ. *Nuclear Instruments and Methods in Physics Research Section A: Accelerators, Spectrometers, Detectors and Associated Equipment*, 350(3):572–581, November 1994.

[61] J. R. Delayen and K. W. Shepard. Tests of a superconducting rf quadrupole device. *Applied Physics Letters*, 57(5):514, July 1990.

[62] P. Kneisel, B. Lewis, and L. Turlington. Experience with High Pressure Ultrapure Water Rinsing of Niobium Cavities. In *Proceedings of the Sixth Workshop on RF Superconductivity, CEBAF, Newport News, Virginia, US*, 1993.

[63] K Saito. Development of electropolishing technology for superconducting cavities. In *Proceedings of the 2003 Particle Accelerator Conferenc*, 2003.

[64] V Shemelin and H. Padamsee. The Optimal Shape of Cells of a Superconducting Accelerating Section. *Cornell SRF 020128-01*, 2002.

[65] H. Shemelin, V. Padamsee and R. Geng. Optimal cells for tesla accelerating structure. *Nuclear Instruments and Methods in Physics Research Section A: Accelerators, Spectrometers, Detectors and Associated Equipment*, 496(1):1–7, 2003.

[66] J Sekutowicz, P. Kneisel, G Ciovati, and H Wang. Low Loss Cavity for the 12 GeV CEBAF Upgrade. *JLAB Technical Report TN-02-023*, 2002.

[67] J Luk, V Shemelin, and Dmitry Myakishev. Optimization Of The End Cells In SRF Cavities. *Cornell SRF 050808-07*, 2005.

[68] R.L. Geng. *Review Of New Shapes For Higher Gradients.* Invited talk at 12$^{\text{th}}$ International Workshop on RF Superconductivity, July 10-15, NY, 2005.

[69] N. Juntong. *Investigation of the Optimised Electromagnetic fields in SRF cavities for the ILC.* Thesis, University of Manchester, 2011.

[70] A. Thom. *Field Computations in Engineering and Physics.* Van Nost. Reinhold, C.J. Aspelt.

[71] W. Bruns. *The GdfidL Electromagnetic Field Simulator.* www.gdfidl.de.

[72] T. Wangler. *RF Linear Accelerators.* Wiley, 2008.

[73] W. Bruns. *Improvements In GdfidL.* PAC 1999 (THA71), 1999.

[74] W. Bruns. *Short Range Wakepotentials Computed in a Moving Frame.* EPAC08 (TUPP087), 2008.

[75] R. Schuhmann & T. Weiland. *Rigorous analysis of trapped modes in accelerating cavities.* PRST:AB Vol. 3 122002, 2000.

[76] T. Weiland. *On the numerical solution of Maxwell's Equations and applications in the field of accelerator physics.* Part. Acc. 15, 245-292, 1984.

[77] MAFIA, CST GmbH, Darmstadt, Germany.

[78] C.J. Glasman *et al. Simulations of Transverse Higher Order Deflecting Modes in the Main Linacs of ILC.* SRF2007, Beijing, China, 2007.

[79] L. Xiao, C. Adolphsen, V. Akcelik, A. Kabel, K. Ko, L. Lee, Z. Li, and C. Ng. Modeling Imperfection Effects on Dipole Modes in TESLA Cavity. *Conf.Proc.*, C070625, August 2007.

[80] K. Wille. *The Physics of Particle Accelerators.* OUP, 2000.

[81] A. Wolski. *Linear Dynamics.* Lectures delivered to The Cockcroft Institute, Daresbury, UK, 2006.

[82] R. Assman *et al.. LIAR - A Computer Program for the Modeling and Simulation of High Performance Linacs.* SLAC/AP-103, 1997.

[83] P. Tenenbaum *et al. The Lucretia Project.* http://www.slac.stanford.edu/accel/ilc/codes/Lucretia/.

[84] D. Schulte *et al. . PLACET.* http://dschulte.web.cern.ch/dschulte/placet.html, 2004.

[85] U.S. Linear Collider Steering Group. Accelerator technology options report. Technical report, Linear Collider Technology Options Study, 2004.

[86] Z. Li et al. Optimization of the Low Loss SRF Cavity for the ILC. Particle Accelerator Conference PAC07 25-29 Jun 2007, Albuquerque, New Mexico.

[87] B. Muratori. *Luminosity in the presence of offsets and a crossing angle.* CERN AB-NOTE-2003-026, 2003.

[88] I.R.R. Shinton, G. Burt, and C.J. Glasman et al. *Beam dynamic simulations of the CLIC crab cavity and implications on the BDS.* NIMS A 657 (2011) 126-130, 2011.

[89] CLIC Study Group, http://clic-meeting.web.cern.ch/clic-meeting/clictable 2010.html, 2010.

[90] http://clicr.web.cern.ch/CLICr/MainBeam/BDS/v_10_01_25.

[91] H. Braun *et al. CLIC 2008 Parameters.* CLIC-Note-76, 2008.

[92] A.C. Dexter *et al.. CLIC crab cavity design optimisation for maximum luminosity.* NIMS A 657 (2011) 45-51, 2011.

[93] G. Burt, A. Latina, D. Schulte, A. C. Dexter, and P. A. McIntosh. Anticrab cavities for the removal of spurious vertical bunch rotations caused by crab cavities. *Phys. Rev. ST Accel. Beams*, 11:092801, Sep 2008.

[94] D. Schulte. *Study of Electromagnetic and Hadronic Background in the Interaction Region of the TESLA Collider.* PhD thesis, DESY / University of Hamburg (TESLA-97-08), 1997.

[95] D. Schulte. Beam-beam simulations with GUINEA-PIG. *Proceedings of the 1998 International Computational Accelerator Physics Conference*, 1998.

[96] R.H. Bartels. *An Introduction to Splines for Use in Computer Graphics and Geometric Modelling.* Morgan Kaufmann, pp. 9-17, 1998.

[97] A. Chao & M. Tigner. *Handbook of Accelerator Physics and Engineering.* World Scientific, 1999.

[98] M. Heil & A. Hazel. `oomph-lib` - *The Object-Orientated Multi-Physics Finite Element Library.* http://www.oomph-lib.org.

[99] R.L. Muddle. *Parallel Block Preconditioning For Multi-Physics Problems.* Thesis, University of Manchester, 2011.

[100] K.L.F. Bane & P.B. Wilson & T. Weiland. *Wake Fields And Wake Field Acceleration.* SLAC-PUB-3528, 1984.